Methods for MRI RF Pulse Design and Image Reconstruction

by

Feng Zhao

A dissertation submitted in partial fulfillment
of the requirements for the degree of
Doctor of Philosophy
(Biomedical Engineering)
in The University of Michigan
2014

Doctoral Committee:

        Professor Douglas C. Noll, Co-Chair
        Professor Jeffrey A. Fessler, Co-Chair
        Professor Thomas L. Chenevert
        Assistant Research Scientist Jon-Fredik Nielsen

ACKNOWLEDGEMENTS

First of all, I would like to thank my adviser, Doug Noll, for picking me to join this lab about four and half years ago when I was still a senior undergraduate student in China. Before I came to US, I was told that as an international PhD student, my adviser was going to be the most important people in my life in US other than my family and parents. Now I feel very lucky to have Doug to be this important people. He is very knowledgeable and nice to answer any questions I have in research. From him, I learned how to do good research and how to make impact to the field. Other than research, he has been very helpful in advising me to choose career paths. He also provides the maximal degrees of freedom for me to balance my life and work, which was especially helpful for me to get over the tough time since this spring.

I would also like to thank my adviser, Jeff Fessler, who had been generously helping with my research and study as an "unofficial" adviser for most of the time. If it is lucky to have a great adviser, then I feel even luckier to have two great advisers to be the "important" people in my life. He is always so passionate and curious about any topics I bring up during the meeting, and he is also very creative and always has novel ideas or useful suggestions for me. He is also very careful about details, from each line of mathematical derivations to every single font in the manuscripts. This is not just very valuable for my research, but is also the right attitude to everything in our life.

Next, I would like to thank Jon Nielsen who has been so nice to mentor and help me with almost every aspect of my research and experiments. Without Jon's help, I

can not imagine how much longer I would need to finish my PhD Projects. Most of my knowledge about pulse sequence programming and MRI scanner operations was from him. It is so nice of him that he always warmly welcomes me to interrupt him and discuss my own projects.

I would also like to thank Scott Swanson for helping me on the magnetization transfer experiments. I also really appreciate the work by the Texas A&M group, including Professor Steve Wright, Katie Moody and Neal Hollingsworth. They were dedicated to building the parallel excitation system for us, and provided me a lot of knowledge about MRI system engineering. I also would like to thank Professor Thomas Chenevert for kindly serving on my committee and providing useful suggestions for my research proposal.

I would like to thank my lab-mates who have provided an amazing work and life environment for me. Hao Sun and I have done quite a few projects together. He likes to discuss every detail of the research with me, which enlightened me a lot and broadened my views of thinking. Matt Muckley is a very neat traditional American who likes to discuss everything with me, including research, life, sports, history and culture. Most of my knowledge about Americans and USA was from him. With Alan Chu and Yash Shah who usually work at nights, I never felt alone when I had to stay up doing experiments in the midnight. I would also like to thank Steve Allen, Kathleen Ropella, Mai Le and Vivek Bhatia for the great time together in or out of the lab. I would also like to thank senior lab-mates, Daehyun Yoon, Yoon Chung Kim, Hesam Jahanian, Dan Weller and Sathish Ramani for sharing their experience and knowledge with me.

I am grateful to Luis Hernandez for nicely sharing his expertise for my projects and having me involved in the 7T scanner operations. I really appreciate the help from Scott Peltier for my *in-vivo* experiments and many other lab businesses. I would also like to thank Keith Newnham, Ryan Smith and Chuck Nicholas for helping with

TABLE OF CONTENTS

LIST OF FIGURES

Figure

LIST OF TABLES

LIST OF APPENDICES

Appendix

CHAPTER I

Introduction

Magnetic resonance imaging (MRI) is a revolutionary technique that helps clinical diagnosis by non-invasively and non-radioactively imaging human tissue. Briefly, MRI works by imaging signals from hydrogen in the body. The body is placed in a strong magnetic field, also known as (aka) B_0 *field*, and then a weak high frequency radio frequency (RF) signal, aka B_1 *field*, is transmitted to selectively excite the parts of the object to be imaged. Along with linear gradient fields afterwards, signals from the excited parts are encoded to produce MR images that reflect the anatomy.

This thesis first focuses on improving MR image quality and speed by developing fast and robust system calibration methods and image reconstruction methods, including B_1 field mapping [3] and MRI phase reconstruction. The remainder focuses on developing pulse sequences and image reconstruction methods to efficiently and robustly produce special image contrast, including fat suppression and magnetization transfer contrast [4].

1.1   RF Pulse Design in General

1.1.1   MRI Basics and RF Excitation

In MRI scanner, angular momentum possessed by the hydrogen nucleus (^{1}H), aka *spins*, generate a net effect called *magnetization* that can vary spatially ($\boldsymbol{r}$) and tem-

1

porally (t) and is denoted as $\vec{M}(\boldsymbol{r}, t)$. $\vec{M}(\boldsymbol{r}, t)$ is aligned with main field direction (the z direction or the *longitudinal* direction by convention) in the equilibrium, but detectable MRI signals are only from the transverse components of the magnetization which is perpendicular to z. Thus, to generate MRI signal, the magnetization needs to be "tipped" towards the *transverse plane* (x-y plane) by B_1 field (RF field) that is within the transverse plane, and this process is called *excitation*. Excitation typically needs inputs of RF field, which is called *RF pulse*, along with linear gradient fields to achieve a spatially varying transverse magnetization pattern. The linear gradient fields (gradients) consist of 3 channels that are along x, y and z directions respectively, and linearly vary the main field to generate spatial variations of magnetization behaviors.

The relation between the magnetization behaviors and the applied fields is governed by the Bloch equation [5]:

$$\frac{d}{dt}\vec{M}(\boldsymbol{r}, t) = \vec{M}(\boldsymbol{r}, t) \times \gamma\vec{B}(\boldsymbol{r}, t) \tag{1.1.1}$$

where the spatial location $\boldsymbol{r} \triangleq (x, y, z)$, $\vec{M}(\boldsymbol{r}, t) = [M_x(x, y, z, t),\ M_y(x, y, z, t),\ M_z(x, y, z, t)]$, $\gamma = 267, 51$ M rad/s/T is called *gyromagnetic ratio*, $\vec{B}(\boldsymbol{r}, t) = (\mathsf{Re}\{B_1(t)\}, \mathsf{Im}\{B_1(t)\}, B_0 + xG_x(t) + yG_y(t) + zG_z(t))$, $B_1(t)$ is the RF field, $G_x(t)$, $G_y(t)$ and $G_z(t)$ denote the gradient strengths in x, y and z direction respectively, and we have ignored relaxation effects. For each particular $\boldsymbol{r}$ and t, the effects of the applied field to the magnetization is that $\vec{M}(\boldsymbol{r}, t)$ precesses about $\vec{B}(\boldsymbol{r}, t)$ at the frequency $\gamma|\vec{B}(\boldsymbol{r}, t)|$, which is called *Larmor frequency*. In typical MRI scans, $B_0 \gg |B_1(t)|$ and $B_1(t)$ rotates about z at the Larmor frequency of the main field, i.e. γB_0. The main field strength of MRI scanners could range from hundreds of millitesla (mT) to tens of Tesla (T). Popular clinical scanners and research scanners are 1.5 T or 3 T, and 7 T scanners are also widely used in research studies. Thus, the Larmor frequency of

2

the main field strength can be quite high, e.g., about 128 MHz at 3 T. In contrast, the strength of B_1 field is on the order of tens of μT.

Ideally, a system would have homogeneous B_0 field and B_1 field, but it is rarely the case in practice. Although state-of-art MRI scanners can have very homogeneous B_0 field to several parts per million over a typical field of view, magnetic susceptibility differences among different parts of human body cause B_0 inhomogeneity inevitably [6]. This effect increases with the main field strength, so B_0 inhomogeneity is more problematic at higher field strengths. Since the resonant frequency of hydrogen is proportional to B_0, spins at field strengths off the nominal main field strength precess at different frequency than the on-resonance frequency, which is also known as off-resonance effect. At 3T, for example, the off-resonance frequencies of a region of human body can range from tens of Hz up to hundreds of Hz depending on the parts of the body. This is quite small compared to the center frequency, e.g., about 128 MHz at 3 T, but it is still large enough to cause problems in both excitation and image reconstruction if ignored. In addition, B_1 is also not uniform in practice, which is caused by dielectric resonance, RF attenuation by tissue conductivity and other RF-body interactions [7, 8]. Those effects are more severe at higher field strengths. B_1 inhomogeneity at 3T can range from $30 - 50\%$ [9]. B_1 inhomogeneity is less of a concern at field strengths less than 3T.

1.1.2 RF Pulse Design

As seen in the last section, both RF field and gradients can be temporally varying and programmed by RF pulse designers to achieve a certain target pattern of the magnetization at the end of the RF pulse and gradients. So RF pulse design is a process that takes the target pattern of the magnetization, $\vec{M}(\boldsymbol{r}, T)$, as input and determines the unknown gradients, $G_x(t), G_y(t), G_z(t)$ $(0 < t \leqslant T)$, and RF pulse, $B_1(t)$, based on a certain input-output relationship, such as (1.1.1), and the initial

3

state of the magnetization, $\vec{M}(\boldsymbol{r}, 0)$.

In practice, there are several constraints and limitations in the design. First, the pulse length, T, is usually limited to the needs for practical imaging time, tissue relaxation time, desired image contrast or RF power constraints. Second, the amplitude and the slew rate of the gradient waveforms are also limited due to hardware limitations and human body tolerance, e.g., peripheral nerve stimulation; for example, the maximal gradient amplitude and slew rate of our scanner are 40 mT/m and 180 T/m/s respectively. Furthermore, the maximal amplitude and power of RF pulse is limited mainly due to safety requirement for human body scanning.

Unfortunately, it is generally quite hard to obtain accurate RF pulses and gradients by solving (1.1.1) for an arbitrary target pattern from an arbitrary initial state, because either it can be too computationally intensive to solve the problem or there may be no analytical solution to (1.1.1). However, under some circumstances or with some approximations, the RF design problems can be practical. In most RF designs, the gradients, which almost are never linear, are predetermined according to the specific tasks, which largely simplifies the RF design problem. One of the most widely used categories of RF design is the *small-tip-angle* (STA) RF pulse design, where the magnetization is tipped down from the equilibrium to the transverse plane by a "small" angle ($< 30^0$). With STA approximation, the RF pulse has a Fourier-like relation with the transverse components of the resulting magnetization [10], and it can be linearized in general with some other approximations [11]. For larger flip angle target patterns, several methods have been proposed, including the ones with constraints on gradient waveforms [12, 13], the one using numerical simulators [14], the one based on control theory [15], and the ones with approximations on the Bloch equations [16, 17]. Furthermore, for the design where the target pattern is only a one dimensional (1D) function, a filter design based method has been proposed to design the RF pulses with very little approximations [18], which is called *Shinnar-Le Roux*

(SLR) pulse design. This method can also be used to design for the cases where the initial magnetization is not in the equilibrium, such as the inversion pulses that flip the transverse spins (magnetization) by 180^0. In addition, there are some methods proposed to jointly determine both the RF pulses and the gradient waveforms [19–22], where the gradient waveforms are constrained to certain types.

1.2   Small-tip angle (STA) RF Pulse Design

1.2.1   Multi-Dimensional STA Pulse Design

The STA approximation is an approximation to the Bloch equation (1.1.1) where $M_z(\boldsymbol{r}, t) \approx M_z(\boldsymbol{r}, 0) = M_0$ and M_0 is the magnetization at the equilibrium state. Assuming no B_1 field inhomogeneity, the pattern of the resulting transverse magnetization at time T (the end of the RF pulse) in terms of RF pulses and gradients is approximately:

$$M_{xy}(\boldsymbol{r}, T) = i\gamma M_0 \int\limits_0^T B_1(t) e^{i2\pi[\boldsymbol{k}(t)\cdot\boldsymbol{r}+(t-T)f_0(\boldsymbol{r})]} dt \qquad (1.2.1)$$

where i denotes the imaginary unit, $M_{xy}(\boldsymbol{r}, T) \triangleq M_x(\boldsymbol{r}, T) + iM_y(\boldsymbol{r}, T)$, $f_0(\boldsymbol{r})$ is the spatially varying off-resonance frequency map or B_0 map, and $\boldsymbol{k}(t) \triangleq [k_x(t), k_y(t), k_z(t)]$ denotes the so-called *excitation k-space trajectory*. The excitation k-space is defined as:

$$k_x(t) \triangleq \frac{\gamma}{2\pi} \int\limits_t^T G_x(\tau) d\tau \qquad (1.2.2)$$

where x can also be y or z for the other two directions. With gradient waveforms or excitation k-space predetermined, the resulting transverse magnetization pattern $M_{xy}(\boldsymbol{r}, T)$ has a Fourier relation with the RF pulse $B_1(t)$ if the off-resonance effects ($f_0(\boldsymbol{r})$) are ignored. Then such RF design can be carried out very efficiently with the

help of fast Fourier transform (FFT) if the excitation k-space is uniformly sampled. An example is the 1D slice-select pulse which is routinely used in 2D or 3D MRI scans [4]. The slice-select pulse is typically a sinc function of time that is the Fourier transform of the target magnetization pattern, i.e., a 1D rectangle function; the gradient waveforms use only the gradient in the slice-select direction (assuming non-oblique directions) and the waveform is a trapezoidal lobe followed by a trapezoidal refocusing lobe, which corresponds to coverage of the corresponding excitation k-space.

When excitation k-space is not uniformly sampled, RF pulse is computed by FFT with k-space velocity and density compensations [10] or by iterative methods [23] with nonuniform FFT (NUFFT) [24] . When $f_0(\boldsymbol{r})$ can not be ignored, methods have been proposed to solve this problem based on approximations in time domain or frequency domain [11, 25–27].

In general, the relation between the RF pulse and the excited magnetization in the STA regime is considered as Fourier-like relation, so we typically analyze the problem with tools of Fourier analysis. For example, the gradient waveforms (excitation k-space) are typically predetermined such that the RF pulse properly samples the Fourier domain of the target pattern, e.g., the excitation k-space samples need to be dense enough to avoid aliasing in the excited magnetization pattern and the excitation k-space coverage needs to be large enough to produce the desired variation in the excited pattern.

1.2.2 Considering the Spectral Domain

In the previous sections, we mainly discuss the spatially selective pulse design that aims at exciting a certain pattern in the spatial domain. Since human tissue that can be excited by MRI scanners is not limited to the on-resonance hydrogen in water, the spectral response of the RF pulse is considered in many applications,

such as fat suppresion [28], magnetization transfer imaging [4] and chemical exchange saturation transfer [29]. With the STA approximation, the spectral response of the RF excitation comes naturally:

$$M_{xy}(\boldsymbol{r}, f, T) = i\gamma M_0 \int\limits_{t=0}^{T} B_1(t) e^{i2\pi[\boldsymbol{k}(t)\cdot\boldsymbol{r}+k_f(t)f]} dt \qquad (1.2.3)$$

where f denotes the relative frequency relative to the center frequency, and its corresponding excitation k-space is defined as:

$$k_f(t) \triangleq t - T \qquad (1.2.4)$$

Equation (1.2.3) is the signal model for spectral-spatial (SPSP) pulse design in the STA regime, and pulse designers can design RF pulses and gradients for specific target pattern in both the spatial and spectral domain. The predetermined excitation k-space is usually a repeated version of the excitation k-space used for spatial pulses, so that the k_f (time) domain can be covered. By using different numbers of gradient channels, 2D, 3D and 4D SPSP pulse designs have been investigated for different applications, such as water-only slice-select excitation [30], fat saturation [31], and susceptibility artifacts correction [32].

Beyond SPSP pulse design, one can also turn off the gradients so that the spatial specification is dropped, and (1.2.3) becomes the model for spectrally selective pulse design. In this case, the RF pulse in the time domain corresponds to the spectral response in the spectral domain, and applications include fat saturation [28], magnetization transfer imaging [4] and chemical exchange saturation transfer [29].

1.2.3 Iterative STA Pulse Design

In practical RF pulse design, designers need to discretize the signal models to calculate the discrete samples of the RF pulse and gradients for the scanner that uses digital-to-analog converters to convert discrete input to analog signals to the amplifiers and coils. Typically, the RF pulse $B_1(t)$ is uniformly discretized into a train of weighted rectangular impulses, and we fit discrete samples of the space to the signal model. Since similar principles can be applied to the SPSP model (1.2.3), I only discuss the spatial pulse signal model (1.2.1) in this section, and its discrete version is:

$$\boldsymbol{m} \approx A\boldsymbol{b} \tag{1.2.5}$$

where $\boldsymbol{m} = [M_{xy}(\boldsymbol{r}_1, T), \ldots, M_{xy}(\boldsymbol{r}_{N_p}, T)]^T$, $\boldsymbol{r}_1, \ldots, \boldsymbol{r}_{N_p}$ are the uniform spatial domain sample locations, $\boldsymbol{b} = [B_1(t_1), \ldots, B_1(t_{N_t})]^T$, $t_1, \ldots, t_{N_t}$ are the time points of the RF pulse samples, matrix A is in dimension $N_p \times N_t$ with each element $a_{ij} = i\gamma M_0 \Delta t e^{i2\pi[\boldsymbol{k}(t_j)\cdot\boldsymbol{r_i}+(t_j-T)f_0(\boldsymbol{r_i})]}$, and Δt is the sampling interval of the RF pulse.

With this discrete forward model, the pulse design becomes an inverse problem. To solve this problem efficiently using FFT, a Jacobian determinant, which is related to excitation k-space trajectory speed and density [10], has to be calculated when the excitation k-space is not uniformly sampled, which is the traditional non-iterative pulse design [10]. When off-resonance effects are not ignored, the non-iterative method further needs to apply the conjugate phase method [27] which assumes B_0 map varies smoothly and slowly over space.

Yip *et al.* proposed an iterative method for STA pulse design [23], which greatly improves the performance of STA pulse design. Instead of directly calculating the RF pulse, this method tackles the inverse problem with the forward model by iteratively solving an optimization problem. Specifically, they proposed a quadratic cost function that consists of an excitation error term and a regularization term, and the

optimization problem is:

$$\hat{\boldsymbol{b}} = \underset{\boldsymbol{b}}{\mathrm{argmin}} \, \|\boldsymbol{d} - A\boldsymbol{b}\|_W^2 + \beta\|\boldsymbol{b}\|_2^2 \qquad (1.2.6)$$

where $\boldsymbol{d}$ denotes the target excitation pattern, $\|\cdot\|_W$ denotes the weighted l_2 norm that masks out the "don't care" region of the target pattern, and $\beta\|\boldsymbol{b}\|_2^2$ denotes the regularization term that penalizes the RF power and β is a scalar parameter.

By minimizing the cost function with an appropriate value of β, one can achieve the desired balance between the excitation error and the RF power deposition, which is hard to accomplish in the non-iterative method. This convex and quadratic optimization problem can be solved efficiently with many existing optimization algorithms, such as the conjugate gradient (CG) algorithm [23]. There is no need to calculate the Jacobian determinant or use the conjugate phase method. Instead, NUFFT [24] along with time or frequency-segmentation methods [11, 26] can be applied to the forward model and solve the inverse problem efficiently and more robustly. In addition, the iterative method is able to define an region of interest (ROI) in the target pattern to disregard "don't care" regions and produce more degrees of freedom in the design compared to the non-iterative methods. Furthermore, the iterative method is particularly useful for the cases when only the magnitude of the target pattern is of interest, such as saturation pulses [33] and reduced-field-of-view (rFOV) excitation [34]. Then the magnitude least squares method [35] can be applied to relax the phase of the target pattern, which can greatly improve the pulse design performance.

1.3 MRI Parallel Excitation

1.3.1 Introduction

We assume uniform B_1 field in the previous sections, but it is usually not the case in practice, especially in high field ($\geqslant 3T$) scanners. Many pulse design methods

have been proposed for B_1 inhomogeneity correction, e.g., [36–38]. However, existing B_1 inhomogeneity correction methods with single-channel excitation usually require long pulse length and/or high RF power deposition, because the spatial variations are corrected with the help of the compensating spatial variations produced by linear gradients which can be inefficient for some tasks. This problem can be largely mitigated with parallel excitation system which uses multiple surface coils to transmit B_1 field independently. The B_1 field of each transmit coil is non-uniform and stronger near the corresponding coil. The coils are usually placed in circularly symmetric positions in the transverse plane and have uniform B_1 magnitude along the longitudinal direction. Figure 1.3.1 shows an example of an eight-channel parallel excitation system where the B_1 magnitude and phase maps are both displayed. The spatial variations produced by the multiple independent parallel excitation coils can improve efficiency of the RF pulses and therefore reduce the required pulse length, such as in the applications of B_1 inhomogeneity correction [39, 40]. In addition, parallel excitation has also been used for applications that are impractical with single-channel excitation, such as susceptibility artifacts corrections [22, 32, 41] and reduced FOV excitation [34, 42].
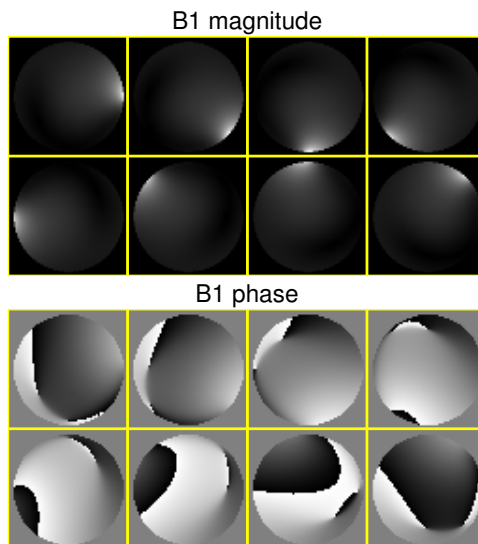
Figure 1.3.1: Example of the B_1 magnitude (top) and phase (bottom) maps of an eight-channel parallel excitation system.

If $S_n(\boldsymbol{r})$ denotes the B_1 field map, aka B_1 map or transmit sensitivity map, of the nth parallel excitation coil, then the composite B_1 field map produced by all the coils is simply the superposition of the B_1 map produced by each individual coil:

$$S_{PEX}(\boldsymbol{r}, t) = \sum_{n=1}^{N} S_n(\boldsymbol{r}) b_n(t) \tag{1.3.1}$$

where $S_{PEX}(\boldsymbol{r}, t)$ denotes the composite B_1 field that can change over time, N is the number of coils, and $b_n(t)$ denotes the RF pulse of the nth channel.

1.3.2 Parallel Excitation Pulse Design

Based on the signal model (1.2.1) and the equation (1.3.1), the signal model for the parallel excitation pulse design with STA approximation is:

$$M_{xy}(\boldsymbol{r}, T) = i\gamma M_0 \sum_{n=1}^{N} S_n(\boldsymbol{r}) \int_0^T b_n(t) e^{i2\pi[\boldsymbol{k}(t)\cdot\boldsymbol{r} + (t-T)f_0(\boldsymbol{r})]} dt \tag{1.3.2}$$

This signal model can be discretized similarly as in (1.2.5). Non-iterative methods [43, 44] have been proposed to design parallel excitation pulses. In general, iterative methods [34] are still preferred, due to the similar reasons mentioned in Section 1.2.3. Similar to the methods for single-channel excitation, the iterative parallel excitation design also conducts an optimization problem that balances the excitation errors and RF power:

$$[\hat{\boldsymbol{b}}_1, \ldots, \hat{\boldsymbol{b}}_N] = \operatorname*{argmin}_{[\boldsymbol{b}_1, \ldots, \boldsymbol{b}_N]} \left\| \boldsymbol{d} - \sum_{n=1}^{N} \boldsymbol{S}_n A \boldsymbol{b}_n \right\|_W^2 + \beta \sum_{n=1}^{N} \|\boldsymbol{b}_n\|_2^2 \tag{1.3.3}$$

where $\hat{\boldsymbol{b}}_n$ denotes the discrete version of the RF pulses of the nth channel, and $\boldsymbol{S}_n$ is a diagonal matrix whose diagonal entries are samples of $S_n(\boldsymbol{r})$.

There are also many methods proposed to design Large-tip angle (LTA) parallel

excitation pulses [13–17], where no simple analytical model exists for the design. I briefly review the additive angle method [14] which is discussed in Chapter IV. It is an iterative method that designs LTA parallel excitation pulses with a series of iterative STA parallel excitation designs [34] interleaved by Bloch equation simulations. It usually converges with a small number of Bloch equation simulations. Specifically, the design initially applies a STA design for the LTA target pattern, $\theta^{\text{des}}(\boldsymbol{r})$, to obtain the initial pulses, $\boldsymbol{b}_1^{(1)}, \ldots, \boldsymbol{b}_N^{(1)}$, and Bloch simulator generates the excited complex pattern, $\theta(\boldsymbol{r})^{(1)} e^{i\angle M_{xy}(\boldsymbol{r})}$; then new pulses, $\boldsymbol{b}_1^{(2)}, \ldots, \boldsymbol{b}_N^{(2)}$, are designed with STA method for the target pattern, $\theta^{(1),\text{new}}(\boldsymbol{r}) e^{i\angle M_{xy}(\boldsymbol{r})}$ where $\theta^{(1),\text{new}} \triangleq \theta^{\text{des}}(\boldsymbol{r}) - \theta^{(1)}(\boldsymbol{r})$, and the new pulses are added to the initial pulses; the summed pulses replace the initial pulses in the next iteration, and the target pattern for the STA design in that iteration is still the difference between the excited pattern and the final target pattern. Iterations continue until a certain convergence criterion is met.

1.3.3 Practical Considerations

Despite of the improved performance over single-channel excitation, parallel excitation still has some potential issues in practice which are actively being investigated in MRI research. First of all, the computation intensity is definitely higher than the single channel pulse design, as it has bigger system matrices and more pulses to compute. This can potentially be mitigated by parallel computing, as the typical STA parallel excitation is highly parallelizable.

Second, parallel excitation design requires measuring the B_1 maps of all the coils, which traditionally can be time consuming or inaccurate [45]. Moreover, B_1 field of the same hardware tends to be object-dependent especially at high field strengths, so online B_1 mapping for every subject may be required. Several methods have been proposed to acquire B_1 fast and accurately [1,46,47]. This topic is discussed in details in Section 1.4 and Chapter III.

Another issue with parallel excitation is the excitation k-space design which is typically predetermined based on Fourier analysis in single-channel excitation. Unlike the single-channel excitation, the relation between the parallel excitation pulses and the target pattern is no longer Fourier-like, so optimization of the excitation k-space of parallel excitation pulses is more desirable than the single-channel excitation. Gradient waveform design is generally hard due to its nonlinearities and hardware constraints, but there are several methods proposed to optimize particular types of trajectories [19–22].

In addition, compared to single-channel excitation, the specific absorption rate (SAR) may be more problematic in parallel excitation. SAR indicates the RF energy deposition to human body, so it is a crucial safety index. SAR increases with the main field strength, so it is more problematic at high fields, e.g., 3T and 7T. Two types of SAR are usually considered for MRI scans, global SAR and local SAR. The former indicates the integrated SAR over the whole body, and the latter indicates the SAR of each local region of the body. Global SAR is generally easier to compute than local SAR, as it requires fewer parameters to calibrate [48], but local SAR is the more direct index for RF heating in the body. So far, there is still no well-accepted method for measuring local SAR. The difficulty is mainly that SAR is related to electric field instead of magnetic field in the scanner and electric field can not be measured directly with MRI in general. For parallel excitation in particular, it brings both opportunities and challenges for the SAR problem. Flexibility produced by parallel excitation for the design of excitation patterns may induce unpredictable electric field distribution and thus may cause local SAR problems; on the other hand, parallel excitation also brings flexibility to better manipulate local SAR distributions and may be optimized to have even lower local SAR than the single-channel excitation. So SAR management in parallel excitation system is an interesting and challenging research area.

1.4 B_1 Mapping

1.4.1 Introduction

As mentioned in Section 1.3.3, B_1 mapping is required for parallel excitation pulse design. It is also useful for many applications using single-channel excitation system where B_1 inhomogeneity can not be ignored, such as B_1 inhomogeneity correction [36] and quantitative MRI [49]. Since B_1 map is object dependent and needs to be acquired for every subject in real time, B_1 mapping methods need to be fast. However, it is generally not easy to measure B_1 maps efficiently, because B_1 field is often highly coupled with some tissue parameters, e.g., T_1, in MRI signal models (see Section 1.5.1).

Existing B_1 mapping methods can be classified into magnitude-based methods and phase-based methods which obtain B_1 maps based on the magnitude and phase of MRI signal respectively [1]. Most B_1 methods are magnitude based, such as double-angle method [45], stimulated echo method [50], signal null method [51], actual flip angle imaging [46] and DREAM [47]. However, those methods may suffer from various problems, such as T_1-dependence, long acquisition time, limited dynamic/effective ranges, or high SAR. There are also several phase-based B_1 methods, such as [52] which requires long acquisition time and [53] which may require high SAR.

Note that "B_1 mapping" typically means measuring B_1 magnitude maps, which is what we usually care about in single-channel excitation imaging. In parallel excitation, however, the B_1 phase of each coil relative to one of the coils, aka relative B_1 phase map, is required. Relative B_1 phase maps are typically measured by successively exciting the same object with each coil and receiving the signal by one common coil or one common set of coils.

1.4.2 Bloch-Siegert B_1 Mapping

Sacolick *et al.* proposed *Bloch-Siegert* (BS) B_1 mapping which applies off-resonance RF pulses in between the excitation pulses and the readout gradients [1]. This phase-based method measures B_1 magnitude using off-resonance RF pulses to induce B_1-related phase shifts which is called *Bloch-siegert (BS) shift* [54]. This method is popular because it is fast and relatively accurate in a wide dynamic range and it is insensitive to T_1, chemical shift, B_0 field inhomogeneity and magnetization transfer effect [1]. Its speed and wide dynamic range are especially beneficial for parallel excitation systems where B_1 mapping is generally more time-consuming and has wider ranges of B_1 magnitude than single channel systems.
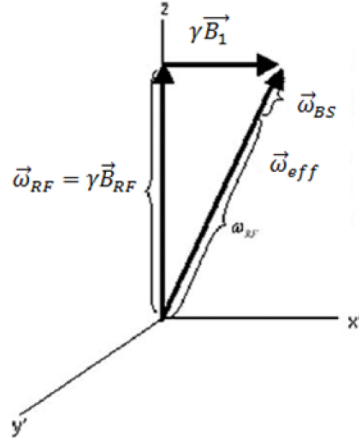
Figure 1.4.1: Illustration of Bloch-Siegert Shift (modified from the Fig.1 in [1]). The B_1 rotating frame rotates at frequency $\omega_0 + \omega_{RF}$, and the spins rotates at ω_{RF}. ω_{BS} is the Bloch-Siegert shift.

In the BS B_1 mapping sequence, when an off-resonance B_1 field is applied, we can observe the behaviors of spins in the B_1 rotating frame where the off-resonance B_1 field is static and the on-resonance spins precess about z axis at the off-resonance frequency of the B_1 field, i.e., ω_{RF}, which is shown in Figure (1.4.1). Hence, effectively the precession of spins in this frame is caused by a virtual field $\vec{B}_{RF}$ such that $\vec{\omega}_{RF} = \gamma \vec{B}_{RF}$, and then the on-resonance spins precess at an effective angle speed $\vec{\omega}_{eff} =$

$\gamma \vec{B}_{RF} + \gamma \vec{B}_1$. One important condition is $\omega_{RF} \gg \gamma B_1$, so that when back to the conventional rotating frame, the on-resonance spins precess about the z axis at the frequency ω_{BS}, i.e., the so-called BS shift:

$$\omega_{BS} = \omega_{eff} - \omega_{RF} = \sqrt{\omega_{RF}^2 + (\gamma B_1)^2} - \omega_{RF} \approx \frac{(\gamma B_1)^2}{2\omega_{RF}} \qquad (1.4.1)$$

So the BS shift is approximately proportional to B_1^2 if ω_{RF} is known. To image the BS shift, we image the accumulated phase induced by an off-resonance RF pulse, which is called *BS pulse*. The BS shift induced phase $\phi_{BS}(\boldsymbol{r})$ could be described as:

$$\phi_{BS}(\boldsymbol{r}) = \int_0^T \frac{(\gamma B_1(\boldsymbol{r}, t)))^2}{2\omega_{RF}(t) - \omega_0(\boldsymbol{r})} dt = K_{BS}(\boldsymbol{r}) B_{1,p}^2(\boldsymbol{r}) \qquad (1.4.2)$$

where $B_1(\boldsymbol{r}, t)$ denotes the spatially and temporally varying B_1 field, $\omega_{RF}(t)$ could be fixed or temporally varying as long as $\omega_{RF}(t) \gg \gamma B_1(\boldsymbol{r}, t)$, $\omega_0(\boldsymbol{r})$ is the B_0 map, $B_{1,p}(\boldsymbol{r})$ is the peak values of $B_1(\boldsymbol{r}, t)$ over time, $B_1(\boldsymbol{r}, t) = B_{1,p}(\boldsymbol{r}) B_{1,n}(t)$, and $K_{BS}(\boldsymbol{r}) \triangleq \int_0^T \frac{(\gamma B_{1,n}^2(t)}{2\omega_{RF}(t) - \omega_0(\boldsymbol{r})} dt$. $B_{1,p}(\boldsymbol{r})$ is the desired B_1 map, and $K_{BS}(\boldsymbol{r})$ is determined by the BS pulse and B_0 map.

As shown previously, BS shift requires spins to have transverse components, so BS pulse is played after an excitation pulse and before the readout. Typically, $\omega_{RF}(t)$ and $B_{1,n}^2(t)$ are chosen such that the BS pulse has negligible direct excitation while $K_{BS}(\boldsymbol{r})$ is large enough to produce detectable phase shifts $\phi_{BS}(\boldsymbol{r})$. An example in [1] was: $\omega_{RF}(t) = 4$ kHz, $B_{1,n}^2(t)$ is a 8 ms long Fermi pulse [4].

B_1 map calculation from the reconstructed image is complicated by the B_0 map in (1.4.2). In addition, the image phase contains not only the BS phase but also the background phase induced by off-resonance effect and the object itself. It is suggested in [1] that one acquires two scans with BS pulses at $\pm \omega_{RF}(t)$ frequencies respectively. Assuming $\omega_{RF}(t) \gg \omega_0(\boldsymbol{r})$, $B_{1,p}^2(\boldsymbol{r})$ is approximately proportional to the

phase difference between the images acquired with those two scans:

$$\phi_{BS,+\omega_{RF}}(\boldsymbol{r}) - \phi_{BS,-\omega_{RF}}(\boldsymbol{r}) \approx \int\limits_{0}^{T} \frac{(\gamma B_1(\boldsymbol{r},t)))^2}{\omega_{RF}(t)} dt = 2K_{BS}B_{1,p}^2(\boldsymbol{r}) \qquad (1.4.3)$$

where $K_{BS} \triangleq \int_{0}^{T} \frac{(\gamma B_{1,n}^2(t)}{2\omega_{RF}(t)} dt$ which is a user-designed constant, and the derivation is based on a 2nd-order Taylor expansion [1].

BS B_1 mapping has been a well-accepted method that is being built into some commercial products. However, a disadvantage of this phase-based method is that the B_1 field estimation in low magnitude regions may suffer from low signal-to-noise ratio (SNR), due to insufficient excitation or low spin density. This is more problematic in B_1 mapping of parallel excitation systems which have more localized B_1 sensitivities. This thesis proposes methods to mitigate this problem for parallel excitation B_1 mapping, which is shown in Chapter III.

1.5 MRI Signal Model and Image Reconstruction

1.5.1 MRI Signal Model

In this section, we introduce physics and signal models of the spin behaviors after the RF excitation in MRI. After the spins are tipped down, the spins precess about the z axis at the Lamor frequency of the main field, but they do not stay in this state forever. The longitudinal component of the spins, $M_z(\boldsymbol{r},t)$, recovers and the transverse component, $M_{xy}(\boldsymbol{r},t)$, decays while precessing, and the spins eventually return to the equilibrium, M_0. These are called *longitudinal relaxation* and *transverse relaxation* respectively, which are modeled by exponential functions of time over the *spin-lattice time constant*, aka T_1, and time over the *spin-spin time constant*, aka T_2, respectively:

$$M_z(t) = M_0 - [M_0 - M_z(0)]e^{-t/T_1} \qquad (1.5.1)$$

$$M_{xy}(t) = M_{xy}(0)e^{-t/T_2} \tag{1.5.2}$$

T_1 is typically on the order of seconds or hundreds of millisecond, and T_2 is typically much shorter and is on the order of tens of millisecond. Before the spins return to equilibrium, the spins are manipulated by the temporally varying linear gradients to generate the desired signal during the readout. The gradients generate linear B_0 field variations over space to encode the signals from different spatial locations. The manipulation of the gradients often generates one particularly large signal, called *echo*, which corresponds to the moment when all of the spins are in-phase or close to in-phase, and the duration between this time point and the excitation is called *echo time*, aka T_E. Most standard pulse sequences do not acquire all the data for a multi-dimensional image with one readout, so the pulse sequence typically is repeated several times with the same excitation and different gradient waveforms for a complete imaging, where the period of each sequence is called *repetition time*, aka T_R. During the readout, the receive coils acquire high frequency signals that are demodulated to be baseband signals afterwards. By some reasonable approximations, the ideal MRI signal can be modeled as:

$$s(t) = \int m(\boldsymbol{r})e^{-i2\pi(\boldsymbol{k}(t)\cdot\boldsymbol{r}+tf_0(\boldsymbol{r}))}d\boldsymbol{r} \tag{1.5.3}$$

where $s(t)$ is the temporally varying signal, $m(\boldsymbol{r})$ is the image which is complex-valued and related to spin density, T_1, T_2, possible off-resonance effects, receive coil sensitivities and sequence parameters like T_E and T_R, and $\boldsymbol{k}(t) \triangleq [k_x(t), k_y(t), k_z(t)]$ denotes the *k-space* as opposed to the excitation k-space defined in (1.2.2), and k-space is defined as:

$$k_x(t) \triangleq \frac{\gamma}{2\pi} \int_0^t G_x(\tau)d\tau \tag{1.5.4}$$

where x can also be y or z for the other two directions. Similar to the STA excitation, the image $m(\boldsymbol{r})$ is the inverse Fourier transform of the signal if gradients are predetermined and off-resonance effects can be ignored. As $m(\boldsymbol{r})$ depends on imaging parameters, it can be manipulated to have the desired contrast between tissues by designing the pulse sequences. Typical image contrasts include spin-density-weighted contrast, T_1-weighted contrast and T_2-weighted contrast.

1.5.2 Image Reconstruction

Due to the Fourier-like relation between MRI signals and the desired image, gradient waveforms or k-space trajectories during the data acquisition are typically determined based on Fourier analysis. Specifically, k-space is covered symmetrically and the coverage is large enough to produce the desired image resolution; the sampling intervals in the k-space typically satisfy the Nyquist theorem to avoid aliasing in the image domain. Traditionally, the k-space is sampled uniformly and FFT is applied to reconstruct the image efficiently, which is called *Cartesian* sampling. Although this sampling method is robust and most accepted in clinical practice, many non-Cartesian methods have been proposed and they sample the k-space non-uniformly and are more efficient than Cartesian sampling, such as spiral trajectory [55] and radial trajectory [56]. A disadvantage of non-Cartesian methods is the more complicated image reconstruction, as FFT is not applicable for non-uniform k-space data. The non-iterative reconstruction methods for non-Cartesian data require k-space density compensation [57]. For both sampling methods, the reconstruction results are susceptible to noise. Another complication to MRI reconstruction is B_0 inhomogeneity which can not be ignored in k-space trajectories that take too long in each shot, such single shot spiral imaging [58] and single shot echo-planar imaging (EPI) [59]. As shown in (1.5.3), even for Cartesian sampling, FFT can not be simply used when B_0 inhomogeneity is not ignored. Non-iterative reconstruction with conjugate phase

methods [25] [26] have been proposed to mitigate the field inhomogeneity problems, but these methods highly rely on the assumption that B_0 map is smooth and slowly varying over space.

The advent of model-based iterative reconstruction greatly improves the performance of MRI reconstruction. In MRI reconstruction, noise can be modeled as additive independent and identically distributed (i.i.d.) complex Gaussian noise. Suppose the ideal signal model (1.5.3) is discretized and then the noisy MRI signal model is described as:

$$\boldsymbol{s} = A\boldsymbol{m} + \boldsymbol{\epsilon} \tag{1.5.5}$$

where $\boldsymbol{s}$ is discretized signal, A denotes the system matrix, $\boldsymbol{m}$ is the discretized image, $\boldsymbol{\epsilon}$ is the i.i.d. complex Gaussian noise, the real or imaginary part of every element of $\boldsymbol{\epsilon}$ is distributed as $\mathcal{N}(0, \sigma^2)$, and σ^2 is the variance. Based on this noise model, the *maximum likelihood estimation* (MLE) of the image is described as a least squares form:

$$\hat{\boldsymbol{m}} = \underset{\boldsymbol{m}}{\operatorname{argmin}} \|\boldsymbol{s} - A\boldsymbol{m}\|^2 \tag{1.5.6}$$

This model-based iterative reconstruction converts the traditional non-iterative inverse problem into an iterative method that uses forward model. In other words, the system matrix A contains the forward system model that can handle non-Cartesian sampling and/or field inhomogeneity terms more accurately and more easily. For the non-Cartesian sampling, one can NUFFT [24] and there is no need to compensate for k-space trajectory density; for the field inhomogeneity, more accurate method that does not highly rely on smoothness of B_0 map [11] can replace the conjugate phase methods.

However, this iterative method may still be susceptible to noise, especially for more ill-conditioned problems like parallel imaging [60]. This is problem can be largely mitigated by introducing regularization terms, which is hard or impossible

to be realized in non-iterative methods. Regularization in the reconstruction can greatly improve the conditioning of the problem and thus produces results that are more immune to noise. Essentially, regularization exploits some prior assumptions of the image, such as piece-wise smoothness of medical images and sparsity of medical images in certain domains [61]. The regularized iterative MRI reconstruction can be described as:

$$\hat{\boldsymbol{m}} = \operatorname*{argmin}_{\boldsymbol{m}} \|\boldsymbol{s} - A\boldsymbol{m}\|^2 + \beta R(\boldsymbol{m}) \tag{1.5.7}$$

where $R(\boldsymbol{m})$ denotes the regularization term and β is scalar regularization parameter that balances between the prior knowledge and data consistency. Popular regularization terms include edge-preserving roughness penalty [62] and total variation regularizer [63]. The minimization in (1.5.7) for MRI reconstruction can be solved iteratively by the many existing optimization algorithms, such as CG algorithm [23], nonlinear CG [61], iterative soft-thresholding [64], iteratively reweighted least squares [65], interior point methods [66] and alternating direction method of multipliers (ADMM) [67]; the choice depends on the specific properties of the regularization terms, such differentiability and convexity.

1.5.3 Compressed Sensing in MRI

Compressed sensing (CS) MRI [61] has become a hot topic in recent MRI reconstruction research, because it can potentially recover accurate images from many fewer k-space samples than required by the Nyquist theorem, and therefore greatly accelerates the MRI data acquisition. It works well in MRI based on the following two assumptions: (a) MR images are sparse in some linear sparse transform domain, e.g., finite difference transform domain, wavelet transform domain or image domain itself; (b) randomly sampled k-space domains and the sparse transform domains are incoherent [61]. Therefore, CS MRI needs to acquire randomly sampled k-space data, which is a type of non-Cartesian sampling. It typically requires an iterative recon-

struction method that enforces sparsity of the images in the sparse transform domain while fitting to the raw data:

$$\hat{\boldsymbol{m}} = \operatorname*{argmin}_{\boldsymbol{m}} \|U\boldsymbol{m}\|_0, \qquad s.t. \quad \boldsymbol{s} = A\boldsymbol{m} \qquad (1.5.8)$$

where U is the sparse transform matrix that transform the image into a sparse transform domain, and $\| \cdot \|$ denotes the l_0 norm. Since l_0 is nonconvex, non-quadratic and non-differentiable, it is very hard to solve this optimization problem. It has been shown that l_1 norm works quite well for CS MRI in practice and could be an alternative to l_0 norm. Furthermore, the data consistency constraint should be relaxed to be under a certain noise level σ. Then the optimization problem for CS MRI is modified to be:

$$\hat{\boldsymbol{m}} = \operatorname*{argmin}_{\boldsymbol{m}} \|U\boldsymbol{m}\|_1, \qquad s.t. \quad \|\boldsymbol{s} - A\boldsymbol{m}\|^2 < \sigma \qquad (1.5.9)$$

This constrained optimization problem can be transformed into its Lagrangian form which is an unconstrained problem:

$$\hat{\boldsymbol{m}} = \operatorname*{argmin}_{\boldsymbol{m}} \|\boldsymbol{s} - A\boldsymbol{m}\|^2 + \beta \|U\boldsymbol{m}\|_1 \qquad (1.5.10)$$

This problem becomes the regularized iterative MRI reconstruction problem (1.5.7) with a special regularization term. With the l_1 based regularization term, this problem can solved easily with iterative soft thresholding [68] or nonlinear CG [61].

Note that the prior knowledge of sparsity is based on the magnitude of medical images, but MR images usually have non-trivial phase variations caused by B_0 inhomogeneity and/or intentional encoding on phase [69, 70]. These phase variations may reduce sparsity of the MR images, and [61] suggests doing phase compensation to mitigate this problem. Specifically, it requires a low-resolution phase estimation

from fully sampled low-resolution k-space data, and the estimated phase information is incorporated into the CS reconstruction:

$$\hat{\boldsymbol{m}} = \underset{\boldsymbol{m}}{\operatorname{argmin}} \|U\boldsymbol{m}\|_1, \qquad s.t. \quad \|\boldsymbol{s} - AP\boldsymbol{m}\|^2 < \sigma \qquad (1.5.11)$$

where P is a diagonal matrix whose diagonal entries are exponentials of the estimated phases. Then the unknown $\boldsymbol{m}$ is closer to being real valued and thus is sparser.

1.6 Fat Suppression

1.6.1 Introduction

Fat is usually not of interest in clinical diagnosis and it inherently has a slightly different on-resonance frequency than water tissue. Thus, it can cause undesired artifacts due to off-resonance effects, such as chemical shift artifacts in Cartesian MRI [6] or blurring artifacts in spiral MRI [71]. In addition, in some applications, e.g., T_1 weighted imaging, fat tissue appears brighter than most tissue, which produces undesired image contrast. Moreover, fat tissue can affect the visualization of its adjacent tissue, such as MR angiography [72] and cartilage imaging [73]. Therefore, fat suppression has been routinely used in many clinical MRI scans.

Fat suppression methods are based on the special properties of fat tissue. First, fat typically has much shorter T_1 values, e.g., about $150 \sim 300$ ms, than normal water tissues which have T_1 values on the order of seconds. So fat can potentially be differentiated from water tissues by its unique T_1. Second, in the spectral domain, although fat has multiple peaks [74], its main spectral peak that takes most of the energy is at about 3.5 parts per million (ppm) lower than the water peak, which corresponds to about 224 Hz at 1.5T or 448 Hz at 3T. The bandwidths of the water and fat spectra are on the order of tens of Hz, so fat can be separate from water in the spectral domain.

1.6.2 Pulse Design Methods

Over the last several decades, various pulse design methods have been proposed to do fat suppression. One popular method is *fat sat(uration)* [28], which is based on the spectral property of fat. This method uses a spectrally selective pulse to first saturate fat spins without exciting water, and then dephases the saturated fat spins using a large trapezoidal gradient waveform, aka *gradient crusher*, so that there is no longitudinal fat magnetization for the following imaging pulse sequences. Fat sat is compatible with most imaging sequences. However, this method is sensitive to B_0 inhomogeneity, because the locations of the fat and water spectra in the frequency domain shift with the local B_0 fields, and a spectrally selective pulse may not be able to accommodate large B_0 inhomogeneity. Even for the case when B_0 inhomogeneity is not too severe, long pulse lengths may be required to handle the widened spectra of fat and water due to B_0 inhomogeneity, e.g., typical fat sat pulse is 10 ms long at 1.5 T and 5 ms at 3T. In addition, fat sat is also susceptible to B_1 inhomogeneity, because ideal fat sat needs to excite all fat spins by 90^0 tip angle which is impossible in the presence of B_1 inhomogeneity.

Another preparatory pulse for fat suppression is Short T_1 Inversion Recovery pulse (STIR) [75] [76], which is based on the unique T_1 of fat. Although this method is immune to B_0 field inhomogeneity, it has many drawbacks, such as long scan time, reduced SNR of water signal, and altered T_1 contrasts.

Instead of preparatory pulses, spectral-spatial (SPSP) pulse was proposed to selectively excite water tissue [30]. This pulse specifies excitation profiles in both spatial and spectral domain, but it is still subject to B_0 inhomogeneity and may have some other drawbacks, e.g., poor slice profile or long pulse length.

1.6.3 Fat-water Separation

There are still several applications where direct visualization of fat is desirable, such as diagnosis of fatty tumors, quantification of visceral adipose tissue and diagnosis of hepatic steatosis [74]. Fat-water separation techniques which produce both water-only and fat-only images are very useful for those applications.

Many fat-water separation methods are post image processing methods based on special image sequences. One class of methods are based on the multiple acquisitions with different echo times such that the behaviors of fat and water spins can be differentiated due to the different resonant frequencies, and they are called *Dixon-based* methods [4,77,78]. These methods decompose water and fat by linear combinations of the images acquired with the multiple acquisitions. The initial two-point Dixon method [77] is susceptible to B_0 inhomogeneity, but this problem is mitigated by methods proposed later [78]. Reeder *et al.* proposed an iterative method called IDEAL (Iterative Decomposition of water and fat with Echo Asymmetry and Least squares estimation) [79], which optimizes the echo times of the multiple acquisitions in terms of noise performance. This method has been shown to be quite robust and can be extended to decompose the multiple peaks of fat.

Another class of fat-water separation methods is based on steady-state free precession (SSFP) sequences [6]. These sequences feature high SNR efficiency and have special signal models in terms of off-resonance frequencies of the spins. These signal models can be manipulated and used for separation of fat and water [80–82]. As this thesis presents a fat-water separation method motivated by the large-angle multiple-acquisition (LAMA) balanced SSFP (bSSFP) method [81] in Chapter VI, we briefly overview LAMA bSSFP in this section. For large-tip-angle ($\sim 50^0$ or greater) bSSFP sequences with 0 or 180^0 phase difference between every two successive RF pulses (called 0 *phase-cycled sequence* and 180^0 *phase-cycled sequence* respectively), their signal models in terms of off-resonance frequency are approximately sine function

and cosine function respectively:

$$S_0(f + f_0) = \sin[\pi T_R(f + f_0)]$$
$$S_{180}(f + f_0) = \cos[\pi T_R(\Delta f + f_0)]$$

(1.6.1)

where S_0 and S_{180} are the signal of the 0 phase-cycled sequence and the 180^0 phase-cycled sequence respectively, and T_R needs to be adjusted such that fat is put at the signal null when water is at the signal peak. Based on these signal equations and B_0 map, $f_0(\boldsymbol{r})$, acquired separately, the water-only image, $W(\boldsymbol{r})$, and the fat-only image, $F(\boldsymbol{r})$, can be calculated by linearly combining the two bSSFP images, $S_0(\boldsymbol{r})$ and $S_{180}(\boldsymbol{r})$:

$$F(\boldsymbol{r}) = S_0(\boldsymbol{r})\cos[\pi T_R f_0(\boldsymbol{r})] - S_{180}(\boldsymbol{r})\sin[\pi T_R f_0(\boldsymbol{r})]$$
$$W(\boldsymbol{r}) = S_0(\boldsymbol{r})\sin[\pi T_R f_0(\boldsymbol{r})] + S_{180}(\boldsymbol{r})\cos[\pi T_R f_0(\boldsymbol{r})]$$

(1.6.2)

1.7 Fast Imaging in the Steady-State

Typical MRI sequences have T_R values on the order of T_1 values or even longer, i.e., hundreds of milliseconds. As imaging time is one of the limitations of MRI, many fast MRI methods have been proposed to reduce MRI scan time. One type of fast MRI techniques use very short T_R and is called fast imaging in the steady-state, aka *steady-state imaging*. The T_R values of the steady-state imaging sequences are usually on the order of T_2 values or even shorter, namely, from several milliseconds to tens of milliseconds. These sequences can be classified into *steady-state coherent* (SSC) sequences and *steady-state incoherent* (SSI) sequences, based on whether or not the transverse magnetization goes naturally to steady-state between successive RF pulses [6].

1.7.1 Steady-State Incoherent Sequences

The SSI sequences are based on the elimination of any residual transverse magnetization before the next RF pulse [6]. One classic SSI sequence is *spoiled gradient-echo sequence* (SPGR), aka FLASH or T1-FFE. This sequence is a gradient-echo sequence with short T_R as well as gradient crushers and RF spoiling to eliminate any transverse magnetization at the end of each repetition. This sequence is typically used for T_1-weighted imaging. Figure 1.7.1 illustrates one repetition of a SPGR sequence where the gradient-echo readout has balanced gradients and there is a large gradient crusher to dephase the intra-voxel spins at the end of each repetition. For sequences with T_R longer than T_2, gradient crushers are usually sufficient to eliminate all the remnant transverse magnetization before the next RF excitation, but it is not the case when $T_R < T_2$. Although with gradient crushers, the signals of the dephased spins in each voxel cancel with each other completely, the transverse components of the spins are still coherent and do not disappear by T_2 decay, so they may be refocused in later repetitions. Thus, additional operations are still needed to completely eliminate the transverse magnetization at the end of each repetition.
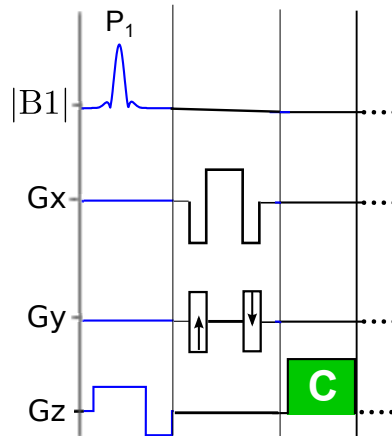
Figure 1.7.1: An illustration of SPGR sequence: a gradient-echo sequence with balanced gradients as well as gradient crushers and RF spoiling.

One well-accepted method is *RF spoiling* which spoils nearly all the transverse

magnetization by varying the bulk phase of the RF pulse over repetitions [83]. RF spoiling makes the dephased spins incoherent and then eliminates the signals from them, and thus none of the transverse component of the spins are in steady states. However, the net signal of each voxel still needs to reach a steady state to produce consistent data in each repetition. According to [83], to maintain the steady state of all voxels at the end of each repetition, the net areas of the gradients should be the same, hence the phase-encoding gradients have to be balanced. Suppose the change of the bulk phase of the nth RF pulse is denoted as $\psi_{\mathrm{rf}}(n)$, so the phase of any refocused magnetizationprior to the nth RF pulse is:

$$P_n = \sum_k [\psi_{\mathrm{rf}}(n-k) + \psi_{\mathrm{g}}(\boldsymbol{r})] - \sum_j [\psi_{\mathrm{rf}}(n-j) + \psi_{\mathrm{g}}(\boldsymbol{r})] \tag{1.7.1}$$

where $\psi_{\mathrm{g}}(\boldsymbol{r})$ denotes the phase change of spins by gradients in the nth repetition and it is a function of spatial locations but not of n as the net gradient areas are fixed in each repetition, and the phase terms in $\sum_j [\cdot]$ with negative sign in front denotes the repetitions where these spins experience the odd number of "pancake-like" flipping by the RF pulse. To be refocused, these spins need to experience zero phase from the gradients, so we have:

$$0 = \sum_k \psi_{\mathrm{g}}(\boldsymbol{r}) - \sum_j \psi_{\mathrm{g}}(\boldsymbol{r}) = \psi_{\mathrm{g}}(\boldsymbol{r})(K - J) \tag{1.7.2}$$

where K and J denote the numbers of the terms in $\sum_k[\cdot]$ and $\sum_k[\cdot]$ respectively, and $K = J$. To have the spins to reach steady state, P_n needs to be independent of n, so we have:

$$P_n = \sum [\psi_{\mathrm{rf}}(n-k) - \psi_{\mathrm{rf}}(n-j)] \tag{1.7.3}$$

28

Since k and j are arbitrary, the following equation must be satisfied:

$$\psi_{\text{rf}}(n - k) - \psi_{\text{rf}}(n - j) = \text{independent of } n \qquad (1.7.4)$$

Thus, $\psi_{\text{rf}}(n)$ should be a linear function of n:

$$\psi_{\text{rf}}(n) = an + b \qquad (1.7.5)$$

where a and b are constants. As P_n is the phase change in the nth RF pulse, the bulk phase of the RF pulses should be an quadratic function of n. So far, we only obtain the conditions for the sequence with RF spoiling to reach steady state, and more conditions are needed to guarantee that the refocused spins at the end of each repetition is close to zero. In [83], empirical simulations show that the desired spoiling can be achieved by setting a to be certain values and the results are not sensitive to tissue types but the flip angle needs to be within a certain range. $a = 117^0$ is one of the well accepted values for SPGR sequences.

Since there is no transverse magnetization residual prior to the new RF pulse, SSI sequences typically have good compatibility with magnetization preparation, such as fat saturation and magnetization transfer [4].

1.7.2   Steady-State Coherent Sequences

For the SSC sequences, both the transverse and longitudinal magnetization components at the end of each repetition contribute to the signal in the next cycle and no spoiling technique is used [6]. Typical SSC sequences include steady-state free precession with free induction decay (SSFP-FID), aka GRASS, FISP or FFE, SSFP-Echo, aka PSIF, SSFP or T2-FFE, and balanced SSFP (bSSFP), aka TrueFISP, FIESTA or b-FFE [6]. Due to the contribution of the unspoiled transverse magnetization, SSC sequences typically have some T_2 contrast in addition to T_1 contrast. In addition,

as spins are coherent over different repetitions, SSC sequences are less interruptible and thus are less compatible with magnetization preparations that are played in each repetition.
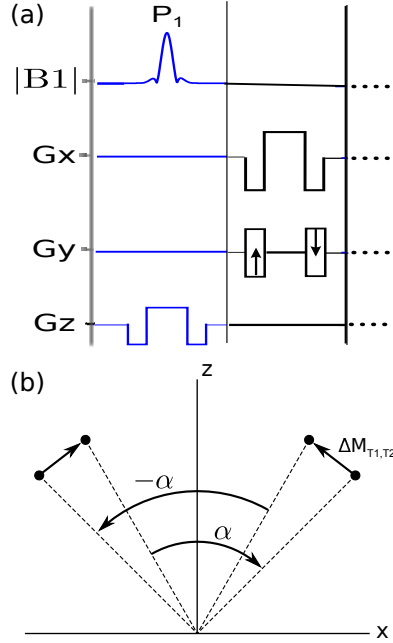
Figure 1.7.2: An illustration of bSSFP sequence. (a) One repetition of the sequence where there are no gradient crushers and RF spoiling, and all the gradients are balanced; (b) The path of the magnetization in steady state during bSSFP scans where α denotes the flip angle and $\Delta M_{T_1,T_2}$ represents the T_1 and T_2 relaxations (from Fig. 2 in [2])

In this section, I only briefly review the bSSFP sequence mentioned in later chapters. Figure 1.7.2 illustrates one repetition of bSSFP sequence where all the gradients are balanced with zero net areas and there are no gradient crushers and RF spoiling. The path of the magnetization in steady state during bSSFP scans is also shown in Figure 1.7.2 where α denotes the flip angle and $\Delta M_{T_1,T_2}$ represents the T_1 and T_2 relaxations. As the magnetization in bSSFP are used very efficiently, bSSFP has the highest SNR efficiency of all known sequences [84]. The contrast of bSSFP is T_2/T_1 weighted which usually produces good fluid-tissue contrast. One drawback of bSSFP is that it is sensitive to B_0 inhomogeneity. When the off-resonance frequency f_0 is

such that $T_R f_0$ is about odd multiples of $\frac{1}{2}$, the signal intensity drops off to near zero, and thus the spatially smooth B_0 map usually produces smoothly distributed dark bands in the image, which are called *banding artifacts*.

1.7.3 Small-Tip Fast Recovery Imaging
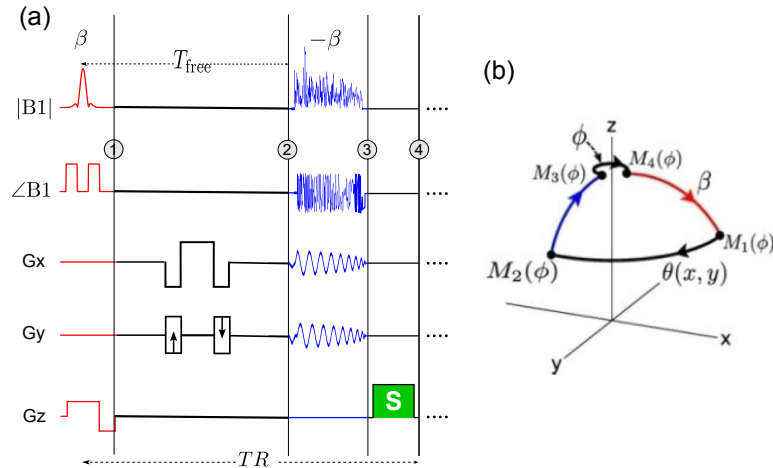
Figure 1.7.3: An illustration of STFR sequence (figures are from J-F Nielsen from The University of Michigan). (a) One repetition of the sequence: all the gradients are balanced, there is one tip-down excitation pulse at the beginning and one tip-up pulse after the readout, β is the tip angle, and there is a gradient crusher at the end and RF spoiling is required; (b) The path of the magnetization in steady state during STFR scans where the subscripts of M correspond to the time points numbered in (a), the spin is tipped down and then tipped back up to the z axis after a free precession time during the readout, and the final gradient crusher and RF spoiling eliminate all the residual magnetization at the end of the repetition.

Nielsen *et al.* [2] have proposed an SSI sequence called small-tip fast recovery sequence (STFR). It produces bSSFP-like T_2/T_1 contrast images which have higher SNR than SPGR images, but they are free of banding artifacts. Figure 1.7.3 illustrates one repetition of the sequence where all the gradients are balanced, there is one tip-down excitation pulse at the beginning and one tip-up pulse after the readout, β is the tip angle, and there is a gradient crusher at the end. In addition, RF

spoiling is required for this version of STFR. Figure 1.7.3 also shows the path of the magnetization in steady state during STFR scans. In each repetition, the spin is first tipped down and is then tipped back up to the z axis after a free precession time, denoted as T_{free}, during the readout. Due to B_0 inhomogeneity, the transverse magnetization precesses during the free precession time at the off-resonance frequency f_0, so the tip-up pulse is a tailored multi-dimensional spatial pulse that is designed to match the phase map of the spins at the end of the free precession time, i.e., $2\pi f_0 T_{free}$, so that those spins are tipped back up to the z axis. However, such tip-up pulses typically do not work perfectly due to T_1 and T_2 relaxations and imperfect pulse design, so a gradient crusher and RF spoiling are required to eliminate any residual transverse magnetization.

With most transverse magnetization recycled by the tip-up pulse, STFR also uses magnetization efficiently and produces high SNR images. As the longitudinal magnetization in the steady state at the beginning of each repetition is related to T_1 and T_2 relaxations of the previous repetition, STFR images have T_2/T_1-like contrasts [2]. Thank to the tailored tip-up pulse, STFR images are free of banding artifacts. In addition, this SSI sequence also has good compatibility with magnetization preparations.

Furthermore, an SSC version of STFR imaging has also been proposed recently [85], which is called G-STFR. It simply removes the RF spoiling of the original STFR sequence so that it becomes a SSC sequence. G-STFR has the same contrast as STFR if there are no errors in the phase map of the excited pattern of the tip-up pulse, which is rarely the case in practice. G-STFR is shown to be less sensitive to such errors than STFR, so it works more robustly in practice [85]. Another interesting feature of G-STFR is that its signal is a triangle-like function of off-resonance frequency when tip-up pulse is set to be the time-reversal version of the tip-down pulse [85]. Chapter VI proposes a fat-water separation method based on this feature.

1.8 Miscellaneous

1.8.1 Cramer-Rao Lower Bound

The Cramer-Rao Lower Bound (CLRB) is a lower bound on the covariance of any unbiased estimator under certain regularity conditions. Suppose $\hat{\theta}(\boldsymbol{X})$ is an unbiased estimator of $\boldsymbol{\theta} \in \mathbb{R}^p$, the measurements $\boldsymbol{X} \sim f(\boldsymbol{x}; \boldsymbol{\theta})$, the distribution function $f(\boldsymbol{x}; \boldsymbol{\theta})$ is differentiable in $\boldsymbol{\theta}$, and the following regularity condition holds:

$$E[\frac{\partial}{\partial \boldsymbol{\theta}} \log f(\boldsymbol{X}; \boldsymbol{\theta})] = \boldsymbol{0} \tag{1.8.1}$$

where $E[\cdot]$ denotes the expectation function. Then the lower bound of the unbiased estimator covariance of $\hat{\theta}(\boldsymbol{X})$ is:

$$\operatorname{cov}[\hat{\theta}(\boldsymbol{X})] \geqslant F(\boldsymbol{\theta})^{-1} \tag{1.8.2}$$

where $F(\boldsymbol{\theta})$ is also known as *Fisher information* and is defined as:

$$F(\boldsymbol{\theta}) = E\{[\frac{\partial}{\partial \boldsymbol{\theta}} \log f(\boldsymbol{X}; \boldsymbol{\theta})][\frac{\partial}{\partial \boldsymbol{\theta}} \log f(\boldsymbol{X}; \boldsymbol{\theta})]^T\} \tag{1.8.3}$$

1.8.2 Magnetization Transfer Contrast Imaging

Magnetization Transfer Contrast (MTC) Imaging is a special image contrast mechanism that is based on the *magnetization transfer* (MT) effect [4]. MT effect causes MRI signal attenuation due to the interaction between the two pools of hydrogen in human body, namely, free hydrogen protons, e.g., those of fluid, and restricted hydrogen protons , e.g. those of macro-molecules [86]. Specifically, as the restricted protons have much broader spectra, ~ 100 kHz, they have extremely short T_2, $\sim 10 \mu s$, and can not produce any detectable MRI signal; but these protons can be saturated by RF pulses and then exchange magnetization with the free protons, which is the so-

called MT effect. Then the longitudinal magnetization of these free protons decreases and thus the MRI signals are decreased. As the magnitude of MT effect is tissue-type dependent, pulse sequences with MT prep(aration) may produce special image contrasts.

To generate MT effect, MT pulses, which are typically off-resonance pulses, are needed to saturate the restricted protons. To avoid direct excitation to the free protons, MT pulses are typically far off-resonant, e.g., several kHz off-resonance frequency. MT prep can be conducted either only once before a fast steady-state imaging sequence [72], i.e., turbo MT prep, or in each repetition of the imaging sequence [87] like the fat sat sequence, i.e., pulsed MT prep. MTC imaging has many clinical applications, such as brain imaging for diagnosis of multiple sclerosis [88], cartilage imaging [87], cardiac imaging [72], intracranial angiography [89] and breast imaging [90].

1.9 Contributions

This thesis develops methods for fast MRI reconstruction and parallel excitation B_1 mapping, as well as methods of RF pulse design and steady-state imaging sequence design for applications such as fat suppression:

(a) [1]We propose a framework of iterative image reconstruction with separate magnitude and phase regularization where compressed sensing is used for the magnitude and special phase regularizers that are free of phase wrapping are designed for different applications. The proposed method greatly improves the phase image reconstruction while accelerates the data acquisition with compressed sensing.

(b) [2]A modified Bloch-Siegert B_1 mapping is proposed to efficiently acquire both magnitude and phase of the B_1 maps of parallel excitation systems. A regularized

---

[1]See Chapter II and [68, 91]

[2]See Chapter III and [92, 93]

34

method is then proposed to jointly estimate the B_1 magnitude and phase to improve the results in low SNR regions. Furthermore, we propose to optimize the coil combinations in this parallel excitation B_1 mapping sequence based on Cramer-Rao Lower Bound analysis, to improve the quality of the raw data for B_1 estimation.

(c) [3]We propose an efficient 4D spectral-spatial fat sat pulse that uniformly suppresses fat without exciting water in the presence of B_0 and B_1 inhomogeneity with single channel or parallel excitation system. At 3T, we show that the proposed pulse can work much more robustly than the standard spectrally selective fat sat pulse with much shorter pulse length.

(d) [4]We apply the proposed fat sat pulse to steady-state incoherent sequences, namely, SPGR and STFR, using a modified RF spoiling scheme. We tested these proposed sequences on applications like cartilage imaging and MR angiography and demonstrated their ability to simultaneously produce fat suppression and MT preparation. We show that the proposed sequences have less limitation on the minimal T_R and potentially lower the overall SAR.

(e) [5]Motivated by [81], we propose to use the G-STFR sequence to separate water and fat and remove banding artifacts simultaneously.

---

[3]See Chapter IV and [33, 94]
[4]See Chapter V and [95, 96]
[5]See Chapter VI and [97]

CHAPTER II

Separate Magnitude and Phase Regularization via Compressed Sensing [1]

2.1 Introduction

In most MRI applications, only the voxel magnitudes are of interest. However, in applications like field map estimation [98] and phase contrast imaging [69, 70], phase maps also contain important information and need to be accurately estimated. Therefore, we want to reconstruct images with both accurate magnitude and phase components from raw k-space data. Regularized iterative algorithms can reconstruct complex images with certain regularization terms for complex unknowns (the unknown image) based on certain priors, e.g., piece-wise smoothness (Total Variation [63]). Such priors, however, are usually based on properties of the magnitude component of medical images, and may be less suitable when variation of the phase component over space is not negligible. Meanwhile, such reconstructions may not exploit prior knowledge of the phase image which is often different from that of the magnitude image, causing the Signal to Noise Ratio (SNR) of phase image in low magnitude areas to be extremely low. To solve this problem, Fessler *et al.* proposed an iterative reconstruction method [99] in which the phase and the magnitude images are reg-

---

[1]This chapter is based on [91] [68]

ularized for their own features separately, preserving both smoothness of the phase image and resolution of the magnitude image. However, this method cannot handle big jumps in wrapped phase maps, due to non-convexity of the cost function for the phase. Moreover, we have found that when k-space data are undersampled, Compressed Sensing (CS) methods [61] are more effective than the simpler smoothness or edge-preserving regularizers for the magnitude component considered in [99].

Undersampling k-space data is one of the main ways to accelerate MRI acquisitions, e.g., in parallel imaging and in CS. CS has shown good performance in reducing k-space samples by exploiting sparsity of medical images in certain transform domains, e.g., finite differences and wavelet transforms. However, typically the assumption of sparsity is based on the properties of the magnitude component, and CS may not work well when rapid spatial phase variations exist. To mitigate this problem, CS reconstruction methods often use phase estimation [61] to make phase corrected images so that the phase variations are reduced, making images sparser; such estimation is done by acquiring low frequency regions of k-space. A similar idea was introduced in the partial Fourier partially parallel imaging technique [100] which is based on conjugate symmetry in k-space for real images [101]. In that method, the phase corrected image is supposed to be almost real, so its imaginary components energy is constrained to be very low. The performance of both methods relies on a phase map estimation that may require additional acquisition and may not be accurate enough. Meanwhile, such estimation is based on the fact that phase map is spatially smooth, which might not be true in certain applications, e.g., in PRF-shift thermometry [69] and in phase-contrast velocity mapping [70]. In fact, it is contradictory that in the cases when phase correction is most necessary, i.e., rapid spatial phase variation, it is most difficult to estimate phase accurately from low frequency k-space data. Thus, phase correction may not greatly benefit magnitude reconstruction when phase variation is severe. Furthermore, since only low frequency k-space measurements are used,

neither of those methods can reconstruct details in phase images, such as hot spots in thermometry and high velocity arteries in velocity mapping.

Therefore, it is tempting to extend the idea of using separate regularization of the magnitude and phase components by using CS, to improve the reconstruction of both magnitude and phase images while accelerating data acquisitions by undersampling k-space data. This combination theoretically takes advantages of these two techniques by exploiting sparsity of magnitude component and smoothness (or some other features) of phase component. Thus, Zibetti *et al.* proposed new regularization terms to approximate CS regularizer (l_1 norm) for magnitude and first-order roughness penalty for phase in [9], which showed better results than before. This method, however, has several limitations: first, it is only applicable for first-order differences operator in CS regularization, which is usually not the optimal one; second, the phase regularization term is still weighted by its corresponding magnitude, which may cause low SNR in low magnitude areas, in other words, phase is still not regularized independently from magnitude; last, the penalty function for phase is concave when neighboring phase difference is large, e.g., $[\pi/2, 3\pi/2]$, which requires a good initialization for phase.

We propose a reconstruction method that combines CS with separate regularizations for magnitude and phase for more general MRI reconstruction applications. In the framework of the separate regularization in [99], we apply CS regularization for the magnitude image but use a new phase regularizer that is applicable for wrapped phase maps, and we randomly undersample k-space data. Since this framework is general enough to design different regularizers for specific types of phase maps, we developed another type of phase regularizer for applications that have distinct areas on top of smooth background in the phase map, e.g., hot spots in temperature maps and arteries in velocity maps.

In this work, we start with the basic MRI signal model. Then the reconstruction cost functions are discussed in detail by comparing conventional CS method with our

38

proposed method and introducing new phase regularizers with their properties. Next, we discuss the respective optimization algorithms for magnitude and phase. Finally, the proposed method was tested by comparing with conventional phase-corrected CS in both simulation studies and in-vivo data reconstructions; in the simulation studies, we simulated an abdomen thermometry data with hot spots in the phase map; in the *in-vivo* data reconstruction, we acquired velocity mapping data of the femoral artery by a phase-contrast bSSFP sequence on 3T GE scanner.

2.2 Theory

2.2.1 Signal Model

In this work, we only discuss single coil reconstruction, but the algorithms easily generalize to parallel imaging using sensitivity encoding (SENSE) [60]. The baseband signal equation of MRI is the following:

$$s(t) = \int m(\vec{r}) e^{-ix(\vec{r})} e^{-i2\pi \vec{k}(t) \cdot \vec{r}} d\vec{r} \qquad (2.2.1)$$

where $\vec{r}$ is the coordinate in spatial domain, $m(\vec{r})$ is the object "magnitude", $x(\vec{r})$ is the phase map, and $\vec{k}(t)$ is the k-space trajectory. We allow $m(\vec{r})$ to take negative values to avoid any π jumps aborbed into the phase $x(\vec{r})$. We assume a short data acquisition time so that the off-resonance induced phase is contained in $x(\vec{r})$. In MRI scanning, complex Gaussian modeled random noise $\epsilon(t)$ is involved in the detected signal, which is

$$y(t) = s(t) + \epsilon(t) \qquad (2.2.2)$$

where $y(t)$ is the detected signal. For computation, we discretize the signal equation as follows:

$$\boldsymbol{y} = A(\boldsymbol{m}e^{i\boldsymbol{x}}) + \boldsymbol{\epsilon} \qquad (2.2.3)$$

where $y = [y_1, y_2, \ldots, y_{N_d}]^T \in \mathbb{C}^{N_d}$, are the measured data; $A \in \mathbb{C}^{N_d * N_p}$ is the system matrix of MRI, e.g., the discrete Fourier transform (DFT) matrix, $m = [m_1, m_2, \ldots, m_{N_p}]^T \in \mathbb{R}^{N_p}$ is the magnitude image, $x = [x_1, x_2, \ldots, x_{N_p}]^T \in \mathbb{R}^{N_p}$ is the phase image, and $\epsilon = [\epsilon_1, \epsilon_2, \ldots, \epsilon_{N_d}] \in \mathbb{C}^{N_d}$ is the complex noise. (We write $\boldsymbol{m}e^{i\boldsymbol{x}}$ as as shorthand for element-wise multiplication of these two vectors.) In this work, our goal is to reconstruct $\boldsymbol{m}$ and $\boldsymbol{x}$ simultaneously from undersampled k-space data $\boldsymbol{y}$.

2.2.2 Cost Functions

In conventional CS [61], applying a regularized approach for (2.2.3) yields the cost function:

$$\Psi_0(\boldsymbol{f}) = \|\boldsymbol{y} - A\boldsymbol{f}\|^2 + \beta R(\boldsymbol{f}) \qquad (2.2.4)$$

where $\boldsymbol{f} = \boldsymbol{m}e^{i\boldsymbol{x}}$, $\boldsymbol{y}$ denotes randomly undersampled data in k-space, $\| \cdot \|$ denotes l_2 norm, β is the scalar regularization parameter, and $R(\cdot)$ is the CS regularizer; usually, $R(\cdot)$ is the l_1 or l_0 norm of finite differences or a wavelet transform. The estimated magnitude and phase, i.e., $\hat{\boldsymbol{m}}$ and $\hat{\boldsymbol{x}}$ are then computed from the reconstructed complex image $\hat{\boldsymbol{f}}$, where $\hat{\boldsymbol{f}} = \text{argmin}_f \Psi_0(\boldsymbol{f})$.

To reduce phase variation of $\boldsymbol{f}$, phase-correction is often applied to better sparsify the image $\boldsymbol{f}$ in the sparse transform domain [61]:

$$\Psi_1(\boldsymbol{f}_1) = \|\boldsymbol{y} - Ae^{i\boldsymbol{P}}\boldsymbol{f}_1\|^2 + \beta R(\boldsymbol{f}_1) \qquad (2.2.5)$$

where $\boldsymbol{P}$ is the estimated phase map from low frequency k-space, $e^{i\boldsymbol{P}}$ denotes a diagonal matrix whose diagonal entries are exponentials of $\boldsymbol{P}$ in the same order. The unknown $\boldsymbol{f}_1$ should then be closer than $\boldsymbol{f}$ in (2.2.4) to the magnitude image $\boldsymbol{m}$ which

is sparser. The final reconstructed image for conventional CS is:

$$\hat{\boldsymbol{f}} = e^{i\boldsymbol{P}}\hat{\boldsymbol{f}}_1, \hat{\boldsymbol{m}} = |\hat{\boldsymbol{f}}|, \hat{\boldsymbol{x}} = \angle\hat{\boldsymbol{f}} \tag{2.2.6}$$

where $\hat{\boldsymbol{f}}_1 = \operatorname{argmin}_{\boldsymbol{f}_1} \Psi_1(\boldsymbol{f}_1)$.

In this work, this method is used for comparison, and we choose $R(\cdot)$ to be l_1 norm of wavelet transform; then the cost function becomes:

$$\Psi_1(\boldsymbol{f}_1) = \|\boldsymbol{y} - Ae^{i\boldsymbol{P}}\boldsymbol{f}_1\|^2 + \beta\|U'\boldsymbol{f}_1\|_1 \tag{2.2.7}$$

where U is the wavelet transform matrix and $\|\cdot\|_1$ denotes l_1 norm.

In contrast, we propose a cost function with separate regularizations for magnitude and phase components as follows:

$$\Psi_0(\boldsymbol{x}, \boldsymbol{m}) = \|\boldsymbol{y} - A\boldsymbol{m}e^{i\boldsymbol{x}}\|^2 + \beta_1 R_x(\boldsymbol{x}) + \beta_2 R_m(\boldsymbol{m}) \tag{2.2.8}$$

where $R_x(\boldsymbol{x})$ and $R_m(\boldsymbol{m})$ denote the regularizers for $\boldsymbol{x}$ and $\boldsymbol{m}$, β_1 and β_2 denote the scalar regularization parameters. For the magnitude component $\boldsymbol{m}$, we exploit the sparsity of the magnitude in wavelet domain by regularizing the l_1 norm of the wavelet coefficients of $\boldsymbol{m}$. For the phase component $\boldsymbol{x}$, we select the regularizer according to features of the phase map. For a smooth phase map, we use a typical first-order finite differences regularizer (called "regularizer 1" hereafter) to enforce spatial smoothness [99]. The cost function then becomes:

$$\Psi_1(\boldsymbol{x}, \boldsymbol{m}) = \|\boldsymbol{y} - A\boldsymbol{m}e^{i\boldsymbol{x}}\|^2 + \beta_1\|C\boldsymbol{x}\|^2 + \beta_2\|U'\boldsymbol{m}\|_1 \quad \text{(regularizer 1)} \tag{2.2.9}$$

where C is finite differencing matrix that penalizes roughness. Note that the arguments of the cost function are real valued.

Because the phase $\boldsymbol{x}$ appears in an exponential in the data fit term, the cost function is non-convex; indeed, it is 2π periodic. When this term is combined with regularizer 1, it can be difficult for a descent algorithm to find a desirable local minimum, particularly if the range of the true phase map values exceeds a 2π interval. We observed empirically that descent algorithms frequently converged to undesirable local minimizers in this situation. To address this problem, we investigated a different phase regularizer that is also periodic, by regularizing the exponential of the phase instead of the phase itself. This regularizer (called "regularizer 2" hereafter) is described as:

$$R_2(\boldsymbol{x}) = \|Ce^{i\boldsymbol{x}}\|^2 \quad \text{(regularizer 2)} \tag{2.2.10}$$

Note that the unit of $\boldsymbol{x}$ has to be radians here. This regularizer accommodates phase wrapping, because the wrapped phase values will be equivalent to the unwrapped ones when exponentiated [102]. However, this choice introduces some non-linearity to the regularization term, which requires examination. To explore it, we consider an arbitrary pair of neighboring pixels (x_1, x_2) that are penalized in regularizer 2:

$$\left|[Ce^{i\boldsymbol{x}}]_k\right|^2 = |e^{ix_1} - e^{ix_2}|^2 = 2(1 - \cos(x_1 - x_2)) = 2(1 - \cos(t)) \tag{2.2.11}$$

where k corresponds to x_1 and x_2 in regularizer 2, and t is the finite difference $x_1 - x_2$. In contrast, regularizer 1 has this corresponding formula:

$$\left|[C\boldsymbol{x}]_k\right|^2 = (x_1 - x_2)^2 = t^2 \tag{2.2.12}$$

Fig. 2.2.1 compares $2(1 - \cos(t))$ with t^2, $(t - 2\pi)^2$ and $(t + 2\pi)^2$, showing that regularizer 2 approximates regularizer 1 in every period and therefore allows phase wrapping without changing the roughness penalty. As can be seen, the new regularizer is a very good approximation to the old one in intervals between $2n\pi \pm 1.5$ with $n =$
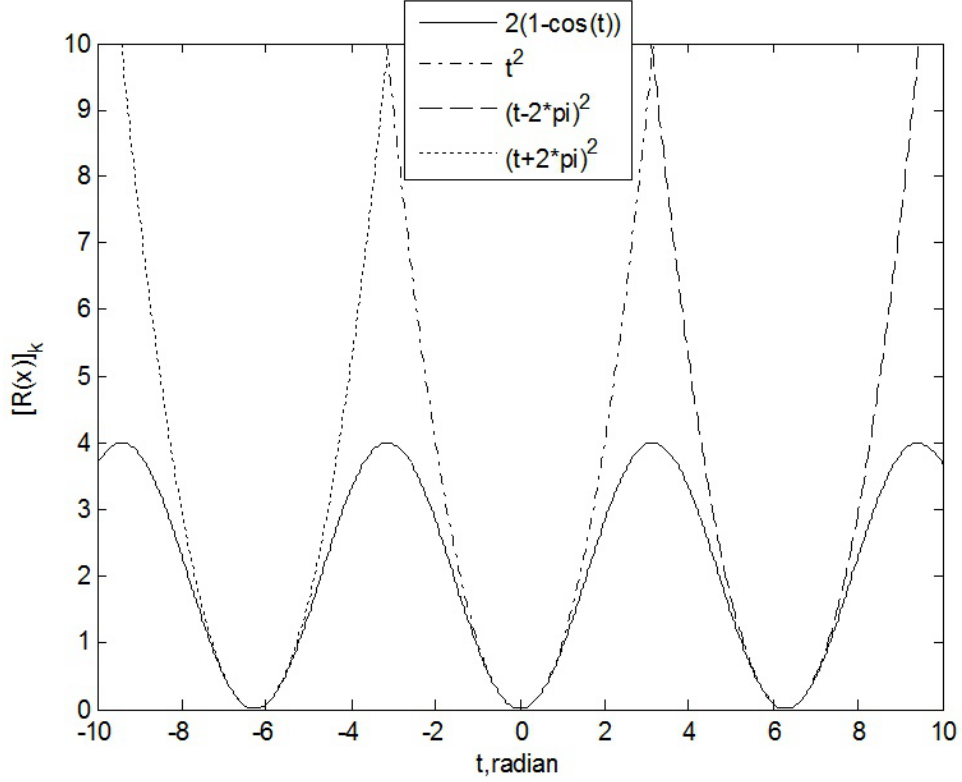
Figure 2.2.1: Comparison between the two regularizers (regularizer 1: t^2; regularizer 2: $2(1 - \cos(t))$.)

all integers, which are sufficiently wide intervals for most MRI phase maps. Therefore, in principle, this regularizer will not only handle the phase wrap but also preserve smoothness of the phase map. Note that $R_x(\boldsymbol{x})$ is concave for large phase differences $(\in (2n\pi + \pi/2, 2n\pi + 3\pi/2))$, which is the same problem in [102]. Fortunately, such problem can be avoided in most cases by choosing a sufficiently good initial phase map for the reconstruction (discussed later in the paper). Therefore, if no extremely sharp edges exist in the true phase map, the value of t in our reconstruction will often be within the convex domain of the regularization term, i.e., $(2n\pi - \pi/2, 2n\pi + \pi/2)$. To sum up, the proposed cost function for typical cases with smooth phase maps is:

$$\Psi_2(\boldsymbol{x}, \boldsymbol{m}) = \|\boldsymbol{y} - A\boldsymbol{m}e^{i\boldsymbol{x}}\|^2 + \beta_1\|Ce^{i\boldsymbol{x}}\|^2 + \beta_2\|U'\boldsymbol{m}\|_1 \quad \text{(regularizer 2)} \quad (2.2.13)$$

Some applications have more complicated phase maps, so only enforcing phase smoothness may be suboptimal. Fortunately, the proposed cost function is general enough to introduce other regularizers that are designed for specific applications. For example, in PRF-shift temperature mapping, phase maps may have hot spots in thermal ablation therapy [69]; in phase contrast velocity mapping, phase maps may have velocity information of arteries which are in systole. In both cases, the phase map will have relatively small distinct areas on top of a smooth background. To estimate such phase maps more accurately, we propose to apply edge-preserving phase regularizers to preserve hot spots or contracting arteries while still smoothing the background.

Although we ultimately want to extend regularizer 2 in this application so that wrapped phase maps could be properly regularized, we start with a conventional edge-preserving regularizer for non-wrapping phase maps, because it can be used in the initialization step which will be discussed later. This edge-preserving regularizer for non-wrapping phase (called "regularizer 3" hereafter) is:

$$R_3(\boldsymbol{x}) = \sum_{k=1}^{K} \psi([C\boldsymbol{x}]_k) \quad \text{(regularizer 3)} \tag{2.2.14}$$

where $\psi(\cdot)$ denotes an edge-preserving potential function, k is the row index, and K is the number of rows of C. For edge preservation, $\psi(\cdot)$ should be non-quadratic and satisfy: $\omega_\psi(t) = \dot{\psi}(t)/t$ is non-increasing and $\lim_{t\to\infty} \dot{\psi}(t) \in (0,\infty)$ [62]. There are many typical edge-preserving potential functions, e.g., hyperbola, Cauchy, Geman & McClure, etc. [62]. Since they are all non-quadratic, it complicates the optimization (shown in Appendix A). Obviously, this regularizer cannot handle wrapped phase, because it will treat phase wraps as edges instead of enforcing smoothness.

Thus, we designed a new regularizer, trying to regularize wrapped phase maps while preserving edges. Incorporated with the edge-preserving potential function in

the regularizer, the new cost function becomes:

$$\Psi_4(\boldsymbol{x}, \boldsymbol{m}) = \|\boldsymbol{y} - A\boldsymbol{m}e^{i\boldsymbol{x}}\|^2 + \beta_1 \sum_{k=1}^{K} \psi(|[Ce^{i\boldsymbol{x}}]_k|) + \beta_2\|U'\boldsymbol{m}\|_1 \quad \text{(regularizer 4)}$$

$$(2.2.15)$$

(This phase regularizer is called "regularizer 4" hereafter). Similar to regularizer 3, there are many choices for potential functions. To illustrate this regularizer, we consider the hyperbola function, which is

$$\psi(s) = \delta^2(\sqrt{1 + |\frac{s}{\delta}|} - 1) \quad (2.2.16)$$

where δ is the parameter to tune how much edge-preserving we need. Note that the unit of x has to be radians, but δ is unitless for regularizer 4. Similar to (2.2.11), the corresponding formula for regularizer 4 is:

$$\psi(|[Ce^{i\boldsymbol{x}}]_k|) = \psi(|e^{ix_1} - e^{ix_2}|) = \psi(\sqrt{2(1 - \cos(t))}) \quad (2.2.17)$$

where $t = x_1 - x_2$. Fig. 2.2.2 compares $[R(\boldsymbol{x})]_k$ of regularizer 1 and regularizer 4. As can be seen in this plot, regularizer 4 does have edge-preserving properties compared to regularizer 1; here $\delta = 0.005$, which was chosen for velocity mapping reconstruction in the next section Similar to regularizer 2, the exponential terms in regularizer 4 makes the cost function non-convex, but we have mitigated this problem by certain strategies that will be discussed in the next section.

Table 2.1: summary of the four regularizers

Regularizer 1	$R_1(\boldsymbol{x}) = \|C\boldsymbol{x}\|^2$
Regularizer 2	$R_2(\boldsymbol{x}) = \|Ce^{i\boldsymbol{x}}\|^2$
Regularizer 3	$R_3(\boldsymbol{x}) = \sum_{k=1}^{K} \psi([C\boldsymbol{x}]_k)$
Regularizer 4	$R_4(\boldsymbol{x}) = \sum_{k=1}^{K} \psi(|[Ce^{i\boldsymbol{x}}]_k|)$
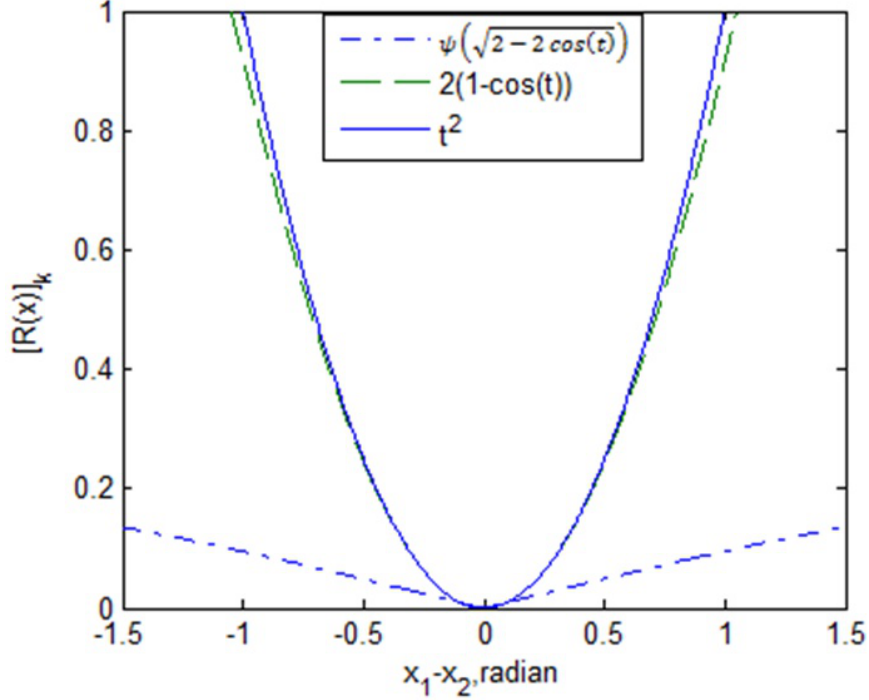
Figure 2.2.2: comparison of regularizer 1: t^2, regularizer 2: $2(1 - \cos(t))$, and regularizer 4: $\psi(\sqrt{(2 - 2\cos(t))})$.

2.2.3 Optimization Algorithms

Our goal is to estimate $\boldsymbol{x}$ and $\boldsymbol{m}$ from data $\boldsymbol{y}$ by minimizing the cost function:

$$(\hat{\boldsymbol{x}}, \hat{\boldsymbol{m}}) = \underset{\boldsymbol{x}, \boldsymbol{m} \in \mathbb{R}^{N_p}}{\operatorname{argmin}} \; \Psi_l(\boldsymbol{x}, \boldsymbol{m}) \qquad (2.2.18)$$

where $l = 1, 2, 3$ or 4, and N_p is the number of pixels in each image. We jointly estimate the phase and magnitude by alternately updating each of them in each iteration:

$$\boldsymbol{x}^{(n+1)} = \underset{\boldsymbol{x} \in \mathbb{R}^{N_p}}{\operatorname{argmin}} \; \Psi_l(\boldsymbol{x}, \boldsymbol{m}^{(n)}) \qquad (2.2.19)$$

$$\boldsymbol{m}^{(n+1)} = \underset{\boldsymbol{m} \in \mathbb{R}^{N_p}}{\operatorname{argmin}} \; \Psi_l(\boldsymbol{x}^{(n+1)}, \boldsymbol{m}) \qquad (2.2.20)$$

There are many optimization algorithms for CS, and we choose to use the iterative

46

soft thresholding (IST) algorithm [62] to update $\boldsymbol{m}$ in (2.2.20). Specifically, we firstly design a separable quadratic surrogate function for the data fit term according to the optimization transfer principle [62], and then use the IST algorithm to minimize the surrogate function. The update formula was derived for real unknowns:

$$\boldsymbol{m}^{(n+1)} = U * \mathsf{soft}\{U' * \boldsymbol{m}^{(n)} + \frac{1}{\check{c}}\mathsf{Re}\{U'A_x'(\boldsymbol{y} - A_x\boldsymbol{m}^{(n)})\}, \frac{\beta_2}{2\check{c}}\} \qquad (2.2.21)$$

where $\mathsf{soft}\{t; \alpha\} = (t - \alpha * \frac{t}{|t|}) * 1\{|t| > \alpha\}$, $\mathsf{Re}\{t\}$ is the real part the complex number t, $A_x \triangleq A * \mathsf{diag}\{e^{x_j^{(n+1)}}\}$, and $\check{c} \triangleq \rho(A'A)$, which is the spectral radius of $A'A$ and e.g., $\check{c} = N_p$ when we use Cartesian sampling.

It is more challenging to update $\boldsymbol{x}$, because the cost function for $\boldsymbol{x}$ is nonlinear and non-convex. One way to approach this problem is to use optimization transfer as in [62]. We have investigated this approach for the cost function with regularizer 1 by using De Pierros trick [103] to design a quadratic surrogate function. However, it turned out to converge very slowly. Although this algorithm may work well for images that are sparse in the image domain, e.g., angiography images, we prefer to minimize the cost function in a more generally practical way. Therefore, we apply preconditioned conjugate gradient with backtracking line search (PCG-BLS) algorithm [62] to mitigate such problem. The updating formula is derived as follows (see Appendix A for details):

$$\boldsymbol{x}^{(n+1)} = \boldsymbol{x}^{(n)} + \hat{\alpha}_n \boldsymbol{d}^{(n)} \qquad (2.2.22)$$

where $\boldsymbol{d}^{(n)}$ is the search direction derived by PCG algorithm [62], $\hat{\alpha}_n$ is the step size α at the nth iteration which is chosen by Newton-Raphson algorithm with backtracking strategy to guarantee monotonicity [62]. The formula of the Newton-Raphson algorithm for updating the step size is:

$$\alpha^{(k+1)} = \alpha^{(k)} - \frac{\dot{f}_n(\alpha^{(k)})}{\ddot{f}_n(\alpha^{(k)})} \qquad (2.2.23)$$

where $f_n(\alpha) = \Psi_l(\boldsymbol{x}^{(n)} + \alpha\boldsymbol{d}^{(n)}, \boldsymbol{m}^{(n)})$. These step size optimization formulas for the four regularizers are shown in Appendix Arespectively. Since this algorithm alone does not guarantee monotonicity, we need to use the backtracking strategy [62] to ensure monotonic decrease of $\boldsymbol{\Psi}_l$.

As one would expect, this nonlinear optimization algorithm has higher computational complexity than conventional CS optimization. For conventional CS by IST, the operations that dominate in each iteration are 2 A-operations, i.e., Fast Fourier transforms, and 2 U-operations, i.e., wavelet transforms. For the proposed method, updating m takes slightly shorter time than conventional CS, because although there are also 2 A-operations and 2 U-operations in each iteration, parts of them are real number operations instead of complex number operations in conventional CS optimization. However, the nonlinear optimization for x in the proposed method is much slower: in each iteration, there are $3N_s$ A-operations $+2N_s$ C-operations, i.e., taking finite difference transform, for computing the gradients, $3N_s * N_a$ A-operations $+3N_s * N_a$ C-operations for the Newton-Raphson updating, and $N_s * N_a * N_b$ A-operations $+N_s * N_a * N_b$ C-operations for the backtracking part, where N_s is the number of sub-iterations in each iteration, N_a is the number of iterations for the line search and N_b-1 is the number of backtracking steps. Empirically, we choose $N_s = 2$, and on average N_a is 2.5 and N_b is about 1.1 on average; therefore, in each iteration, there are about 27 A-operations and 25 C-operations. A-operation is $O(N\log_2 N)$, U-operation and C-operation are both $O(N)$, where N represents N_d, N_p or K. Since we use first order finite difference and 3-level wavelet transform, C-operation is much faster than U-operation. Thus, the proposed method is roughly 10 times slower than conventional CS. However, we still achieve an acceptable computation time by the implementation shown in the appendix; for example, it takes about 55 s to run the proposed method with 120 iterations for the 2D data in the *in-vivo* experiments of Section 2.3.3 on a computer with Intel (R) Core (TM)2 Quad CPU Q9400 @ 2.66GHz,

4GB RAM and Matlab 7.8. For 3D data, a more efficient implementation in C++ may be necessary, but we believe that the computation time can be made acceptable.

As mentioned before, monotonically decreasing a non-convex cost function cannot guarantee finding a global minimizer for x for an arbitrary initial guess; therefore a good initial estimate for the phase image is important. In this study, since the cost function of conventional CS is convex, we set the initial guess for x and m by using the phase and magnitude of the result of conventional CS reconstruction method for complex voxels by IST (the cost function is like (2.2.4)). During this setup, we set the unknowns to be $\boldsymbol{f} = \boldsymbol{m}e^{i\boldsymbol{x}}$, and the initial guess of $\boldsymbol{f}$ is the inverse DFT of zero-padded k-space data; then we use a similar algorithm to (2.2.21) with some modifications:

$$\boldsymbol{f}^{(n+1)} = U * \mathsf{soft}\{U' * \boldsymbol{f}^{(n)} + \frac{1}{\check{c}}A(\boldsymbol{y} - A\boldsymbol{f}^{(n)})), \frac{\beta_2}{\check{c}}\} \qquad (2.2.24)$$

Then we set $\boldsymbol{x}^{(0)} = \angle \boldsymbol{f}^{(n)}$ and $\boldsymbol{m}^{(0)} = |\boldsymbol{f}^{(n)}|$ for $n = 1$ or 2 usually. Such initialization for phase and magnitude turns out to be very good for most cases except for regularizer 4 which has a narrower convex domain. To solve this problem, we take one more step to form the initial guess, which is to use regularizer 2 or 3 for a few iterations, because both of them have wider convex domains than regularizer 4. Then we believe we get the phase map closer to the desired phase map, which can help lead reconstructions using regularizer 4 to a desirable local minimum.

Like all the other regularized reconstruction methods, the regularization parameters should be carefully selected. For the parameter of the roughness penalty term, i.e., β_1, the value can be selected according to the desired spatial resolution of the phase image [98]. However, it is still an open problem for selecting parameters of the l_1 norm term. In this study, we choose the parameter β_2 empirically.

2.3   EXPERIMENTS

2.3.1   Experiment Setup

In our experiments, we compared the performance of the proposed methods with conventional phase-corrected CS that uses the IST algorithm (2.2.24) for optimization. All the data were sampled in the 2D Cartesian grid of k-space. The center of the k-space was fully sampled according to Nyquist sampling theorem, which preserves low frequency information and also allows for phase correction in conventional CS. The rest of k-space was randomly undersampled (as shown in Fig. 2.3.1). Three different image masks are used in the experiments: for reconstruction, we used a "loose" mask that was obtained from the inverse DFT of the raw undersampled data; in the results comparison, we use the true mask that is taken from the true image for a fair evaluation; for evaluation of the regions of interest (ROI), we use the ROI mask that is taken manually from the true phase image and only covers the ROIs. Regularization parameters were empirically chosen to be "the best" for each method, in terms of Normalized Root Mean Square Error (NRMSE) or Root Mean Square Error (RMSE) which were used for magnitude images and phase images respectively. NRMSE and RMSE are defined as below:

$$\text{NRMSE} = \frac{\|\boldsymbol{m}_r - \boldsymbol{m}_t\|}{\|\boldsymbol{m}_t\|} \qquad (2.3.1)$$

$$\text{RMSE} = \frac{\|\boldsymbol{x}_r - \boldsymbol{x}_t\|}{\sqrt{N_p}} \qquad (2.3.2)$$

where $\boldsymbol{m}_r$ and $\boldsymbol{m}_t$ denote the reconstructed and true magnitude images respectively, $\boldsymbol{x}_r$ and $\boldsymbol{x}_t$ denote the reconstructed and true phase images respectively, and N_p is the number of pixels in each image. Moreover, we ran the algorithm until the cost function appeared to reach a minimum. In both methods, the sparse transform matrix

(U) was set to be a 3-level Haar wavelet transform matrix which is unitary.
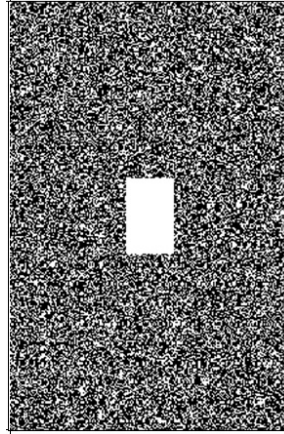
Figure 2.3.1: The sampling pattern in k-space

2.3.2 Experiments with simulated data

We simulated a thermometry scan using an abdomen T_2 weighted magnitude image (upper left most in Fig. 2.3.2). We used the corresponding field map, scaled into the interval $(-2\pi, 2\pi)$, as the background of the true phase map. The true complex image was cropped to be a $320 * 208$ matrix (40 cm $* 26$ cm FOV). To reduce the discretization effects that might happen in the synthesized data, we simulated the data from a higher resolution "true image". Since there is not an analytical expression or a higher resolution version of this simulated object, we synthesized the higher resolution "true image" by linearly interpolating the original true image to be $960 * 624$. In addition, we added four "Gaussian hot spots", the peak values of which are from 3.5 to 4 radians, onto the interpolated background phase map to simulate thermal ablation (lower left most in Fig. 2.3.2). We chose this wide range of phase values to test performance of the proposed algorithm for wrapped phase maps. This "true complex image" is used as an approximation of the continuous phantom. Then we synthesized the fully sampled single-coil k-space data by taking DFT of the "true complex image", and took the k-space data in a $320 * 208$ matrix with

sampling intervals corresponding to 40 cm *26 cm FOV. Then we added Gaussian distributed complex noise to mimic MRI scanner noise, and the noise level was fixed through all these simulation experiments such that the Signal-to-Noise-Ratio (SNR) was approximately 24 dB. The SNR is defined in k-space, which is

$$\text{SNR} = 20 \log(\frac{\|\boldsymbol{y}_t\|}{\|\boldsymbol{y}_t - \boldsymbol{y}\|}) \tag{2.3.3}$$

where $\boldsymbol{y}_t$ denotes the noise-free k-space data, $\boldsymbol{y}$ denotes the noisy k-space data, and both are fully sampled in k-space. Afterwards, the final simulated data were formed by randomly sampling the Cartesian grid, with the center (3%) of the k-space fully sampled, as shown in Fig. 2.3.2. In the experiments, the proposed method and conventional CS approach were tested at different sampling rates ranging from 20% to 60%. Since some referenceless PRF-shift temperature mapping methods [104, 105] have been proposed in literature, it is realistic to just reconstruct a certain frame without considering the reference frame in this simulation study. The reconstruction results are compared by visual inspection as well as NRMSE and RMSE of the reconstructed images with respect to the "low resolution true image". This "low resolution true image" is obtained from the $320 * 208$ fully sampled noiseless k-space data by an inverse DFT. For conventional CS, we estimated the slow-varying reference phase map by taking the inverse DFT of the fully sampled k-space center. The proposed method used the regularizer 4 for the phase map, where we chose hyperbola function as the edge-preserving potential function, i.e., $\psi(t) = \delta^2(\sqrt{1 + |t/\delta|^2} - 1)$ with $\delta = 0.0005$ (radians) chosen empirically. The regularization parameters chosen for the simulation studies are shown in Table 2.2.

Fig. 2.3.3 compares NRMSE of magnitude maps with the true mask (called "entire magnitude" hereafter) and RMSE of phase maps with the true mask (called "entire phase" hereafter) at different sampling rates of conventional CS and the proposed

method. We also compared the RMSE of the phase with the ROI masks, as shown in Fig. 2.3.3 (left), to evaluate the performance of the two methods for the regions around the hot spots, which are more important than other regions. The proposed method reduced NRMSE of the entire magnitude images by $10\% \sim 20\%$, while reduced the RMSE of the entire phase images by about $60\% \sim 70\%$; for the phase in the hot spots, the proposed method achieved about $50\% \sim 60\%$ lower RMSE. Fig. 2.3.2 illustrates the results at 40% sampling rate; the regions outside the object have been masked out. Compared to conventional CS, the proposed method produces a much cleaner background phase map while preserving the hot spots information, especially for the hot spots in the low intensity regions where the important hot spots information is corrupted by noise in the results by conventional CS. However, the reduced NRMSE in the magnitude images is not very visible, which will be discussed in the next section.

To demonstrate the importance of using regularizer 4, we replaced the regularizer 4 by regularizer 1-3 in the proposed method and reconstructed the data with 40% sampling rate. The regularization parameters are shown in Table 2.3, and δ is set to 0.0005 radians for regularizer 3. Fig. 2.3.4 shows the phase maps and phase error maps of the reconstructed results. Regularizer 1 and regularizer 3 cannot handle the phase wrapped regions and tend to enhance the phase wrapping boundaries due to the smoothing within different convex domains; therefore, it is reasonable that regularizer 3 makes less "jumps" over the phase wrapping boundaries than regularizer 1 does. As expected, regularizer 2 tends to over-smooth the hot spots, especially the one pointed by the arrow; however, as shown in Fig. 2.2.1, regularizer 2 still has some edge-preserving effect, so the result by regularizer 2 was not far from the true phase; but it still not as good as the result by regularizer 4 (shown in Fig. 2.3.2). Table 2.3 also shows the RMSEs of ROI in the phase maps by regularizer 1-4. For initializing the proposed method, we believe that the results obtained by regularizer 2 or 3 tend

to be in the convex domain that contains desired local minimum of the ultimate cost function with regularizer 4.
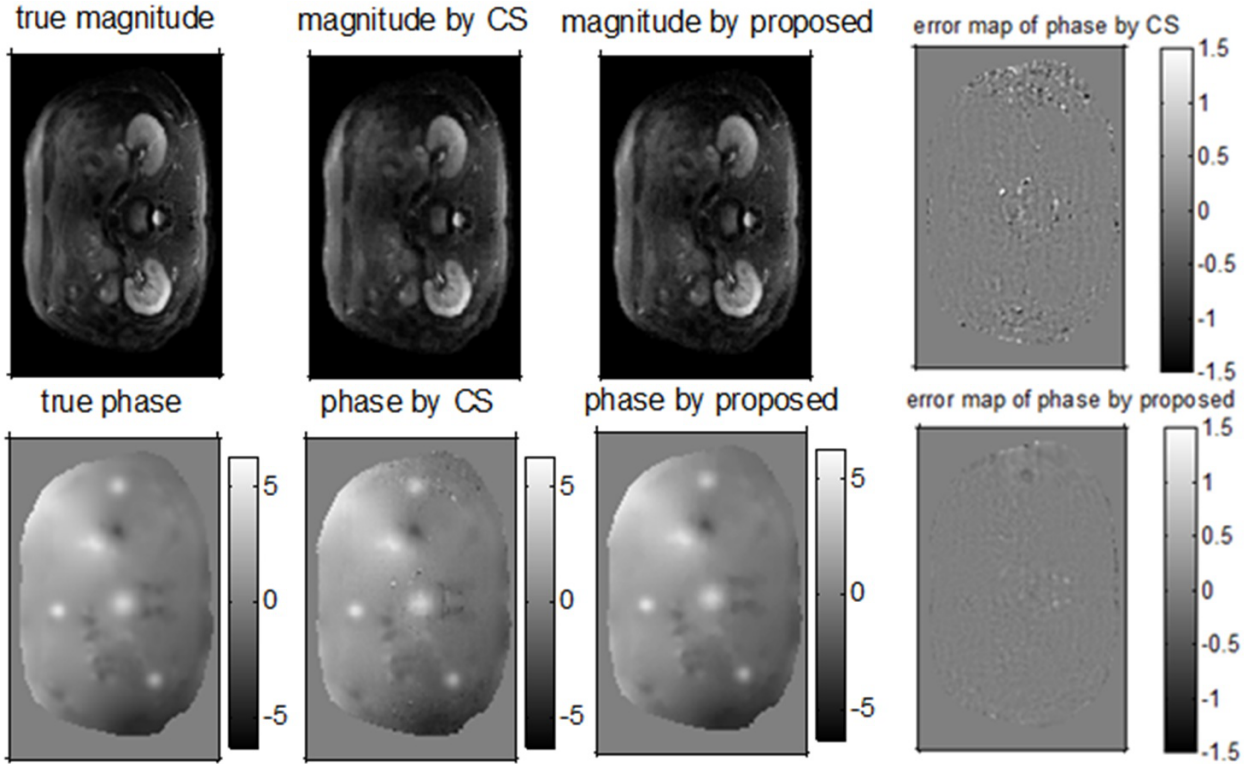
Figure 2.3.2: Top row: true magnitude, magnitude by CS, magnitude by the proposed method, phase error map by CS; bottom row: true phase, phase by CS, phase by the proposed method, phase error map by the proposed. (0.4 sampling rate, background is masked out, and the units of the phase are radians.)

Table 2.2: regularization parameters in the simulations

	0.2	0.3	0.4	0.5	0.6
β	1248	3744	2912	2912	4576
$\beta_1/10^6$	10	8	5	7	7
β_2	832	1248	1248	2080	2080

54

Table 2.3: regularization parameters in the simulations

	Reg. 1	Reg. 2	Reg. 3	Reg. 4
$\beta_1/10^4$	1	1	800	500
β_2	2912	2912	2912	1248
RMSE of ROI (radians)	0.930	0.087	0.282	0.081
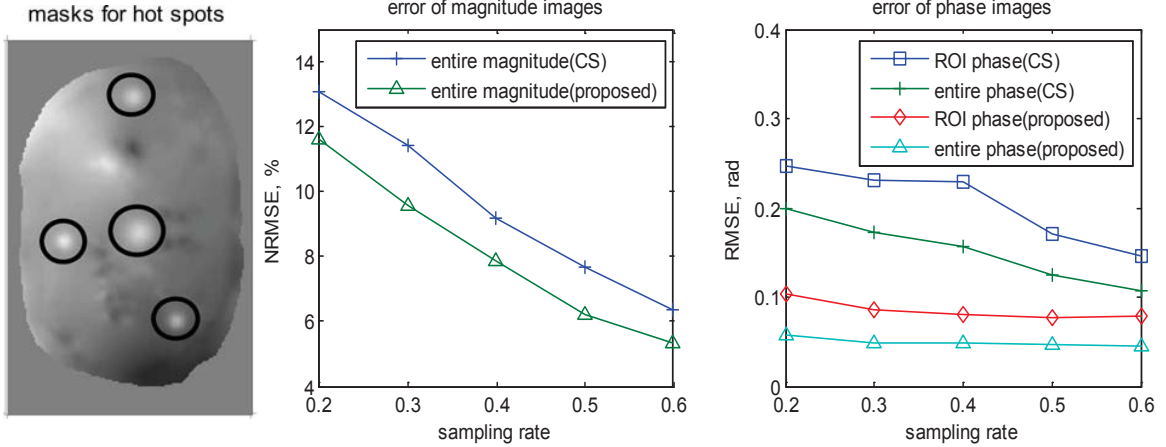
Figure 2.3.3: The regions masked for evaluating hot spots (left), NRMSE of the magnitude image (middle), RMSE of the entire phase image and RMSE of the phase masked for ROI, i.e., the hot spots, (right).

2.3.3 Experiments with In-vivo Data

We acquired *in-vivo* velocity mapping data around a human femoral artery using a phase-contrast bSSFP sequence in 3T GE scanner (Signa Excite HD) with an 8-channel cardiac surface coil array. These multi-coil Cartesian sampled data contain 10 temporal frames as well as the reference frame (no velocity encoding). In each frame, the Cartesian grid is $160 * 160$ which covers a FOV of 16 cm*16 cm. For demonstrating the 2D reconstruction algorithm for single coil, we used the reference frame and the 6th frame (capturing the peak velocity of the aorta) in coil 2 where the aorta signal is strong. Since the original data are fully sampled, we randomly undersampled them in the manner as in Fig. 2.3.1 to mimic the compressed sensing sampling; in particular, the sampling rate was chosen to be 1/3 of fully sampling, including 4% of fully sampled center.
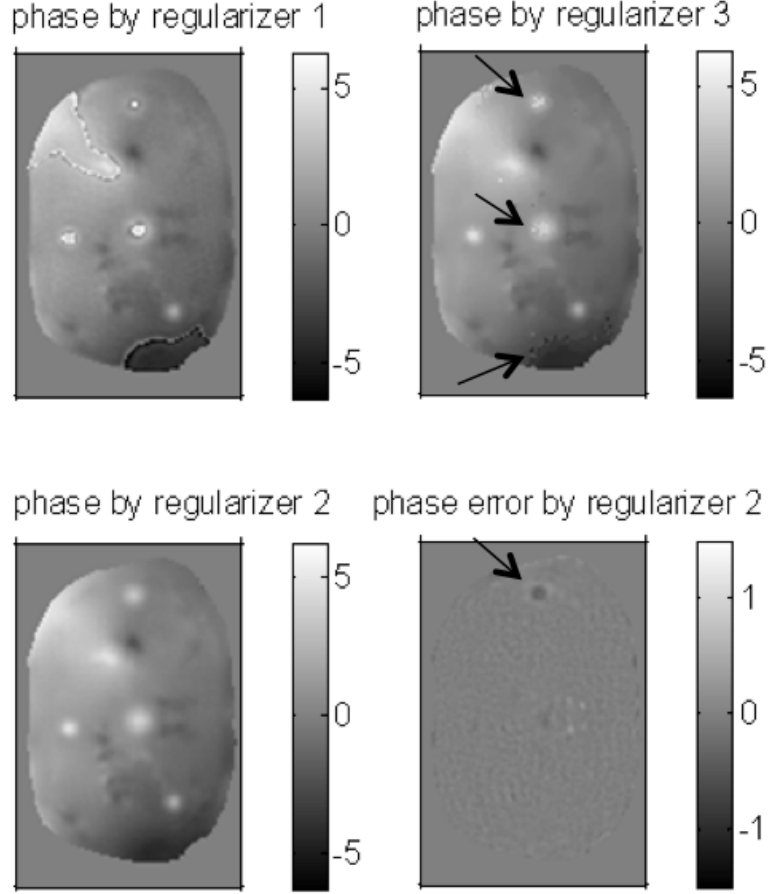
Figure 2.3.4: The reconstructed phase or phase error map by regularizer 1-3, the units are in radians

Due to the reference frame, the reconstruction procedure was slightly different from the simulation experiment. Instead of reconstructing from one set of 2D data, we first reconstructed the reference frame by each method, and then we reconstructed the velocity encoded image with background phase removed by incorporating the reconstructed reference frame into the system matrix, which is a similar strategy to phase correction in CS as shown in (2.2.7). The cost functions of the two methods for the second step are shown below:

$$\Psi_1(\boldsymbol{f}_1) = \|\boldsymbol{y} - A(e^{i\boldsymbol{P}}.* e^{i\boldsymbol{R_p}}.* \boldsymbol{f}_1)\|^2 + \beta R(\boldsymbol{f}_1) \tag{2.3.4}$$

56

$$\Psi_1(\boldsymbol{x}_1, \boldsymbol{m}) = \|\boldsymbol{y} - A(e^{i\boldsymbol{R_p}}. * \boldsymbol{m}. * e^{\boldsymbol{x}_1}\|^2 + \beta_1 R_x(\boldsymbol{x}_1) + \beta_2 R_m(\boldsymbol{m}) \qquad (2.3.5)$$

where (2.3.4) and (2.3.5) are for CS and the proposed method respectively, $\boldsymbol{R}_p$ is the reference phase which contains no velocity information, $\boldsymbol{f}_1$ should contain only velocity information in its phase, and $\boldsymbol{x}_1$ should contain only velocity information. In (2.3.4), the CS method also has low frequency phase correction. In the proposed method, we used regularizer 2 to reconstruct the reference image, a smooth phase map, as it has no velocity encoding; we used the regularizer 4 to reconstruct the velocity map. Furthermore, we also investigated the performance of the proposed method with regularizer 1-3. The potential function for regularizer 4 (regularizer 3) was the hyperbola function with $\delta = 0.005$ (radians). The regularization parameters for all the experiments are shown in Table 2.4.

Table 2.4: regularization parameters in the *in-vivo* experiments

	CS	Reg. 4	Reg. 1	Reg. 2	Reg. 3
$\beta_1/10^3$		60	5	5	50
β or β_2	800	800	800	800	800

The results are shown in Fig. 2.3.5. In this experiment, since there is no "true" image for comparison, the reconstruction results from the fully sampled data by inverse DFT are shown in the first row of Fig. 2.3.5 for comparison; the second and the third row are the results by CS and the proposed method respectively. In the figure, the first, second and third column are the magnitude images, the reference phase maps and the velocity maps respectively. Similar to the simulation experiment, both of the methods (CS and the proposed) can reconstruct a comparably good magnitude image from undersampled data. In the second column of Fig. 2.3.5, the reference phase map produced by the proposed method is much smoother than that by conventional CS. In the last column, the proposed method gives us a velocity map that clearly shows a
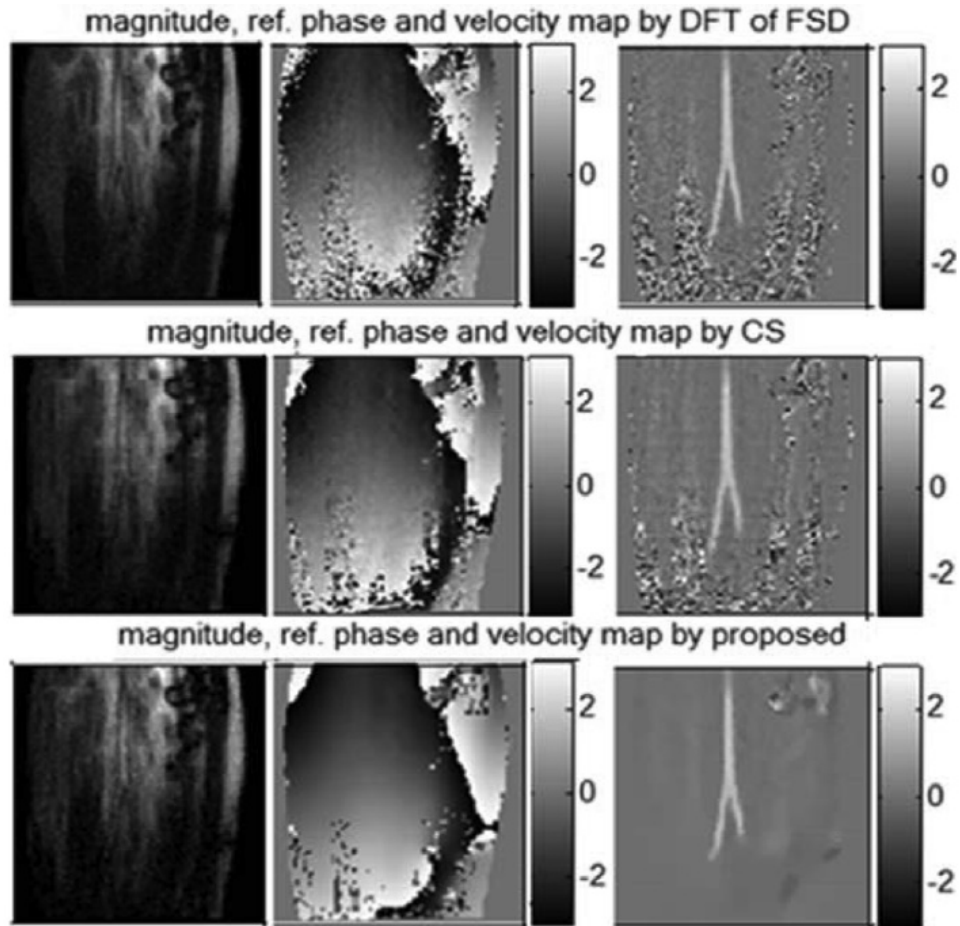
Figure 2.3.5: From the 1st row to the 3rd row: results by inverse DFT, conventional CS and the propose method; from the 1st column to the 3rd column: the magnitude, the reference phase and the velocity map. (The units of 2nd and 3rd columns are radians and cm/s respectively)

bifurcated aorta on top of a reasonably smooth background, which is much less noisy than the noisy velocity map produced by conventional CS.

In the right upper corner of the velocity map by the proposed method (Fig. 2.3.5), there is an area that is not smooth; this is due to the inconsistency between the reference frame and the velocity encoded frame, which appears to be caused by the unreliable reference phase in that low intensity area.

Fig. 2.3.6 shows the phase maps reconstructed by the proposed method with regularizer 1, 2 and 3. Similar to the results in the simulation studies, while regularizer
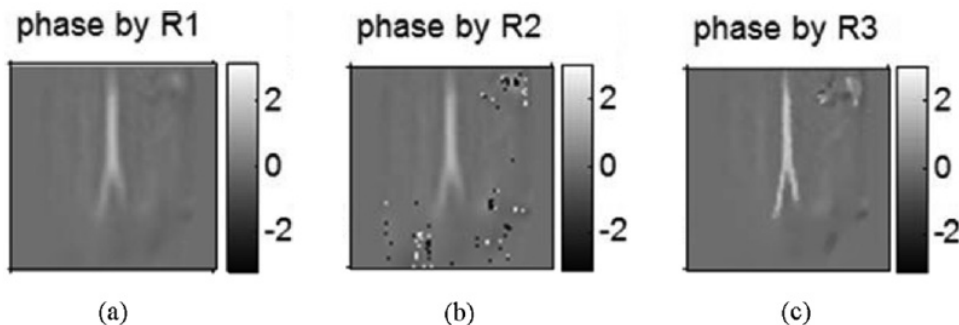
Figure 2.3.6: "R" denotes "regularizer"; left: phase map by the proposed method with R1; middle: phase map by the proposed method with R2; right: phase map by the proposed method with R3

2 smooths the background (except for the phase wraps), it also tends to over-smooth the arteries, which is undesirable. Since this particular problem has no phase wraps if initialized properly, the result by regularizer 1 just has some over-smoothed arteries and the one by regularizer 3 is as good as the one by regularizer 4 (shown in Fig. 2.3.5); both of them do not have phase wrapping problem. Then for this case, regularizer 3 provides better initialization than regularizer 2.

2.4 DISCUSSION

We have proposed two cost functions (2.2.13,2.2.15) and iterative algorithms (2.2.21-2.2.23) for reconstruction of magnitude and phase from undersampled k-space data. The key property of the proposed method is that one can adapt the regularizer for the magnitude and phase images individually.

The cost function is non-convex, so we cannot guarantee that the algorithm will converge to a global minimum. To mitigate this drawback, we introduced some suitable strategies for initialization. According to the simulation studies and real data experiments, it suffices to initialize by inverse DFT of zero-padded k-space and a few CS iterations for complex images when we apply regularizer 1, 2 or 3 appropriately. Since the cost function with regularizer 4 has a narrower convex domain, such two-

step initialization does not always work; so a third step is added to the initialization as mentioned in the theory section. The logic behind these sequential initialization strategies is: optimizing the cost function with a wider convex domain is likely to "push" the initial guess towards the relatively narrower convex domain of the cost function that is optimized in the following step, when these two cost functions have similar optimization solutions. For initialization of the cost function with regularizer 4, the first step by inverse DFT sets the initial guess in the convex domain of the non-concave conventional CS cost function, then optimizing CS cost function pushes the initial guess to the convex domain (around a desired local minimum) of the proposed cost function with regularizer 2 or 3, and finally optimization in the third step make the initial guess reach the convex domain (around a desired local minimum) of the proposed cost function with regularizer 4. In a word, the initial guess is gradually "pushed" towards the convex domain of the final cost function by such sequential initialization steps. However, these strategies cannot theoretically guarantee finding a desirable minimum and are only successful empirically. Refining the initialization for this type of non-convex cost function is still an open problem for future research.

When using regularizer 4, we choose among various edge-preserving potential functions. We have investigated all the potential functions listed in [62] that have a bounded $\dot{\omega}_\psi$ and most of them work well; finally we chose the hyperbola function because it has the widest convex domain and can match the quadratic function (t^2) very well when neighboring pixels have similar phase values. The parameter δ determines the transition between smoothing and edge-preserving, hence it should be selected according to the features of the specific true phase map. In our experiments, we empirically discovered that the peaks of the hot spots or arteries tend to be over-smoothed if δ is selected according to t_{edge}, i.e., the amount of jumps that happen in the "edge" regions. Alternatively, we chose δ to be much smaller than t_{edge}, in which case the regularizer 2 or 4 is approximately a Total Variation (TV) regularizer [63], as

the hyperbola potential function becomes approximately taking l_1 norm. Since TV still functions as edge-preserving regularization, it is still reasonable to use small δ for the proposed method. As long as δ is sufficiently small, we do not want it to be too small, because that will slower the convergence of the algorithm. Since the edges in the *in-vivo* data are sharper than the ones in the simulation data, δ in the *in-vivo* data was chosen to be larger than the one for the simulation data, but both of them are sufficiently smaller than t_{edge}. In a word, we empirically chose δ such that it is sufficiently small and also preserves an acceptable convergence rate.

The fully sampled k-space center is necessary for both conventional CS and the proposed method. For conventional CS, this part of the data is used to perform a rough phase-correction. In the proposed method, this low frequency part of the k-space contains most information of the phase map which has a smooth background. Empirically, $2 \sim 5\%$ of the k-space center is sufficient to preserve the low frequency information of phase maps.

As can be seen in the simulation results, magnitude maps produced by the proposed method merely have a $10 \sim 20\%$ lower NRMSE than the CS method in the simulation study and preserve a few more details if one carefully inspects, but this is not a significant improvement. Similar results were also observed in the *in-vivo* data experiments. In fact, this relatively small improvement is expected, because conventional phase-corrected CS has already removed most of the phase component of the true image before the CS reconstruction procedure. Therefore, the magnitude image in the proposed method is not significantly sparser than the phase corrected complex images in wavelet domain, which means the proposed method does not have much potential to significantly improve the magnitude image quality.

In the *in-vivo* experiment, although the phase map of conventional CS reconstruction looks closer to the fully sampled reconstruction, it does not indicate that it is closer to the true image; because the phase of the fully sampled reconstruction in

the low intensity regions is dominated by noise. According to the physics, the true phase map should be smooth except for the distinct regions, e.g., arteries, so we believe that the smoothed background of the phase maps reconstructed by the proposed method are closer to the true phase map. Similarly, the reference frame of the velocity mapping reconstructed by the proposed method with regularizer 2 should be more accurate than the noisy map estimated by conventional CS, which is one of the reasons why the velocity map reconstructed by the proposed method is better.

Our method can potentially be used for field map estimation. In [98], the method is based on the reconstructed image, but it is ultimately better to estimate phase changes based on the raw k-space data, because the image itself may suffer from some undesirable artifacts. Our method not only estimates the phase based on the k-space data, but also could accelerate the acquisition by undersampling, which is useful for 3D and/or high resolution field map estimation.

In this work, we only discussed the reconstruction problem for data from single coil acquisitions. However, all the proposed cost functions can also be easily generalized for parallel imaging, e.g. SENSE [60], to achieve an even lower sampling rate in k-space. Though we only studied 2D data, any higher dimensional data are applicable in the proposed method. The random sampling we used in the experiments simulates the random phase encode sampling in 3D data acquisition. Furthermore, this method is also applicable for non-Cartesian sampling by using non-uniform fast Fourier transform [24] as the system matrix.

The proposed method provides a more flexible and more controllable algorithm for phase map reconstruction than conventional phase corrected CS approach. The proposed method is flexible enough to allow customizing regularizers for phase component according to its own features, and regularizer 1-4 are concrete examples suitable for some applications; other sophisticated regularizers can be developed for other types of phase maps in this reconstruction framework. In addition, even though in

some cases the results of phase corrected CS are acceptable, it is not as flexible for tuning the smoothness or resolution of the phase map as the proposed method. If one wants to increase the resolution of a non-smooth phase map when using phase corrected CS, another scan with different sampling rate may be required; in contrast, within a certain range, the proposed method can handle this by simply adjusting regularization parameters in reconstruction for the same data.

2.5 CONCLUSIONS

By using the CS regularization terms for magnitude, the proposed method allows for undersampling in data acquisitions. In the framework of separate regularization reconstruction, the proposed method achieves a substantial improvement, e.g., $50\% - 70\%$, in phase reconstruction and a minor improvement, e.g., $10\% - 20\%$ in NRMSE, in magnitude reconstruction, compared to the phase corrected CS reconstruction. RMSE of ROI in phase maps were compared in the simulation studies to show that the proposed method can improve both ROI and background phase. Regularizer 1-4 were investigated for the simulated data and the in-vivo data, demonstrating that with initialization by using regularizer 2 or 3, the proposed method with regularizer 4 is able to handle phase wrapping and also reconstructs good phase maps and magnitude maps for applications like PRF-shift temperature mapping and phase contrast velocity mapping. The proposed method has more computational complexity, e.g., about ten times, than conventional CS, but we believe the computation speed can be made acceptable.

CHAPTER III

Regularized Estimation of Magnitude and Phase of Multi-Coil B_1 Field via Bloch-Siegert B_1 Mapping and Coil Combination Optimizations[1]

3.1 Introduction

For MRI with parallel excitation (PEX), it is critical to rapidly and accurately estimate the magnitude and relative phase of the multi-channel B_1 field, also known as B_1^+ mapping. Numerous methods have been proposed to map B_1 magnitude, such as double-angle method [45], actual flip angle imaging (AFI) [46] and Bloch-Siegert (BS) B_1 mapping [1]. PEX pulse design also needs the relative phase maps, i.e., the phase of one coil relative to that of all the other coils, which is typically mapped by successively exciting the same object with each coil and receiving the signal by one common coil or one common set of coils.

The approach described in this work is based on the BS B_1 mapping method, which applies off-resonance RF pulse in between the excitation pulse and the readout gradients [1]. This off-resonance pulse is called Bloch-Siegert (BS) pulse and it induces phase shifts that are proportional to $|B_1|^2$. This method is popular because it is fast and relatively accurate in a wide dynamic range and it is insensitive to T_1, chemical

---
[1]This chapter is based on [92, 93]

64

shift, B_0 field inhomogeneity and magnetization transfer effects [1]. Its speed and wide dynamic range are especially beneficial for PEX systems where B_1 mapping is generally more time-consuming and has wider ranges of B_1 magnitude than single channel systems. However, a disadvantage of this phase-based method is that the B_1 field estimation in low magnitude regions may suffer from low signal-to-noise ratio (SNR), due to insufficient excitation or low spin density. In particular, the problem of insufficient excitation is severe in PEX B_1 mapping because of the localized B_1 sensitivities of each coil. Furthermore, conventional estimation of B_1 phase needs another set of scans, which is time-consuming and information redundant.

BS B_1 mapping for PEX has been improved in [106] by using combinations of multiple coils for imaging excitation. However, regions of low spin density and/or insufficient excitation may still be problematic, and estimation of B_1 phase still needs another set of scans. Simply smoothing the noisy images with low-pass filters may propagate errors in the corrupted regions to neighboring regions. Therefore, we propose a modified BS B_1 mapping procedure that estimates both the magnitude and phase maps, saving one third of the scans; then a regularized estimation method is proposed to jointly estimate the magnitude and relative phase of multi-coil B_1 maps from this BS B_1 mapping data. By utilizing the prior knowledge that B_1 maps are smooth, the regularization terms can help improve quality of the B_1 map estimation in low magnitude regions.

Many B_1 mapping methods, e.g., [106] [107] [108], use linear combinations of PEX channels to narrow the dynamic range of effective B_1 field for better SNR, where typically all-but-one strategies are applied. However, these strategies are likely to be suboptimal in practice: the power levels of different channels in the object could be uneven due to non-isocenter positioning, which may cause nonuniform B_1 magnitude in the composite fields; the relative phase between channels could be far from what is assumed in those strategies, which may produce dark holes in the

composite fields. Malik *et al.* proposed a method to optimize coil combinations for PEX B_1 mapping [109], but it only optimized over a single complex parameter of the combination matrix over a limited range in an empirical way. That work evaluated the results according to two criteria: the dynamic range of the composite B_1 maps and the condition number of the combination matrix, which sometimes are hard to balance and also may not indicate the estimation quality. In this work, we propose to optimize linear coil combinations in [93] based on Cramer-Rao Lower Bound (CRLB) analysis [92]. The proposed method is general enough to optimize the combinations over all the elements of the combination matrix, which provides the most flexibility for optimization. Evaluation of the combinations is directly based on the variance of the complex B_1 field estimation instead of indirect factors like dynamic ranges and condition numbers. The algorithm minimizes the estimation variance of the pixel that has the maximal estimation variance, reducing the occurrence of focal noise amplification. Simulated Annealing (SA) method [110] is used for this highly nonlinear optimization problem.

This work is organized by starting with the signal model of images acquired by the proposed BS B_1 mapping sequence and then introducing the regularized estimation. Next, the detailed CRLB analysis is shown for this estimation method, and then we discuss optimizing the coil combination matrix. Finally, the proposed regularized estimation method and the proposed coil combination method are tested by simulations and phantom experiments on a 3T GE scanner equipped with an custom eight-channel parallel transmit and receive array [111] [112].

3.2 Regularized BS B_1 Estimation

3.2.1 Linear Combinations of Coils in B_1 Mapping

Instead of mapping one coil at a time, we estimate the multi-channel B_1 field by acquiring standard BS B_1 mapping data with multiple coils turned on at each time [106]. The composite complex B_1 field, $\tilde{C}_n(\boldsymbol{r})$, is the linear combination of the complex B_1 maps, $C_m(\boldsymbol{r})$, of the individual coils:

$$\tilde{C}_n(\boldsymbol{r}) = \sum_{m=1}^{N} \alpha_{n,m} C_m(\boldsymbol{r}) \tag{3.2.1}$$

where $n = 1, 2, \ldots, N$, N is the number of channels available, $\boldsymbol{r}$ denotes the spatial locations, and $\alpha_{n,m}$ is the user-defined complex scalar weighting for the mth individual coil in the nth scan. A convenient choice for $\alpha_{n,m}$ is the so-called all-but-one or leave-one-coil-out strategy, where $\alpha(n,n) = 0$
or -1 and $\alpha_{n,m} = 1$ when $m \neq n$ [107] [113]. Both the composite complex B_1 maps and the individual complex B_1 maps can be expressed in terms of their magnitudes and phases:

$$\tilde{C}_n(\boldsymbol{r}) = \tilde{B}_n(\boldsymbol{r}) e^{i\tilde{\phi}_n(\boldsymbol{r})}, C_m(\boldsymbol{r}) = B_m(\boldsymbol{r}) e^{i\phi_m(\boldsymbol{r})} \tag{3.2.2}$$

3.2.2 The Signal Model

The standard BS B_1 mapping works by applying the BS pulse after the regular excitation pulse [1]. This method typically needs 2 scans for each coil to measure B_1 magnitude, thus $2N$ scans are needed for an N-channel PEX system. To estimate both B_1 magnitude and relative phase by the standard BS B_1 mapping without additional scans for phase, we propose to use the same coil combinations for the BS pulse and the corresponding excitation pulse. The signal models for the noiseless BS data (reconstructed images) of the N pairs of scans, i.e., $\bar{S}_n^+(\boldsymbol{r})$ and $\bar{S}_n^-(\boldsymbol{r})$, are

described as follows:

$$
\begin{cases}
\bar{S}_n^+(\boldsymbol{r}) = \sin(\mu \tilde{B}_n(\boldsymbol{r})) e^{i\tilde{\phi}_n(\boldsymbol{r})} m_n^+(\boldsymbol{r}) e^{i\phi_b(\boldsymbol{r})} e^{iK_{BS}^+(\boldsymbol{r})\tilde{B}_n^2(\boldsymbol{r})} \\[2mm]
\bar{S}_n^-(\boldsymbol{r}) = \sin(\mu \tilde{B}_n(\boldsymbol{r})) e^{i\tilde{\phi}_n(\boldsymbol{r})} m_n^-(\boldsymbol{r}) e^{i\phi_b(\boldsymbol{r})} e^{iK_{BS}^-(\boldsymbol{r})\tilde{B}_n^2(\boldsymbol{r})}
\end{cases}
\tag{3.2.3}
$$

where $n = 1, 2, \ldots, N$; the superscripts $\pm$ denote the scan that has the BS pulse with $\pm\omega_{RF}$ off-resonance frequency, μ is the ratio between the actual flip angle and $\tilde{B}_n(\boldsymbol{r})$, $m_n^\pm(\boldsymbol{r})$ is the magnitude related to spin density, T_1, T_2, T_R, T_E, flip angle, receive sensitivity, magnetization transfer (MT) effect, etc., $\phi_b(\boldsymbol{r})$ is the corresponding background phase, and $K_{BS}^\pm(\boldsymbol{r})$ is the BS pulse constant that incorporates the B_0 field map [1]:

$$
K_{BS}^\pm(\boldsymbol{r}) = \frac{1}{2} \int_0^T \frac{(\gamma B_{\mathrm{normalized}}(t))^2}{\pm\omega_{RF}(t) - \omega_0(\boldsymbol{r})} dt
\tag{3.2.4}
$$

where $B_{\mathrm{normalized}}(t)$ is the normalized shape of the BS pulse. Due to the asymmetric MT effect [114], $m_n^+(\boldsymbol{r})$ is slightly different from $m_n^-(\boldsymbol{r})$. Moreover, we model additive independent and identically distributed (i.i.d.) complex Gaussian noise, i.e., $\epsilon_n^\pm(\boldsymbol{r})$, to the signal, and simplify (3.2.3) by changing variables:

$$
\begin{cases}
S_n^+(\boldsymbol{r}) = M_n^+(\boldsymbol{r}) e^{i[K_{BS}^+(\boldsymbol{r})\tilde{B}_n^2(\boldsymbol{r}) + \tilde{\phi}_n'(\boldsymbol{r})]} + \epsilon_n^+(\boldsymbol{r}) \\[2mm]
S_n^-(\boldsymbol{r}) = M_n^-(\boldsymbol{r}) e^{i[K_{BS}^-(\boldsymbol{r})\tilde{B}_n^2(\boldsymbol{r}) + \tilde{\phi}_n'(\boldsymbol{r})]} + \epsilon_n^-(\boldsymbol{r})
\end{cases}
\tag{3.2.5}
$$

where $S_n^\pm(\boldsymbol{r})$ are the noisy signals from the nth pair of scans, $M_n^\pm(\boldsymbol{r}) \triangleq \sin(\mu \tilde{B}_n(\boldsymbol{r})) m_n^\pm(\boldsymbol{r})$, and $\tilde{\phi}_n'(\boldsymbol{r}) \triangleq \tilde{\phi}_n(\boldsymbol{r}) + \phi_b(\boldsymbol{r})$. The simplest way to estimate B_1 magnitude and phase from this set of data is to first obtain $\tilde{B}_n(\boldsymbol{r})$ using the standard BS B_1 mapping reconstruction [1], and then, assuming $\tilde{B}_n(\boldsymbol{r})$ is known, the relative B_1 phase, $\tilde{\phi}_n'(\boldsymbol{r})$, can be derived by maximum likelihood estimator of (3.2.5) or simply taking:

$$
\tilde{\phi}_n'(\boldsymbol{r}) = \angle[S_n^+(\boldsymbol{r})/e^{iK_{BS}^+(\boldsymbol{r})\tilde{B}_n^2(\boldsymbol{r})}]
\tag{3.2.6}
$$

68

where $M_n^{\pm}(\boldsymbol{r})$ is not needed. We propose to set the coil combination of each excitation pulse the same as its corresponding BS pulse, so that $\tilde{B}_n(\boldsymbol{r})$ and $\tilde{\phi}'_n(\boldsymbol{r})$ correspond to the same composite B_1 map, hence the individual B_1 magnitude and phase, i.e., $B_n(\boldsymbol{r})$ and $\phi'_n(\boldsymbol{r})$, can be derived by (3.2.9) below. This is how the modified BS sequence can avoid the additional scans for B_1 phase. Moreover, for regularized estimation, $M_n^{\pm}(\boldsymbol{r})$ is a set of nuisance parameters that we must jointly estimate, but they are fortunately linear terms that can be easily estimated.

3.2.3 Regularized Estimation of B_1 Magnitude and Phase

Regularization enforces prior knowledge to improve estimation. It is reasonable to assume that the magnitude of the composite B_1 maps, $\tilde{B}_n(\boldsymbol{r})$, are spatially smooth. Although the absolute phase $\tilde{\phi}_n(\boldsymbol{r})$ is not necessarily smooth, the relative phase maps, e.g., $\tilde{\phi}_n(\boldsymbol{r}) - \tilde{\phi}_1(\boldsymbol{r})$, should be smooth. To prevent problems with phase wrapping in $\tilde{\phi}_n(\boldsymbol{r}) - \tilde{\phi}_1(\boldsymbol{r})$, we propose to use the regularizer proposed in [68] that regularizes the roughness of $e^{i[\tilde{\phi}_n(\boldsymbol{r}) - \tilde{\phi}_1(\boldsymbol{r})]}$. The final regularized maximum-likelihood cost function for the estimation is shown in (3.2.7), where all the spatially varying maps are discretized into column vectors (shown in bold fonts):

$$
\begin{aligned}
\Psi(\tilde{\boldsymbol{B}}, \tilde{\boldsymbol{\phi}}, \boldsymbol{M}) = \sum_{n=1}^{N} \sum_{\varsigma=+,-} & \| \boldsymbol{S}_n^{\varsigma} - \boldsymbol{M}_n^{\varsigma}. * e^{i(\boldsymbol{K}_{BS}^{\varsigma}.*\tilde{\boldsymbol{B}}_n^2 + \tilde{\boldsymbol{\phi}}'_n)} \|^2 \\
& + \beta_1 \sum_{n=1}^{N} \| C\tilde{\boldsymbol{B}}_n \|^2 + \beta_2 \sum_{n=2}^{N} \| Ce^{i(\tilde{\boldsymbol{\phi}}'_n - \tilde{\boldsymbol{\phi}}'_1)} \|^2
\end{aligned}
\tag{3.2.7}
$$

where β_1 and β_2 are scalar regularization parameters, $\boldsymbol{M}$ is the concatenation of the image magnitudes $\boldsymbol{M}_n^{\pm}$ of all channels, $\tilde{\boldsymbol{B}}$ and $\tilde{\boldsymbol{\phi}}$ denote the concatenation of all the composite B_1 magnitudes $\tilde{\boldsymbol{B}}_n$ and all the composite B_1 phases $\tilde{\boldsymbol{\phi}}'_n$ respectively, ".*" represents element-by-element multiplication between vectors, $\tilde{\boldsymbol{B}}_n^2$ denotes the vector that contains the squares of the corresponding elements of $\tilde{\boldsymbol{B}}_n$, and C is a finite differencing matrix used to penalize roughness.

We iteratively minimize the cost function (3.2.7) by cyclically updating $\tilde{\boldsymbol{B}}$, $\tilde{\boldsymbol{\phi}}$ and $\boldsymbol{M}$:

$$(\hat{\tilde{\boldsymbol{B}}}, \hat{\tilde{\boldsymbol{\phi}}}, \hat{\boldsymbol{M}}) = \underset{\tilde{\boldsymbol{B}},\tilde{\boldsymbol{\phi}}\in\mathbb{R}^{(NN_p)\times 1}, \boldsymbol{M}\in\mathbb{R}^{(2NN_p)\times 1}}{\operatorname{argmin}} \Psi(\tilde{\boldsymbol{B}}, \tilde{\boldsymbol{\phi}}, \boldsymbol{M}) \qquad (3.2.8)$$

where $\hat{\tilde{\boldsymbol{B}}}, \hat{\tilde{\boldsymbol{\phi}}}$ and $\hat{\boldsymbol{M}}$ denote the estimates of $\tilde{\boldsymbol{B}}, \tilde{\boldsymbol{\phi}}, \boldsymbol{M}$ respectively, and N_p is the number of pixels of each channel. We update $\boldsymbol{M}$ by simply taking the real least square solution of (3.2.7) in each iteration. The cost function is non-quadratic in $\tilde{\boldsymbol{B}}$ and $\tilde{\boldsymbol{\phi}}$, so we use conjugate gradients with line search algorithms (CG-LS) [115] to update $\tilde{\boldsymbol{B}}$ and $\tilde{\boldsymbol{\phi}}$, where backtracking line search (BLS) [116] and monotonic line search (MLS) [115] are used for $\tilde{\boldsymbol{B}}$ and $\tilde{\boldsymbol{\phi}}$ respectively to guarantee monotonicity (see Appendix for details). The standard approach [1] produces a good initial guess for $\tilde{\boldsymbol{B}}$, and then we compute the initial guess of $\tilde{\boldsymbol{\phi}}$ using (3.2.6). Once $\tilde{\boldsymbol{B}}$ and $\tilde{\boldsymbol{\phi}}$ are estimated, magnitude and relative phase maps of the original coils, $\boldsymbol{B}$ and $\boldsymbol{\phi}$, can be derived easily using the following relation:

$$\begin{bmatrix} B_1(\boldsymbol{r})e^{i\phi_1'(\boldsymbol{r})} \\ \vdots \\ B_N(\boldsymbol{r})e^{i\phi_N'(\boldsymbol{r})} \end{bmatrix} = A^{-1} \begin{bmatrix} \tilde{B}_1(\boldsymbol{r})e^{i\tilde{\phi}_1'(\boldsymbol{r})} \\ \vdots \\ \tilde{B}_N(\boldsymbol{r})e^{i\tilde{\phi}_N'(\boldsymbol{r})} \end{bmatrix} \qquad (3.2.9)$$

where $\phi_n'(\boldsymbol{r}) \triangleq \phi_n(\boldsymbol{r}) + \phi_b(\boldsymbol{r})$, which does not change the relative phase maps, and A is the coil combination matrix:

$$A \triangleq \begin{bmatrix} \alpha_{1,1} & \cdots & \alpha_{1,N} \\ \vdots & \ddots & \vdots \\ \alpha_{N,1} & \cdots & \alpha_{N,N} \end{bmatrix} \qquad (3.2.10)$$

3.3 Coil Combination Optimization

3.3.1 Approximate Signal Model

As mentioned before, the coil combination matrix A in (3.2.10) is conventionally chosen by an all-but-one strategy, but this approach is unlikely to be optimal in practice. Therefore, we propose a method to optimize over the matrix A to improve the estimates of the magnitude and phase of B_1 field in PEX. We use the CRLB to derive a lower bound on the variance of the complex B_1 field estimates in terms of the coil combination matrix A and then find the A that minimizes the worst-case noise-to-signal ratio (NSR).

To simplify the noise analysis, we make some approximations for (3.2.5): asymmetric MT effect is ignored so that $M_n^+(\boldsymbol{r}) \approx M_n^-(\boldsymbol{r}) \triangleq M_n(\boldsymbol{r})$, and the off-resonance effects in $K_{BS}^\pm(\boldsymbol{r})$ are ignored so that $K_{BS}^+(\boldsymbol{r}) \approx -K_{BS}^-(\boldsymbol{r}) \triangleq K$ which is a scalar constant. If we assume the real and imaginary parts of the i.i.d. Gaussian noise are uncorrelated and distributed as $\mathcal{N}(0, \sigma^2)$ where σ^2 is the variance, then the approximate distributions of the signals for each pixel are expressed as follows:

$$
\begin{cases}
S_r^+ \sim \mathcal{N}(M\cos(KB^2 + \phi), \sigma^2) \\[2mm]
S_i^+ \sim \mathcal{N}(M\sin(KB^2 + \phi), \sigma^2) \\[2mm]
S_r^- \sim \mathcal{N}(M\cos(-KB^2 + \phi), \sigma^2) \\[2mm]
S_i^- \sim \mathcal{N}(M\sin(-KB^2 + \phi), \sigma^2)
\end{cases}
\tag{3.3.1}
$$

where the subscripts n, indices $\boldsymbol{r}$, primes and tildes in (3.2.5) are omitted for simplicity, subscripts r/i denote the real/imaginary parts.

3.3.2 Cramer-Rao Lower Bound Analysis

The CRLB is a lower bound on the covariance of any unbiased estimator under certain regularity conditions. The CRLB can be achieved by unbiased maximum likelihood estimators (MLE). This work tries to improve the quality of the raw data before applying regularized estimation, so the effective estimators are equivalent to the estimators in (3.2.8) with $\beta_1 = \beta_2 = 0$ which yields the MLE.

Equation (3.3.1) can be vectorized as follows:

$$\boldsymbol{y} = \boldsymbol{\mu}(\boldsymbol{\theta}) + \boldsymbol{\epsilon} \quad \text{where} \quad \boldsymbol{\epsilon} \sim \mathcal{N}(\boldsymbol{0}, \sigma^2 \boldsymbol{I}) \tag{3.3.2}$$

where $\boldsymbol{y} = [S_r^+, S_i^+, S_r^-, S_i^-]^T$, $\boldsymbol{\mu} = [M\cos(KB^2 + \phi), M\sin(KB^2 + \phi), M\cos(-KB^2 + \phi), M\sin(-KB^2 + \phi)]^T$, $\boldsymbol{\theta} = [B, \phi]^T$. We show in the Appendix that this problem satisfies the regularity condition for the CRLB theorem. Then, with Taylor expansion and assuming the scans have independent noise, we derived the lower bound of the variances of the complex B_1 estimates of the N channels in location $\boldsymbol{r}$:

$$\mathsf{var}(\hat{C}_{n,\boldsymbol{r}}(A)) \triangleq \mathsf{var}(\hat{B}_{n,\boldsymbol{r}}(A) e^{i\hat{\phi}'_{n,r}(A)}) \geqslant V_{n,\boldsymbol{r}}(A)$$

with $V_{n,\boldsymbol{r}}(A)$

$$\triangleq \{A^{-1}\mathsf{diag}\{\frac{\sigma^2}{2M_{n,\boldsymbol{r}}^2(A)}[\tilde{B}_{n,\boldsymbol{r}}^2(A) + \frac{1}{4K^2\tilde{B}_{n,\boldsymbol{r}}^2(A)}]\}A^{-H}\}_{n,n} \tag{3.3.3}$$

where $n = 1, \ldots, N$, $\mathsf{diag}\{z\}$ denotes the diagonal matrix with vector z its diagonal entries, and we have put back the subscripts n, indices $\boldsymbol{r}$, primes and tildes in (3.2.5) except that we move the indices $\boldsymbol{r}$ to the subscripts and make A be the argument, as A is the main unknown of this optimization problem. The detailed derivation is shown in the Appendix.

3.3.3 Optimize Linear Combinations of Array Elements

We propose to optimize the SNR of the B_1 estimates by minimizing the lower bound of NSR, defined as the ratio between $\sqrt{V_{n,\boldsymbol{r}}(A)}$ and $B_n(\boldsymbol{r})$. Since (3.3.3) is only for one single pixel, a scalar that evaluates the noise performance of the whole 2D or 3D B_1 field of the N coils has to be chosen for optimizing over the coil combinations. To better suppress the focal noise amplifications which are common in PEX B_1 mapping, we apply a min-max optimization strategy in this work, where the maximal $V_{n,\boldsymbol{r}}(A)$ of all spatial locations and channels is minimized to optimize the worst noise performance of the whole estimation. A practical issue is that PEX systems have amplitude limits, which bounds the maximum magnitude of the elements of A, so A must be constrained according to the hardware limits. Therefore, the final expression of this optimization problem is shown as follows:

$$\hat{A} = \underset{A \in \mathbb{C}^{N \times N}}{\operatorname{argmin}} \{ \max_{n,\boldsymbol{r}} \frac{\sqrt{V_{n,\boldsymbol{r}}(A)}}{B_{n,\boldsymbol{r}}(A)} \} \tag{3.3.4}$$

subject to

$$\max_{m,n} |\alpha_{m,n}| \leqslant \lambda$$

where λ is the amplitude limit of the PEX system. This method optimizes the noise performance over all the elements of A, which is much more flexible than the method in [109].

The cost function in (3.3.4) is highly nonlinear and nonconvex in terms of A, so it would be very hard to find the global minimum. In practice, however, it should suffice to keep the noise level below a certain reasonable value rather than to exhaustively search for the global minimizer. Since A is relatively a small matrix, we found that the Simulated Annealing (SA) method [110] in Matlab's Optimization Toolbox can efficiently find a reasonably good local minimum.

The CRLB expression (3.3.3) depends not only on the coil combination matrix

A that we will optimize using (11), but also on other parameter maps that are not known, namely $M_{n,\boldsymbol{r}}(A)$ and $\tilde{B}_{n,\boldsymbol{r}}(A)$. The composite maps $\tilde{B}_{n,\boldsymbol{r}}(A)$ can be described as:

$$\tilde{B}_{n,\boldsymbol{r}}(A) = \left| \sum_{m=1}^{N} \alpha_{n,m} B_m(\boldsymbol{r}) e^{i\phi_m(\boldsymbol{r})} \right| \tag{3.3.5}$$

The maps $M_{n,\boldsymbol{r}}(A)$ depend on other parameters that are unknown, such as T_1, T_2 and spin density, and can be modeled mathematically according to the specific imaging sequence. In this work, we only focus on the spoiled gradient echo (SPGR) based BS sequence, where $M_{n,\boldsymbol{r}}(A)$ can expressed as follows:

$$M_{n,\boldsymbol{r}}(A) = B_1^-(\boldsymbol{r}) e^{-\frac{T_E}{T_2(\boldsymbol{r})}} \frac{\rho(\boldsymbol{r})(1 - e^{-\frac{T_R}{T_1(\boldsymbol{r})}}) \sin(\mu \tilde{B}_{n,\boldsymbol{r}}(A))}{1 - e^{-\frac{T_R}{T_1(\boldsymbol{r})}} \cos(\mu \tilde{B}_{n,\boldsymbol{r}}(A))} \tag{3.3.6}$$

where $B_1^-(\boldsymbol{r})$ is the receive coil sensitivity map, $\rho(\boldsymbol{r})$ is the spin density map, $T_1(\boldsymbol{r})$ and $T_2(\boldsymbol{r})$ are the T_1 and T_2 maps respectively. Instead of attempting to determine these maps, which would be impractical, we use uniform maps with nominal T_1, T_2, and ρ values for optimizing A. For $B_1^-(\boldsymbol{r})$, we either use uniform values when signal is received by a single coil in a non-high field scanner ($\leqslant$3T), or acquire an off-line phantom data for a coarse estimation of $B_1^-(\boldsymbol{r})$. For the transmit B_1 magnitude, $B_m(\boldsymbol{r})$, we use a set of B_1 maps estimated by a phantom off-line. For the transmit B_1 phase, $\phi_m(\boldsymbol{r})$, we either use off-line phantom estimates or fast on-line low resolution *in-vivo* B_1 phase maps.

For our experiments, we focus on an eight-channel PEX head array that has 8-fold rotational symmetry, so although the proposed method can optimize over all the elements of A, it is natural to restrict the 8×8 matrix A to be circulant, which saves computation time by reducing the number of unknowns to 8. This approach also seems to be more robust to local minima compared to optimizing all elements of A.

74

3.4 Experiments

3.4.1 Phantom Experiment: Regularized B_1 Estimation

We carried out a phantom experiment to demonstrate the proposed regularized BS B_1 map estimation on a 3T GE scanner (GE Healthcare, Milwaukee, WI, USA) equipped with an 8-channel custom parallel transmit/receive system. We used a spherical phantom filled with distilled water. Due to a failure in one RF amplifier, since fixed, only seven of the transmit channels were used, the eighth has zero input throughout the experiment. All the data were acquired with a SPGR sequence having a 2D spin-warp readout. We applied a 20 ms Fermi BS pulse with ± 4 kHz off-resonance frequencies. Other imaging parameters were: $T_E = 23$ ms, $T_R = 200$ ms, FOV $= 24 \times 24$ cm, 64×64 reconstruction matrix size, and axial slice imaging. Note that the raw data were all 8-channel parallel imaging data, and they were combined together using the receive side B_1 shimming according to the receive sensitivity maps acquired off-line.

We first acquired B_0 map (ranges from -80 to 8 Hz) using two 2D SPGR scans with an echo time difference. A total of 14 proposed BS B_1 mapping scans were done for this 7-channel B_1 estimation, where we applied the all-but-one coil combination with $\alpha_{1,1} = 0, \alpha_{1,2} = \ldots = \alpha_{1,N} = 1$. The reconstructed raw images were then put into the standard non-regularized BS estimator and the proposed regularized BS estimator. For the proposed method, we manually selected the regularization parameters to be $\beta_1 = 40$ and $\beta_2 = 0.1$; the number of outer iterations was set to 40 with 3 sub-iterations for $\tilde{\boldsymbol{B}}$ and $\tilde{\boldsymbol{\phi}}$ in each outer iteration; the whole reconstruction took less than a minute on a computer with Intel Core2 Quad CPU Q9400 @ 2.66 GHz, 4 GB RAM and Matlab 7.8. Fig. 3.4.1 shows the estimated B_1 magnitude and phase maps, where the proposed regularized estimation improves the quality of both the magnitude and phase maps. If we use the standard method with 1/3 more scans, the

B_1 estimation results will be the same except for the SNR of the B_1 phase. If high SNR imaging is used for the B_1 phase mapping, the results may have better SNR than the results shown in Fig. 3.4.1, but this requires 1/3 more scans. Furthermore, there are still several rough spots in the magnitude maps that were corrupted by the low signal intensity regions so much that they were not fully smoothed by the regularized algorithm. This is the main motivation for us to propose the coil combination optimization which improves the raw data before any reconstruction, and it is discussed and shown to be effective in avoiding such problems in the following sections.

3.4.2   Simulation Study: Coil Combination Optimization

A finite-difference time-domain (FDTD) simulation generated 2D magnetic fields of an eight-channel parallel excitation array for brain imaging at 3T, which is used as the true B_1 maps in the simulations (shown in Fig. 3.4.2). We used a set of brain tissue parameter maps, e.g., T_1 map, T_2 map and spin densities, from "BrainWeb database" [117] [118] [119] [120] [121] as the true values for generating images produced by the BS sequence. The image magnitude was generated based on the signal equation of SPGR sequence (3.3.5) with image parameters: $T_R = 200$ ms, $T_E = 10$ ms. The BS induced phase was simulated based on ± 4 kHz off-resonance Fermi BS pulses ($K_{BS} = 76.9 \, \text{rad/G}^2$) and a realistic B_0 field map acquired from a brain on a 3T GE scanner (ranging from -86 Hz to 25 Hz). Furthermore, the B_1^- map was acquired from a real single-channel body receive coil of the 3T GE scanner. By adding i.i.d. complex Gaussian noise to the noiseless images generated based on (3.2.3), (3.3.5) and (3.3.6), we simulated the raw data in image domain acquired by SPGR-based BS B_1 mapping sequence. The matrix size of these 2D images is 64×64. Note that the coil combination matrix A has to be optimized before simulating the raw data. In the
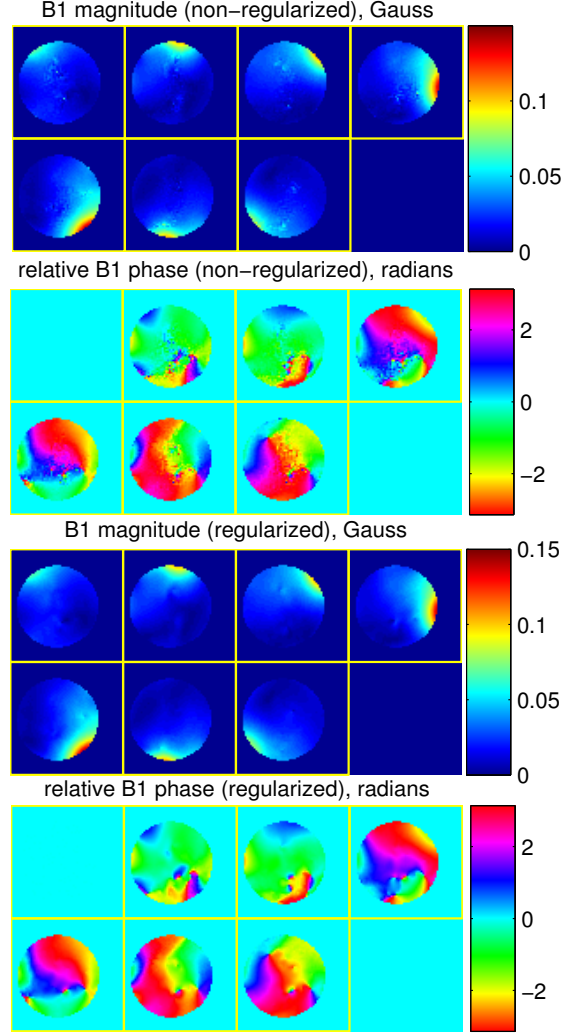
Figure 3.4.1: The estimated B_1 magnitude and phase maps by the non-regularized method and the regularized method.

data simulation, the standard deviation of the Gaussian noise stayed the same and the SNR of raw image data ranged from 23 dB to 26 dB depending on the specific coil combinations; the SNR is defined in image domain as:

$$\text{SNR} = 20 \log_{10}\left(\frac{\|\boldsymbol{S}_t\|}{\|\boldsymbol{S}_t - \boldsymbol{S}\|}\right) \tag{3.4.1}$$

where $\boldsymbol{S}_t$ and $\boldsymbol{S}$ denote the noise-free and noisy images respectively.

We used approximated parameters for the optimization step. T_2 and spin density
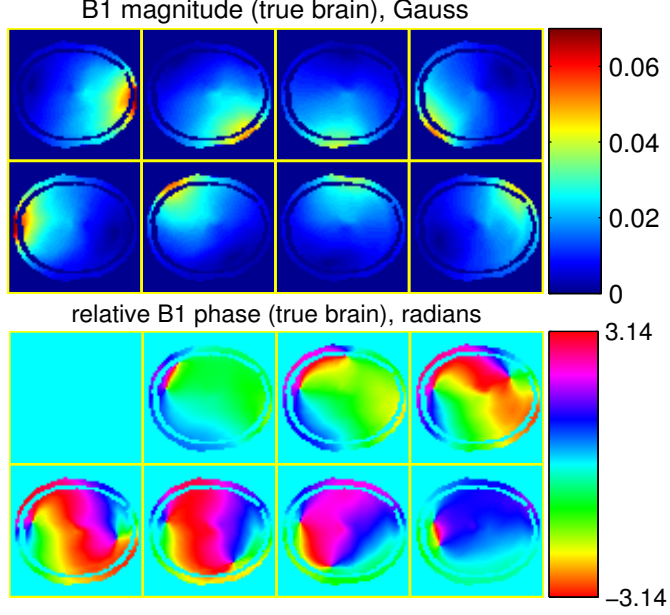
Figure 3.4.2: B_1 maps of the brain, used as the ground truth.

were uniform maps with nominal values, as the absolute values of them are not relevant to the optimization of (3.3.4); T_1 maps were set to be the maximal value (2.6 s) of brain tissue. Since the true receive coil sensitivity map, which was acquired from a single-channel at 3T, is relatively uniform, we used a uniform B_1^- map for the optimization. Furthermore, we did another FDTD simulation for a uniform phantom with the same configurations and positions of the coils as the simulation for the brain; the relative permittivity was 42.3 and conductivity was .489 S/m, which represent the average values of brain tissue; the space occupied by the phantom needed to cover the brain used in the previous simulation, so that the phantom B_1 maps can be cropped to the brain size for the optimization (shown in Fig. 3.4.3). For the B_1 phase specifically, other than using the phantom B_1 phase which will be called "method 1", we also simulated an on-line low resolution (32×32 matrix) fast scan of brain using one transmit coil at a time to obtain the relative B_1 phase, which will be called "method 2". Moreover, for demonstration purposes, we simulated the case when the coil combinations are optimized based on the true B_1 maps as well as true B_1-, T_1,
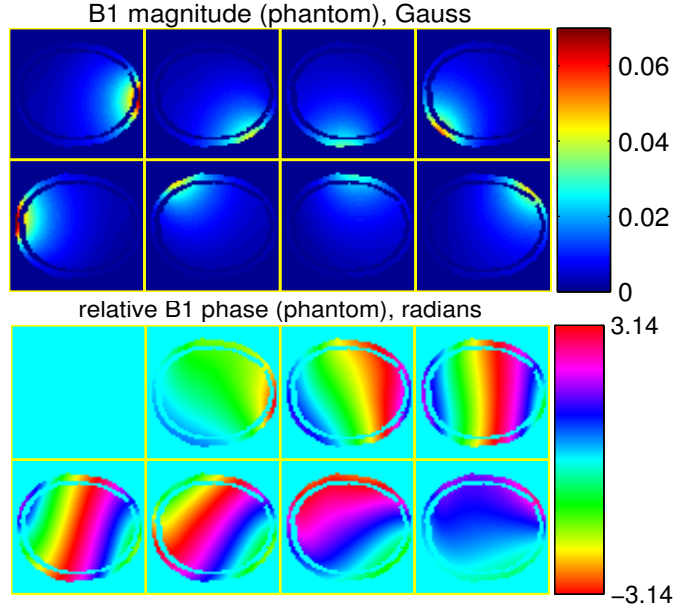
Figure 3.4.3: B_1 maps of the phantom (masked by the brain shape), used for optimization.

T_2 and spin density maps, which will be called "oracle method". For comparison, the results of the all-but-one combination with $\alpha_{1,1} = 0, \alpha_{1,2} = \ldots = \alpha_{1,N} = 1$ were also simulated. Table 3.1 summarizes the methods used in this simulation study. Circulant structure was assumed for the matrix A, and the optimization algorithm was initialized with the all-but-one combination. The threshold λ in (3.3.4) was set such that the RF power does not exceed a fixed peak nominal power. Furthermore, a fast online low resolution prescan of the subject has to be done anyway to obtain a mask for the optimization. Note that a more accurate mask was applied to all the images and the statistics (Table 3.2) in the result.

Table 3.1: Summary of the Methods in the Simulation

	B_1 mag. estimates	B_1 phase estimates	B_1-, T_1, T_2, spin density
method 1	Phantom (off-line)	Phantom (off-line)	Uniform maps
method 2	Phantom (off-line)	Low-res *in-vivo* (online)	Uniform maps
oracle method	True B_1 magnitude	True B_1 phase	True maps
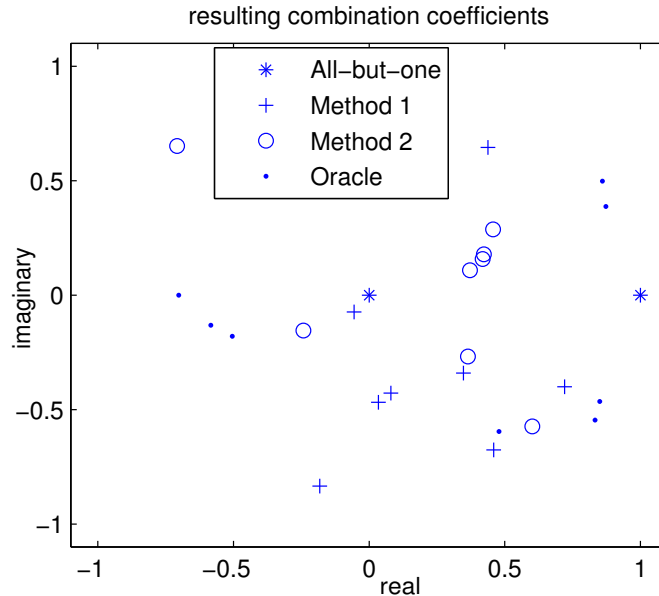
Figure 3.4.4: The first row of the resulting combination matrices by different methods, where the magnitude is normalized to the peak nominal power of the system.

Fig. 3.4.4 shows the resulting coil combination coefficients by different methods. As we assumed circulant structure, only the first rows of each A, which are vectors of 8 complex numbers, are shown in the complex plane. Compared to the all-but-one method, all the other optimized results are scattered more uniformly within the complex plane and also "random-like". We also calculated the condition numbers of all the combination matrices and obtained the corresponding composite B_1 maps, which are shown in Fig. 3.4.5. As can be seen, the oracle method and method 2 produced more uniform composite B_1 maps and have much smaller condition numbers, compared to method 1 and the all-but-one method. The composite maps of method 1 are as uniform as those of the all-but-one method, but its condition number is largely reduced. In addition, the all-but-one method produced higher overall B_1 magnitude than the optimized combinations.

Furthermore, if the true tissue parameters and the true B_1 maps along with the

resulting matrix A are plugged into (3.3.3-3.3.6), we can get the lower bounds maps of NSR, i.e., $\frac{\sqrt{V_{n,r}(A)}}{B_n(\boldsymbol{r})}$, and the results of different methods are shown in Fig. 3.4.6. Method 2 and oracle method greatly reduced the focal noisy spots and produced relatively uniform NSR maps. However, method 1 did not work as well as method 2 due to the large model mismatch in B_1 phase, but it still lowered the noise amplification and redistributed the focal noisy spots, compared to the all-but-one method.
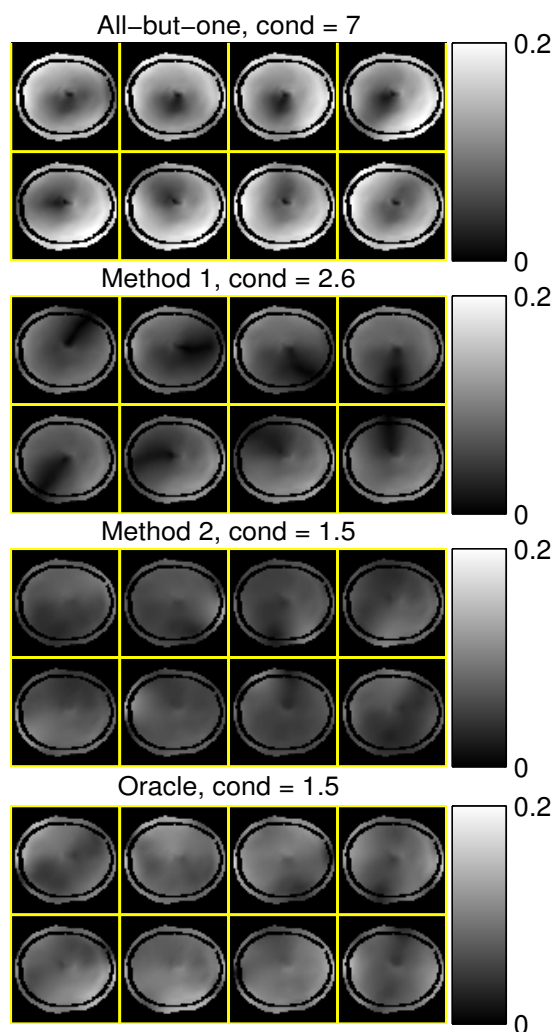
Figure 3.4.5: Magnitude of the composite B_1 maps (masked), $\tilde{B}_n(\boldsymbol{r})$, by different methods, in Gauss. The condition numbers (cond) of each combination matrix are shown on the titles.
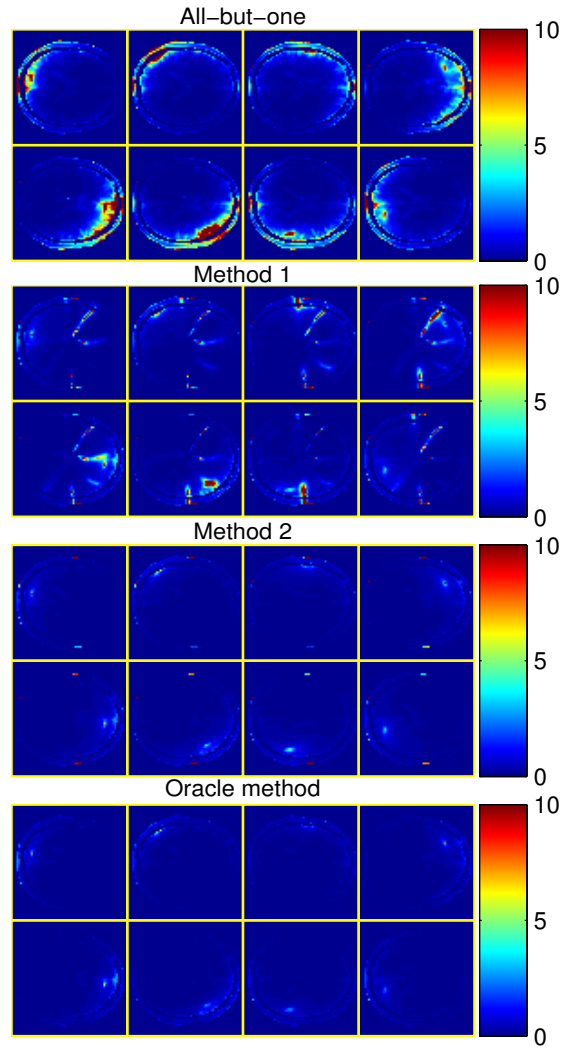
Figure 3.4.6: The lower bounds of NSR maps (masked) by different methods, unitless.

Finally, we simulated the B_1 map reconstruction with the four different coil combinations, where we used the non-regularized method to reconstruct the B_1 magnitude and phase. Fig. 3.4.7 shows the resulting B_1 magnitude and phase maps. As can be predicted from Fig. 3.4.5 and Fig. 3.4.6, method 2 and the oracle method pro-
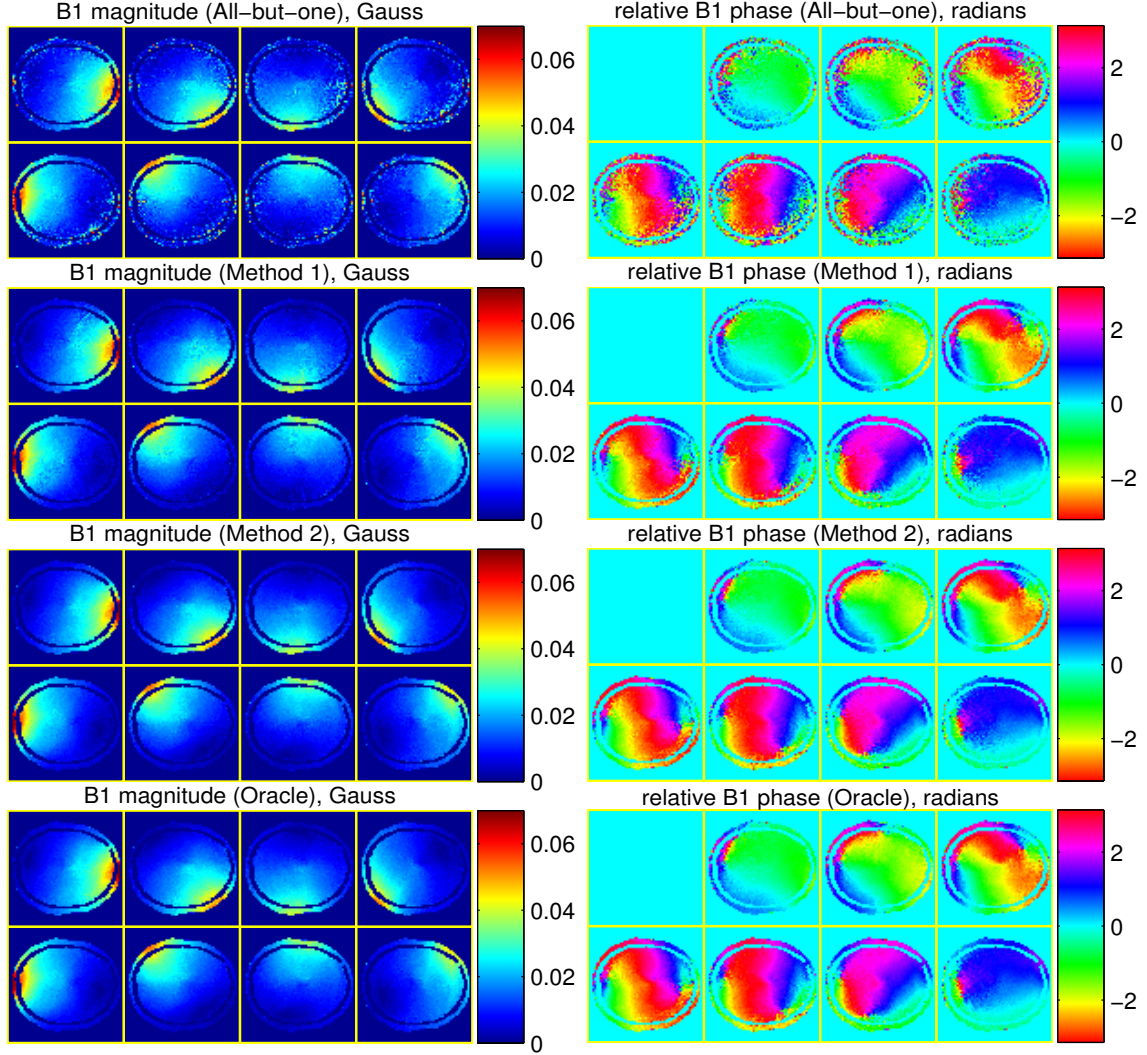
Figure 3.4.7: The simulation results of all the methods; left: B_1 magnitude estimates, right: B_1 phase estimates.

duced less noisy B_1 maps than method 1 and the all-but-one method. Despite the model mismatch mainly in B_1 magnitude, receive sensitivities and distributions of spin density, T_1 and T_2, method 2 still worked similarly well as the oracle method. In contrast, although method 1 still largely improved the B_1 estimation compared to the all-but-one method, the results of method 1 are not at the same level as those of method 2 and the oracle method. Table 3.2 shows the normalized root mean squared error (NRMSE) of the B_1 magnitude and the root mean squared error (RMSE) of

the B_1 phase, which are defined as:

$$\text{NRMSE} \triangleq \frac{\|\boldsymbol{B}_r - \boldsymbol{B}_t\|}{\|\boldsymbol{B}_t\|} \tag{3.4.2}$$

$$\text{RMSE} \triangleq \frac{\|\boldsymbol{\phi}_r - \boldsymbol{\phi}_t\|}{\sqrt{N_p}} \tag{3.4.3}$$

where $\boldsymbol{B}_r$ and $\boldsymbol{B}_t$ denote the reconstructed and the true B_1 magnitude respectively, $\boldsymbol{\phi}_r$ and $\boldsymbol{\phi}_t$ denote the reconstructed and the true B_1 phase respectively.

Based on this empirical comparison, we believe that the coil combination optimization can improve the SNR of the multi-coil B_1 magnitude and phase estimation. Moreover, we found that the proposed method is robust to inaccurate magnitude related parameters, e.g., B_1 magnitude, receive sensitivities and distributions of spin density, T_1 and T_2. However, unlike the B_1 magnitude estimated by phantom, B_1 phase estimates from phantom were far from the true B_1 phase in brain, causing the inferior performance of method 1. With such big B_1 phase mismatch, the improvement of method 1 over the all-but-one method is mainly from the optimization of the matrix condition number. Since a set of low resolution B_1 phase maps only takes very minimal time in practice, we conclude that method 2 is the more robust and practical method for the coil combination optimization.

Table 3.2: Statistics of the results

	all-but-one	method 1	method 2	oracle
NRMSE of $B_m(\boldsymbol{r})$	36.9%	8.09%	5.62%	4.82%
RMSE of $\phi_m(\boldsymbol{r})$, radians	0.804	0.360	0.274	0.232

3.4.3   Phantom Experiment: Coil Combination Optimization

We also carried out a phantom experiment to demonstrate the proposed coil combination optimization method on the 3T GE scanner with the 8-channel parallel

transmit/receive system, where we still only used the seven working transmit channels. All the data were acquired with the same SPGR-based BS B_1 mapping sequence as used in the previous phantom experiment, and the imaging parameters were also kept the same.

Based on the simulation study discussed earlier, we only compared the all-but-one method and method 2 which is the more robust optimized method. To mimic the on-line *in-vivo* B_1 mapping, we used two phantoms which have different shape and different materials, i.e., a big cylindrical phantom filled with silicon oil and a spherical phantom filled with distilled water. We treated the big cylindrical phantom as the calibration phantom for estimating the B_1 magnitude maps for the optimization algorithm. In addition, the B_1- map was also acquired off-line with this phantom. Since we only did 2D axial B_1 maps, this phantom was carefully positioned to get centered axial images. The smaller spherical phantom was treated as the actual object for which we needed to do the online B_1 mapping, and it was positioned in the scanner such that its axial cross-section is fully covered by that of the bigger silicon oil phantom. As proposed in method 2, fast low resolution pre-scans were done to estimate the B_1 phase maps and the B_0 field map. To better separate the off-line and online procedure, the online experiment with the spherical water phantom was done several days later than the off-line calibration with the cylindrical silicon oil phantom, where the coil was marked to the same positions in the scanner every time. Along with the off-line acquired B_1+ and B_1- magnitude maps and the online acquired B_1+ phase and B_0 maps, uniform spin density, T_2 and T_1 maps were inputted to the optimization algorithm for the optimized coil combination. To introduce some more model mismatch, the uniform T_1 map was intentionally set to $1s$ which is off from the true value, i.e., around $3s$. Similar to the simulation, circulant structure was assumed for the matrix A, and the optimization algorithm was initialized with the all-but-one combination.

We then acquired two sets of complex B_1 maps using the same SPGR-based BS sequence where the optimized coil combination coefficients and the all-but-one coefficients $(\alpha_{1,1} = 0, \alpha_{1,2} = \ldots = \alpha_{1,N} = 1)$ were applied respectively. The non-regularized method was used to reconstruct the B_1 magnitude and phase.
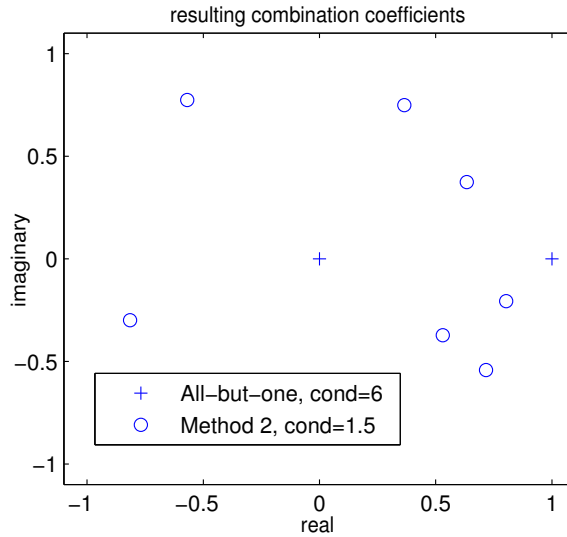
Figure 3.4.8: The first row of the optimized coil combination matrix and that of the all-but-one matrix, where magnitude is normalized to the peak nominal power of the system; the condition numbers of each matrix are shown in the legend.

Fig. 3.4.8 shows the first row of the optimized coil combination matrix A along with that the all-but-one coefficients, and the condition numbers are shown in the legend. Furthermore, the resulting B_1 magnitude and phase maps by these two coil combinations are shown in Fig. 3.4.9. Similar to the simulation study, the optimized coil combination greatly improved the SNR of both the B_1 magnitude and phase estimation, compared to the all-but-one combination. However, there are some bias
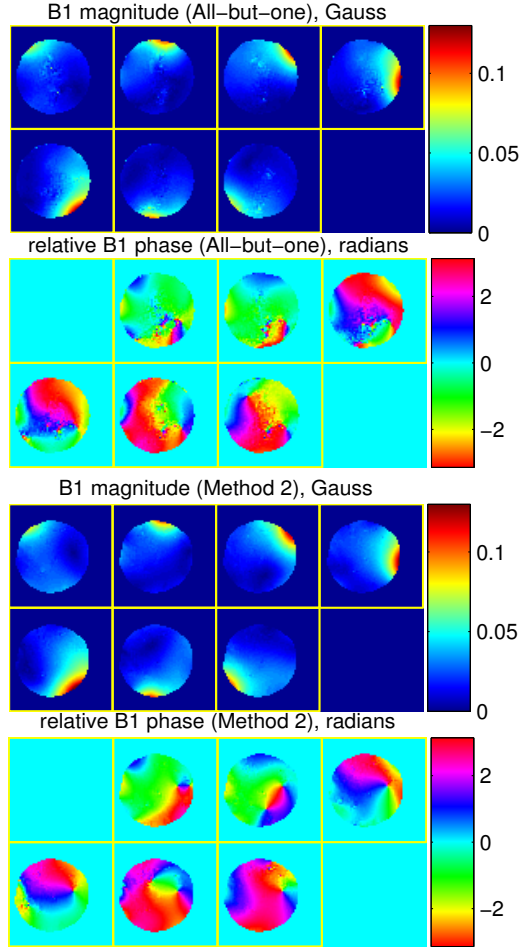
Figure 3.4.9: The resulting B_1 magnitude and phase maps by the two different coil combinations. The B_1 estimates based on the optimized coil combination matrix (bottom two sets of images) have better SNR than the conventional all-but-one approach (top two sets of images).

differences between these two results, especially in the phase maps. This in theory should not happen in a linear parallel excitation system. After some investigation on the system, we suspect that these unexpected effects were caused by uncompensated non-linearity in our custom PEX hardware. This is being corrected, but was irrelevant to the proposed optimization method.

3.5 Discussion and Conclusion

We have proposed methods to improve the BS B_1 mapping for parallel excitation pulse design in the following three aspects: **a) Acquisition speed**: the modified BS B_1 mapping sequence is proposed to get both magnitude and relative phase information, which saves a third of scans that are otherwise required for B_1 phase; **b) Estimation quality**: the regularized method is proposed to jointly estimate the magnitude and phase of multi-coil B1 maps from BS B_1 mapping data, which improves estimation quality by using the prior knowledge of B_1 magnitude and phase; **c) Raw data quality**: the coil combination optimization that is based on CRLB analysis is proposed to directly optimize the SNR of the non-regularized complex B_1 estimation over the whole combination matrix. Combining these three techniques, one can obtain improved complex B_1 estimates of PEX systems with shorter scan time.

The cost function in the regularized B_1 estimation is nonconvex, but our experiments have shown that the initialization by applying the standard BS B_1 mapping and solving (3.2.3) is good enough to obtain a good local minimum with our gradient-based optimization algorithm. The phase regularizer proposed in [68] works well in smoothing B_1 phase in the presence of phase wrap. The CG-LS algorithm efficiently optimizes the highly nonlinear cost function, but a future work can be to design MLS updates for B_1 magnitude like the one for phase to further improve the algorithm efficiency. Other than coil combination optimization, another way to improve the regularized B_1 estimation is to design a direct regularized estimation for the decomposed B_1 magnitude and phase, i.e., $B_n(\boldsymbol{r})$ and $\phi_n(\boldsymbol{r})$, instead of the composite B_1 maps. This could be challenging, because this method will involve an even more nonlinear and nonconvex cost function and it will be very challenging to design MLS updates for both B_1 magnitude and phase.

Our simulation study shows that the optimization results are relatively insensitive

to accuracy of T_1, T_2, spin densities, receive sensitivities and B_1 magnitude for 3T brain imaging. Among these magnitude related parameters, the simulation results were more sensitive to different T_1 values (results not shown). We empirically found that using uniform maps with the maximal T_1 is generally more robust than using other T_1 values for this SPGR-based BS sequence which is a T_1-weighted imaging. Even so, the second phantom experiment still worked reasonably well with T_1 value mismatch. As B_1 phase of the phantom is likely to be far from the *in-vivo* B_1 phase, we prefer method 2 which requires only minimal additional scan time.

The highly nonlinear and nonconvex coil combination optimization produces random-like combination coefficients, and is highly dependent on the initialization and the pseudo-random seeds used in the SA algorithm, so they are probably not global minimums. However, as we only need to find some combination coefficients that can largely improve the raw data, rather than the very best choice, the proposed coil combination optimization method is still useful in practice.

Although the optimized coil combination works in practice, this CRLB analysis is only an approximation because the MLE of B_1 magnitude and phase are biased estimators in general. Furthermore, more estimation bias may be introduced if we include regularization to this method. Thus, future work could be to design a coil combination optimization based on the biased CRLB analysis [122] which is theoretically valid for the proposed regularized estimation.

Although good estimates of B_1 maps may still be achieved with the all-but-one combinations using the regularized estimation, the proposed coil combinations produce raw data with much better SNR, improving robustness of the regularized estimation method. Sometimes, the optimized coil combination yields adequate B_1 estimates without requiring regularization, which may be preferable for practical use.

The proposed coil combination optimization does not constrain specific absorption rate (SAR), which could be of a concern in BS B_1 mapping sequences. Applying

complex weights to PEX channels may cause unpredictable local SAR increase without the knowledge of local electromagnetic properties of the tissue [123], so a future work can be to consider SAR limit in the coil combination optimization, especially for high field PEX B_1 mapping. Following this, a possible further extension will be to apply the coil combination optimization to *in-vivo* experiments for human brain as well as other parts of human body.

The experiments for the coil combination optimization were only based on the 2D SPGR sequence, but the similar principle can be easily applied for any other typical 2D or 3D BS B_1 mapping compatible sequences. In addition, improving coil combination is generally important to other multi-coil B_1 mapping methods, including both phase-based and magnitude-based methods. Although the proposed method was developed for BS B_1 mapping sequence, the framework of the CRLB based coil combination optimization can be applied to other popular mult-coil B_1 mapping methods, e.g., AFI [46].

CHAPTER IV

Four-Dimensional Spectral-Spatial Fat Saturation

Pulse Design[1]

4.1   Introduction

Fat suppression has been widely used in MRI to suppress undesired adipose tissue signals or prevent chemical shift artifacts. One popular method is fat sat(uration) [28], which uses a spectrally selective pulse to saturate and dephase fat spins preceding the actual imaging pulse sequence. Fat sat is compatible with most imaging sequences, but it is sensitive to B_0 and B_1 inhomogeneity. Another popular preparatory pulse for fat suppression is Short T_1 Inversion Recovery pulse (STIR) [75] [76], which is based on the unique T_1 of fat. Although this method is immune to B_0 field inhomogeneity, it has many drawbacks, such as long scan time, reduced signal-to-noise ratio (SNR) of water signal, and altered T_1 contrasts. Instead of preparatory pulses, spectral-spatial (SPSP) pulse was proposed to selectively excite water tissue [30]. This pulse specifies excitation profiles in both spatial and spectral domain, but it is subject to B_0 inhomogeneity and may have drawbacks like poor slice profile or long pulse length.

This work focuses on improving the fat sat method by minimizing the adverse effects of B_0 and B_1 inhomogeneity with short pulses. Our approach to solving this

---

[1]This chapter is based on [94] [33]

problem is to incorporate maps of the 3D B_0 and B_1 fields into the pulse design to excite a 4D SPSP pattern. Morrell *et al.* [31] proposed a similar idea using 3D SPSP pulse to excite 3D patterns (2 spatial and 1 spectral dimensions) based on 2D field maps, to mitigate B_0 inhomogeneity problems for 2D water-only imaging or fat saturation, but this method has limited use for 3D imaging or interleaved multi-slice imaging where 3D field maps are typically needed; moreover, the pulse length of this design was too long for steady-state imaging sequences, and it does not handle B_1 inhomogeneity. With the advent of parallel excitation, Heilman *et al.* proposed efficient pulses to uniformly saturate fat via multi-channel transmitters by tuning the center frequency of each coil to match the variation of B_0 maps [124], but it is difficult for this approach to address complex B_0 patterns and to insure uniform tip angles. Recently, a parallel excitation pulse design for broadband slab selection with B_1 inhomogeneity correction [125] demonstrates the feasibility of addressing some simple spectral profiles by tailored SPSP pulses in 3D k-space (k_x-k_y-k_z). In addition, Malik *et al.* proposed a water selective imaging method using parallel excitation to achieve more complex spectral profiles with SPSP pulses that are based on weighted binomial pulse trains in k_z-k_f of k-space [126]. However, absence of traversing within k_x-k_y may lead to incomplete B_0/B_1 compensation in the transverse plane and thus makes the results highly dependent on the B_0 shimming and configurations of transmit coils.

In this work, we propose to tackle this problem by designing a 4D SPSP fat sat pulse that is tailored for B_0 and B_1 inhomogeneity of the 3D space. The proposed method avoids the need of a sharp transition band in the spectral domain by exploiting the spatial variations of center frequencies, so it can achieve better performance with even shorter pulse length than the standard fat sat pulse. Both single-channel excitation and parallel excitation versions have been developed. We compute this saturation pulse numerically using an iterative algorithm composed of a small-tip angle approximation design and an automatic rescaling step. The proposed method

is compared with the conventional fat sat pulse in phantom experiments and in-vivo experiments on 3T scanners for both the single channel excitation and the parallel excitation versions.

4.2   Theory

We propose a 4D SPSP (1D spectral and 3D spatial) fat sat pulse design with the option of incorporating parallel excitation. The pulse is tailored to match B_0 and B_1 variations of the specified 3D space. It has been shown in [34] that small-tip-angle (STA) approximation can be effective for 90^0 designs except for a scaling factor. So we propose a two-step design: using STA approximation to determine the pulse waveform "shape" and then automatically computing the pulse "amplitude".

Beyond the robustness to B_0 and B_1 inhomogeneity, the proposed method can also significantly improve the pulse efficiency. With certain conditions satisfied, this seemingly harder pulse design actually needs similar or even shorter pulse length than the conventional spectral pulse. The conventional fat sat pulse needs to have a relatively rapid transition between the water and fat spectra to accommodate the B_0 inhomogeneity of the whole 3D volume; in contrast, the 4D SPSP fat sat pulse only needs to handle much narrower spectra of each local voxel, which can be achieved with smoother transition bands in the frequency domain. In other words, the proposed method makes the task in frequency domain easier than the conventional method, and therefore allowing a shorter pulse length.

Fig. 4.2.1 illustrates the difference between the 4D fat sat pulse and the conventional spectral pulse in the frequency domain, where three representative voxels that have different local off-resonance frequencies are shown as examples. The 4D fat sat pulse fits the spectra of the each voxel much better than the spectral pulse that can not accommodate the B_0 variations over the volume. Moreover, the 4D fat sat pulse has a much smoother transition in the spectral domain than the spectral pulse,

reducing the pulse length.
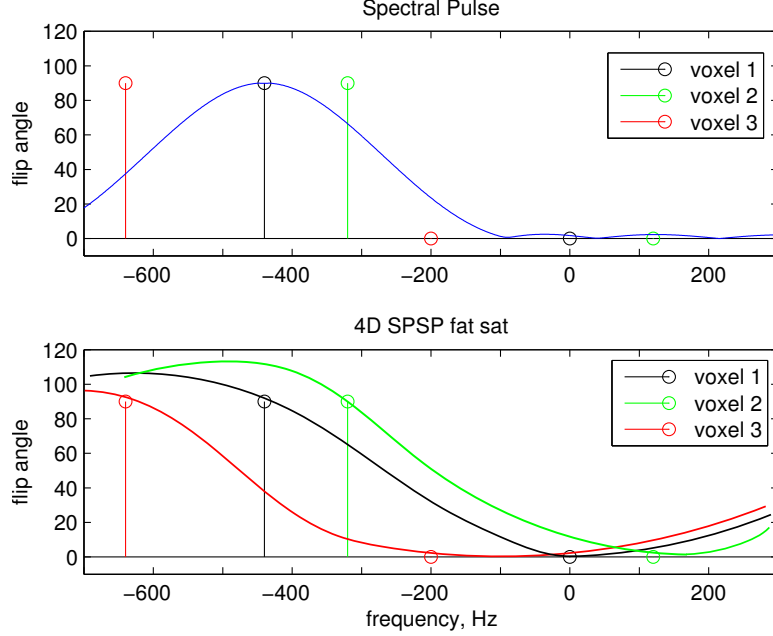
Figure 4.2.1: Illustration of the frequency responses of the SLR fat sat pulse (top) and the 4D fat sat pulse (bottom) in the presence of B_0 inhomogeneity, where 3 voxels at different off-resonance frequencies are selected as examples. The 4D fat sat pulse suppresses fat without exciting water much more effectively with less sharp transition bands.

4.2.1 Step 1: Determine the RF Waveform "Shape"

With the STA approximation, the 4D excitation pattern model is described as follows:

$$m(x, y, z, f) = i\gamma m_0 \sum_r S_r(x, y, z) \int_0^T b_r(t) e^{i2\pi[(x,y,z,f)\cdot \boldsymbol{k}(t)]} dt \qquad (4.2.1)$$

where (x, y, z) is the spatial coordinate, f is frequency, $m(x, y, z, f)$ is the 4D excitation pattern, γ is the gyromagnetic ratio, m_0 is the equilibrium magnetization magnitude, $S_r(x, y, z)$ is the B_1 map of each coil, $b_r(t)$ is the RF pulse of the rth

coil, $r = 1, 2, \ldots, R$, R is the number of transmit coils, T denotes the pulse length, and $\boldsymbol{k}(t) = [k_x(t), k_y(t), k_z(t), k_f(t)]$ denotes the 4D excitation k-space trajectory. In particular, the excitation k-space trajectories are defined to be backward integrals as follows:

$$k_x(t) = -\frac{\gamma}{2\pi} \int_t^T G_x(\tau)d\tau, \quad k_f(t) = t - T \tag{4.2.2}$$

where x can also be y or z. The system equation [4.2.1] can be discretized as follows:

$$\boldsymbol{m} = \boldsymbol{A_s}\boldsymbol{b} \tag{4.2.3}$$

where $\boldsymbol{m}$ $(N_s \times 1)$ is the vector that contains N_s samples of the 4D excitation pattern, $\boldsymbol{A_s} = [\boldsymbol{S_1}A \ \boldsymbol{S_2}A \ldots \boldsymbol{S_R}\boldsymbol{A}]$, $\boldsymbol{b} = [\boldsymbol{b_1^T} \ \boldsymbol{b_2^T} \ldots \boldsymbol{b_R^T}]^T$, $\boldsymbol{A}$ $(N_s \times N_t)$ is system matrix that transform the RF pulse of each coil into the 4D pattern without considering the sensitivity map, i.e. $a_{ij} = i\gamma m_0 e^{i2\pi(x_i,y_i,z_i,f_i)\cdot\boldsymbol{k}(t_j)}$, $\boldsymbol{S_r}$ $(N_s \times N_s)$ is a block diagonal matrix which contains the corresponding sensitivity maps of each coil repeated for each spectral sample, $\boldsymbol{b_r}$ $(N_t \times 1)$ is the vector of samples of the RF pulse transmitted by each coil.

To do fat sat, the 4D target excitation pattern uniformly has 90^0 tip angles for the fat spectra and 0 for the water spectra in each voxel. To compensate for B_0 inhomogeneity, the positions of the fat and water bands of each voxel in the target pattern need to shift according to the 3D B_0 map. B_1 maps are input into [4.2.1] to compensate for B_1 inhomogeneity. In this 4D target pattern, most of the spectrum is a "don't care" region and can be masked out in the cost function to gain more degrees of freedom in the design; furthermore, the region outside the object can also be excluded from the target pattern. The pattern is illustrated in Fig. 4.2.2 with a 2D SPSP example.
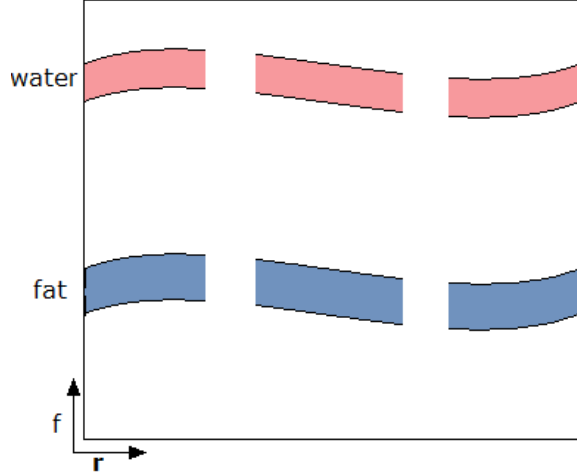
Figure 4.2.2: Illustration of the 4D SPSP target pattern with a 2D SPSP (1D spatial + 1D spectral) example. The pink band represents water band and the blue band represents fat band, and their positions in the frequency directions vary according to local off-resonance frequencies. All the regions in white are "don't care" regions that can be masked out in the design.

With the system equation [4.2.3] and the target pattern, we design the pulses by iteratively optimizing a cost function that contains a target pattern fitting term and a regularization term for RF power penalization [34]. Furthermore, since the transverse phase of fat spins is not important, we apply magnitude least square (MLS) optimization [35] to increase some degrees of freedom for the pulse design, where the final cost function can be described as:

$$\Phi(\boldsymbol{b}) = \|\boldsymbol{P} - |\boldsymbol{A_s b}|\|_W^2 + \beta \|\boldsymbol{b}\|_2^2 \qquad (4.2.4)$$

where $\boldsymbol{P}\,(N_s \times 1)$ is the real-valued 4D target pattern, $\|\cdot\|_W$ denotes the weighted l_2 norm that masks out the "don't care" region of the target pattern, and $\beta\|\boldsymbol{b}\|_2^2$ denotes the regularization term that penalizes the RF power and β is a scalar parameter. We use the approach proposed in [127] to solve this nonlinear optimization problem, which is to introduce another unknown vector $\boldsymbol{\phi}\,(N_s \times 1)$ to the cost function and

alternately minimizes the new cost function [4.2.5] over $\boldsymbol{b}$ and $\boldsymbol{\phi}$:

$$\Phi(\boldsymbol{b}, \boldsymbol{\phi}) = \|\boldsymbol{P}. * e^{j\boldsymbol{\phi}} - \boldsymbol{A_s b}\|_W^2 + \beta\|\boldsymbol{b}\|_2^2 \qquad (4.2.5)$$

where $e^{j\boldsymbol{\phi}}$ ($N_s \times 1$) denotes the vector with elements $e^{j\phi_i}$, $i = 1, 2, ..., N_s$, and ".*" denotes the element-by-element multiplication of two vectors. In particular, the step of updating $\boldsymbol{b}$ is implemented by using conjugate gradient algorithm [34] and nonuniform fast Fourier transform [24]; $\boldsymbol{\phi}$ is updated in each iteration by taking the phase of the latest value of $\boldsymbol{A_s b}$, i.e., $\boldsymbol{\phi}^{(n)} = \angle\{\boldsymbol{A_s b}^{(n)}\}$.

As the cost function [4.2.5] is non-convex over $\boldsymbol{\phi}$, it needs to be initialized carefully to reach a good local minimum. There have been several different methods for the phase pattern initialization, such as zero phase and random phase [127], but none of them worked well in our implementation. Thus, we proposed a different initial phase pattern for this special problem, i.e., $\phi(x, y, z, f) = -2\pi f\frac{T}{2}$, and it worked much better than those conventional initialization methods in our designs. Because the original target pattern with $\boldsymbol{\phi} = \boldsymbol{0}$ is real and slowly varying over space, then the high energy parts of its k-space representation should be concentrated around the origin of the k-space; however, since the coverage of k_f is only over the non-positive part, i.e. from $-T$ to 0, it can only cover half of the high energy parts of this target pattern in k-space. Hence setting $\phi(x, y, z, f)$ to be $-2\pi f\frac{T}{2}$ solves this problem by shifting the target k-space by $T/2$ towards the negative part of k_f, which makes it possible to capture the most high energy parts of the target pattern in k-space. The initial phase pattern works very well in practice, but it is not the only choice and may not be the best. While keeping $\phi(x, y, z, f)$ a linear function of frequency, there are still many degrees of freedom to customize $\phi(x, y, z, f)$ to vary over spatial locations for each frequency. Therefore, there may exist better initial patterns of $\phi(x, y, z, f)$ than the proposed solution. This is still under investigation, and randomly varying

$\phi(x, y, z, f)$ over (x, y, z) while keeping it linear over f is a good point to start with.

The gradient waveforms need to be set to traverse the 4D excitation k-space $(k_x - k_y - k_z - k_f)$, which is achieved by repeating a 3D k-space trajectory $(k_x - k_y - k_z)$ multiple times. We investigate two different types of 3D excitation k-space trajectories for traversing $k_x - k_y - k_z$: the "spoke" trajectory (also known as "fast-kz" trajectory) [37] and the "Spiral Nonselective (SPINS)" trajectory [128]. The spoke trajectory is efficient when k_z needs to be sampled more densely than $k_x - k_y$, such as 2D B_1 inhomogeneity compensation with slice selection [37]. Thus, this trajectory seems sub-optimal for our problem that has nearly isotropic variations in the 3D volume. In contrast, the SPINS trajectory, which is targeted for non-selective excitation, seems to be a better option in terms of efficiency. Moreover, as the SPINS trajectory traverses k-space center more densely and more slowly, specific absorption rate (SAR) and/or peak RF power could be smaller than those of the spoke trajectory. However, we still think it is unknown which one is better for this problem, because: a) When using parallel excitation which usually only produces in-plane variations, the spoke trajectory may gain more efficiency than the SPINS trajectory, as k_z may need sampling more densely than $k_x - k_y$; b) compared to SPINS trajectory, the spoke trajectory has fewer parameters and those parameters are more intuitive and more adjustable; c) Several methods have been proposed to optimize the spoke trajectory [20–22, 129] while optimization of the SPINS trajectory remains much more challenging. We experimentally compared these two trajectories in terms of various practical specifications. Fig. 4.2.3 shows examples of these two trajectories respectively, where $k_x - k_y - k_z$ coverage is restricted such that k_f is sampled adequately densely.
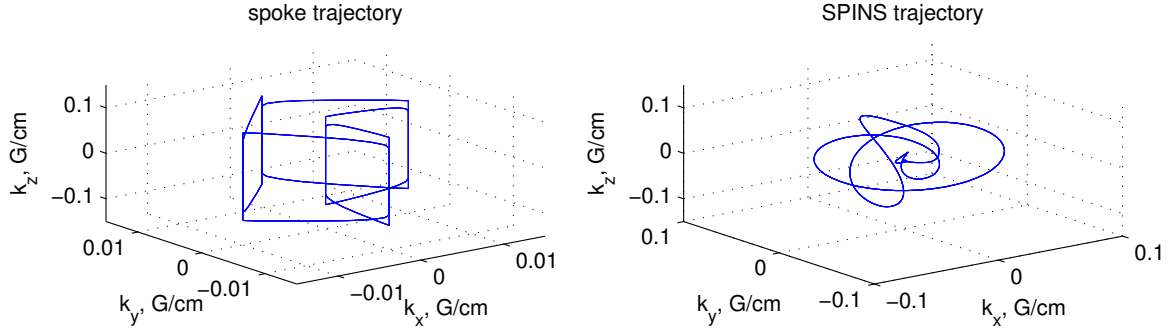
Figure 4.2.3: Examples of the spoke trajectory (left) and SPINS trajectory (right) that are used in this work.

4.2.2 Step 2: Determine the "Amplitude"

STA design only determines the pulse waveform "shape", and the designed pulses still need to be properly rescaled to uniformly saturate the fat spins. To make the design practical for in-vivo scans, we need an efficient and accurate way to determine the pulse "amplitude". Although existing large-tip parallel excitation design methods [14] [15] [16] are able to automate the design process, they would be very computationally intensive for this problem. Thus, assuming the pulses designed in step 1 only need to be properly rescaled, we designed a simple iterative process to determine the pulse "amplitude":

(1) A few, e.g., 50, pixels in the fat band that are best fit to the desired excitation pattern for the STA design in step 1 are selected.

(2) Apply the pulse $b^{(0)}$ designed by STA to the Bloch equation simulation and only compute for the points selected, and it then produces an average of tip angle $\theta^{(0)} < 90^0$. $(n = 0)$

(3) while $(|\theta^{(n)} - 90^0| > \epsilon)$ {

   (a) The pulse is updated to be $b^{(n+1)} = [\frac{1+\sin(90^0-\theta^{(n)})}{\sin(90^0)}]b^{(n)}$;

   (b) Repeat (2) for $b^{(n+1)}$ and get an average tip angle $\theta^{(n+1)}$;

   (c) $n = n + 1$;

}

When the pulses achieve uniform patterns for fat, this strategy is equivalent to the additive-angle method [14]. Since there is only one scalar to determine in this step, only a few pixels are sufficient; then the computation for Bloch equation simulation is very fast. Moreover, since 90^0 is relatively "small" in the large-tip excitation regime, this algorithm usually appears to converge in a few iterations. In practice, this step takes less than a second in Matlab (The Mathworks, Natick MA).

4.3 METHODS

The proposed method is compared with the conventional spectrally selective fat sat pulse in a series of 3T experiments. In the phantom experiments, the spoke trajectory and the SPINS trajectory were both evaluated for single channel and parallel excitation versions. The proposed method was also applied to human knee imaging. All of the experiments were performed on two GE 3T scanners (GE Healthcare, Milwaukee, WI, USA), using GE single channel transmit/receive head coils or an eight-channel custom parallel transmit/receive system [111] [112].
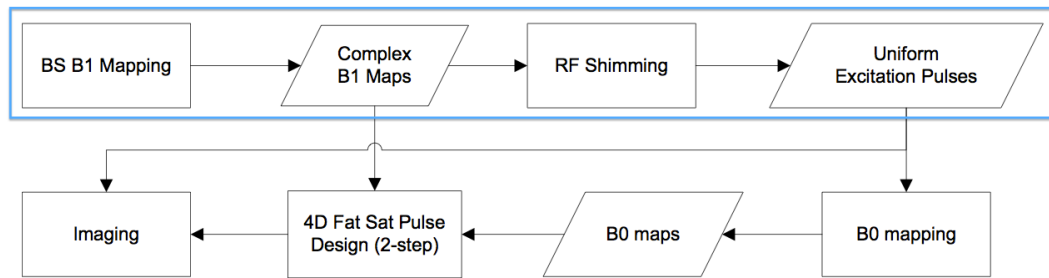
Figure 4.3.1: The flowchart of the 4D fat sat pulse design and imaging procedure. The steps in the blue box were only used in parallel excitation experiments.

4.3.1 Pulse Design

The proposed method is compared with the conventional spectrally selective fat sat pulse which is designed by the Shinnar-Le Roux (SLR) algorithm [18]. The SLR fat sat pulse is 5 ms long and has a 400 Hz minimal phase passband for fat (center frequency is -440 Hz), which is typically used for 3T fat sat. For each pulse sequence, the amplitude of the pulse was properly adjusted to saturate the on-resonance fat spins.

The procedure of the proposed 4D fat sat pulse design is summarized in the flowchart in Fig. 4.3.1. The steps in the blue box, which are for B_1 mapping and RF shimming, were only used in the parallel excitation experiments, as we found that B_1 inhomogeneity was acceptable in our 3T single-channel excitation experiments. For applications that are more susceptible to B_1 inhomogeneity, e.g., abdominal imaging in the presence of ascites [74], it may be necessary to incorporate B_1 maps in the design for single-channel excitation experiments. In the parallel excitation experiments, the required eight-channel complex B_1 maps (B_1 magnitude and relative phase maps) were acquired by using a modified Bloch-Siegert (BS) B_1 mapping method [1, 92, 93] which produces both B_1 magnitude and phase maps with optimized SNR. Moreover, RF shimming [130] was applied to achieve uniform excitation in the parallel excitation system, where the magnitude and phase of each coil of the transmit array were adjusted according to the complex B_1 maps. With the uniform excitation, we can obtain the B_0 maps from the phase difference of two Gradient echo images that have different echo times, and the echo time difference needs to be set such that the water and fat spins are in-phase, e.g., $\Delta T_E = 2.272$ ms on 3T scanners. The B_0 and B_1 maps are then put into the proposed 2-step 4D fat sat pulse design routine to get the desired fat sat pulses. Finally, the uniform excitation pulse and the designed 4D fat sat pulse are loaded onto the scanner to acquire the fat suppressed images.

Although this high dimensional design is computationally intensive, we still achieved

a practical design time by using the following strategies. First, we coarsely sample the 4D spectral-spatial domain, based on the following assumptions: (a) The target pattern varies smoothly with the B_0 and B_1 maps over the 3D spatial domain; (b) The spectra of fat and water in each voxel are relatively narrow and far apart. Second, most parts (usually 80% - 90%) of the 4D SPSP domain are "don't care" regions that can be masked out. Furthermore, as discussed in Section 4.2, the relatively small $k_x - k_y - k_z$ coverage and short k_f coverage, which respectively satisfies the sampling rate along k_f and shortens pulse length, also help to reduce the size of the system matrix. The voxel size of the target pattern and the corresponding B_0 and B_1 maps was around 1 cm^3, and the sampling rate in the frequency domain was about 20 Hz/point. The bandwidths of water and fat were set to be 40 Hz and 80 Hz respectively. The spoke trajectory samples 5 $k_x - k_y$ points as shown in Fig. 4.2.3, where the locations of $k_x - k_y$ samples were empirically chosen to be uniform around the origin. The SPINS trajectory was designed according to the parameters suggested in [128]. The maximal gradient slew rate of both trajectories were driven towards the system limits, which is 180 Tm^{-1}s^{-1}. The sampling interval along k_f, i.e., the time for traversing $k_x - k_y - k_z$, was below 1 ms, keeping any possible aliases in frequency domain at least 1 kHz away from each other.

All of our pulse designs were implemented in Matlab 7.8 on a workstation equipped with Intel Core2 Quad CPU Q9400 @ 2.66 GHz and 4 GB RAM, which takes about 1-2 mins for the single-channel excitation pulse and about 3-5 mins for the parallel excitation pulse. The computation time would be acceptable in practice with a more efficient implementation and a faster computer.

4.3.2 Phantom Experiments with Single Channel Excitation

We then carried out two phantom experiments to test the single-channel excitation version of the 4D fat sat pulse. The first phantom experiment (called "experiment 1"

hereafter) compares the proposed method with the SLR fat sat pulse, and the second experiment (called "experiment 2" hereafter) studies the proposed method with different trajectories and pulse lengths. A cylindrical phantom filled with distilled water (CuSO4 doped) and mineral oil was used for all those experiments.

In experiment 1, we designed a 4.8 ms 4D fat sat pulse for a 14 cm $\times$14 cm $\times$6 cm axial slab of the phantom based on its multi-slice B_0 maps (Fig. 4.4.1). The spoke trajectory was applied with sampling period along k_f of 0.6 ms and 9 k_f samples. No RF power penalization was applied. It is compared with the 5 ms SLR fat sat pulse. We implemented the standard fat saturation scheme where the fat sat pulse is followed by a multi-slice 2D interleaved spiral-out readout. To measure the residual M_z, we play each sequence twice (turn fat sat on or off) with the same parameters: $T_E = 6$ ms, $T_R = 15$ s, FOV $= 14$ cm, slice thickness $= 4$ mm, 15 slices, 4 interleaves, reconstruction size is 64×64. A long T_R is used so that we could approximately calculate the absolute value of the normalized residual M_z by taking the ratio: $|M_z| \approx |$the fat saturated image$|/|$the non-fat-sat image$|$.

In experiment 2, we applied the 4D fat sat pulse with the spoke and SPINS trajectories as well as the SLR fat sat pulse on the same phantom. A 3D spoiled gradient-echo sequence (SPGR) with FOV 14 cm $\times$14 cm $\times$7 cm was applied to acquire the B_0 map (Fig. 4.4.3). We then designed 4 different 4D fat sat pulses, which are 4.8 ms or 2.5 ms 4D fat sat pulses with a spoke or SPINS trajectory. The two 4.8 ms pulses both sample k_f 9 times, while the two 2.5 ms pulses sample k_f 5 times. Among these four pulses, only the 2.5 ms spoke pulse used RF power penalization. The pulses were tested with 3D SPGR sequences that have a 7 cm slab-select excitation and spin-warp readout, and the imaging parameters were: $T_R = 213$ ms, FOV $= 14$ cm $\times$14 cm $\times$7 cm, data size $= 64 \times 64 \times 15$. For each pulse, a pair of 3D images were acquired with fat sat on or off.

4.3.3 Phantom Experiments with Parallel Excitation

The parallel excitation version of 4D fat sat pulses was tested on the same phantom, which is called "experiment 3" hereafter. Due to partial amplifier failure, we only used 4 of the 8 parallel excitation coils for transmission while all 8 parallel receive channels were used. 2D B_1 maps of the parallel transmit channels were acquired and shown in Fig. 4.4.4. They were then stacked up to form the 3D B_1 maps, assuming uniform B_1 field along z. We then designed the complex weights for uniform excitation using RF shimming. Then we acquired the 3D B_0 map (Fig. 4.4.4) using a 3D SPGR squence with FOV 14 cm $\times$14 cm $\times$10.5 cm, where a 5.9 cm thick axial slab was used for the pulse design.

We designed 4.8 ms or 2.7 ms 4D fat sat pulses with a spoke or SPINS trajectory, each of which employed the "heuristically optimized" k-space trajectory: the 4.8 ms spoke trajectory samples k_f every 0.6 ms for 9 times; the 4.8 ms SPINS trajectory samples k_f about every 1 ms for 5 times; the 2.7 ms SPINS trajectory samples k_f every 0.54 ms for 5 times. We did not test spoke pulses shorter than 4.8 ms, which is discussed in Discussion section. All the designs required RF power penalization to satisfy the power limit of the amplifiers. The SLR fat sat pulse with the weights for uniform excitation was also applied for comparison.

All the pulses were tested with 3D SPGR sequences that have a non-selective excitation and spin-warp readout, and the imaging parameters were: $T_R = 80$ ms, FOV = 14 cm $\times$14 cm $\times$10.5 cm, data size = $64 \times 64 \times 48$. For each pulse, a pair of 3D images were acquired with fat sat on or off. Note that the raw data were 8-channel parallel imaging data, and they were combined using the receive side B_1 shimming according to the receive sensitivity maps acquired off-line. The results shown in Result section are all combined images.

4.3.4 In-Vivo Experiments with Single Channel Excitation

The 4D fat sat pulse with single-channel excitation was demonstrated in a knee imaging experiment (called "experiment 4" hereafter). A healthy volunteer participated with approval by the Institutional Review Board of the University of Michigan, after providing informed consent. To insure safety, a relatively long repetition time was used and global SAR was monitored during the experiments. Since head coil may underestimate the global SAR for knee imaging, we kept the monitored global SAR values on the scanner below 5% of the relevant limit. We used the 2.5 ms 4D fat sat pulse with SPINS trajectory which worked best in the single-channel excitation phantom experiments and compared it with the 5 ms SLR fat sat pulse. The 3D B_0 map of a 28 cm ×28 cm ×6.5 cm ($64 \times 64 \times 13$) axial slab of human knees was acquired with a 3D SPGR sequence, and Fig. 4.4.5 shows two representative slices. No penalization was put on peak RF power. Both of the fat sat pulses were tested with 3D SPGR sequences that have a slab-select excitation and spin-warp readout, and the imaging parameters were: $T_R = 91$ ms, minimal T_E, nominal flip angle was 20^0, FOV = 28 cm ×14 cm ×6.5 cm, data size = $256 \times 128 \times 13$.

Table 4.1: The List of Experiments

	objects	equipment	trajectories
Experiment 1	phantom	single-channel excitation	spoke
Experiment 2	phantom	single-channel excitation	spoke, SPINS
Experiment 3	phantom	parallel excitation	spoke, SPINS
Experiment 4	knees	single-channel excitation	SPINS
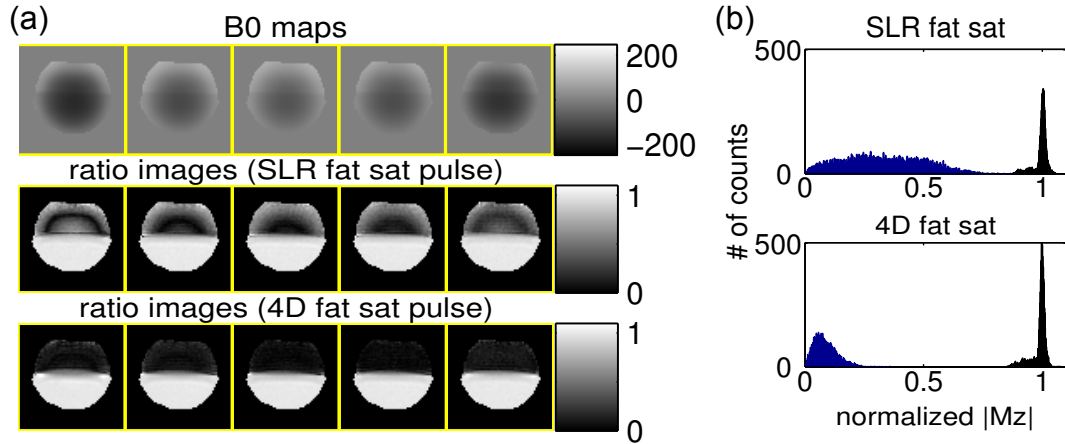
Figure 4.4.1: The B_0 maps and the results of experiment 1. (a) Top: the B_0 maps (in Hz); Middle and bottom: the ratio images by the SLR fat sat pulse (middle) or the 4D fat sat pulse (bottom), where the ratio images are the ratio between the images with fat sat and the ones without fat sat; Note that oil is on the top and water is the bottom in each image, and every third of the axial slices is shown. (b) The histograms (200 bins) of the water (black) and fat (blue) M_z according to the ratio images of all the slices, where the SLR fat sat pulse (top) is compared with the 4D fat sat pulse (bottom).

4.4 RESULTS

4.4.1 Phantom Experiments with Single Channel Excitation

The results (every third slice) of experiment 1 are shown in Fig. 4.4.1 where 4D fat sat pulse is compared with SLR fat sat pulse. Oil is on top of water in the images, and we show the ratio images mentioned in the Methods section which is approximately the absolute value of the normalized residual M_z after the fat sat pulse. By manually selecting the water and fat parts in the images, we put together the histograms of the residual M_z of water and fat parts by the two pulses in Fig. 4.4.1(b). Compared to the SLR fat sat pulse, the 4D fat sat pulse worked nearly the same or a little better for water but much better for fat. Note that some of the M_z of water is greater than 1, which is physically impossible, and the reasons could be artifacts of the spiral

106

imaging and random data noise.
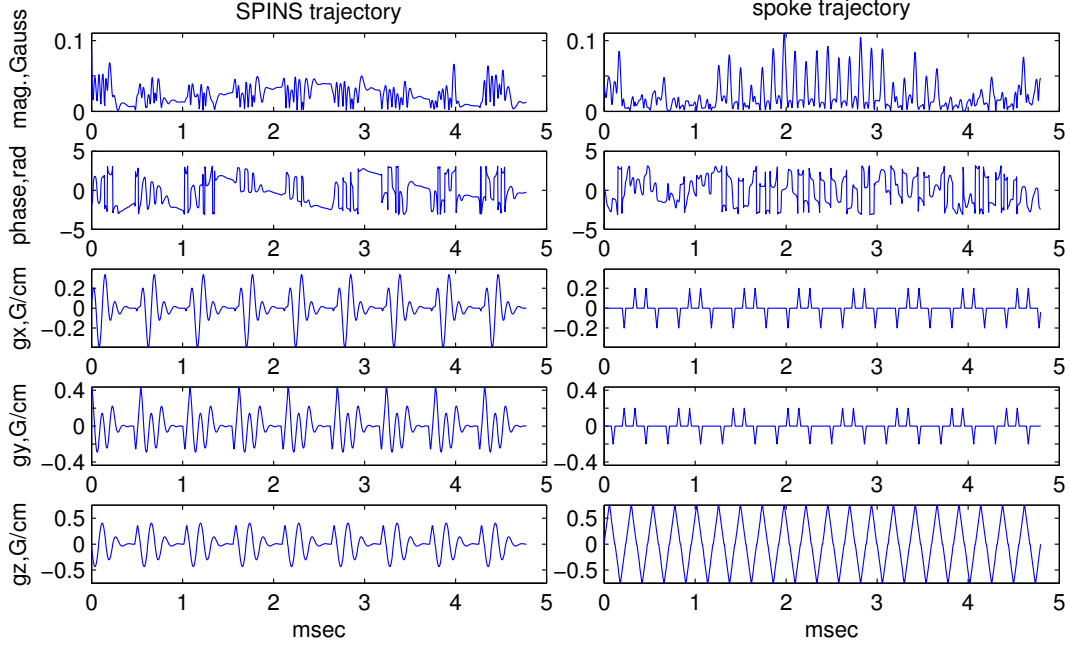
Figure 4.4.2: Examples of the designed 4D fat sat pulses: 4.8 ms 4D fat sat pulse with SPINS trajectory (left); 4.8 ms 4D fat sat pulse with spoke trajectory (right).

In experiment 2, we tested and compared the proposed method with four different k-space trajectories, and Fig. 4.4.2 shows examples of the designed pulses with a spoke or SPINS trajectory. Compared to the spoke trajectory which traverses much faster along k_z, the SPINS trajectory traverses excitation k-space more uniformly and has a smoother and slower transition around the $k_x - k_y - k_z$ center. Hence, the RF power of the SPINS pulse varies less over time and has smaller peak RF power and average power deposition for a given flip angle and pulse length, compared to the spoke pulse. The total RF energy of each pulse, which has been suggested as a
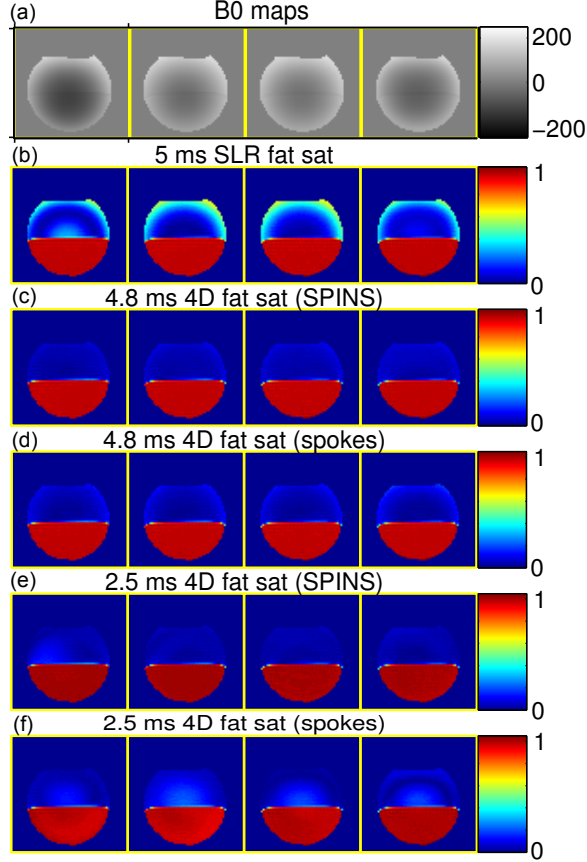
Figure 4.4.3: The B_0 maps and the results of experiment 2, where every third of the axial slices is shown. (a) The B_0 maps (in Hz); (b)-(f) The ratio images by different pulses: (b) 5 ms SLR fat sat pulse, (c) 4.8 ms 4D fat sat pulse with SPINS trajectory or (d) spoke trajectory, (e) 2.5 ms 4D fat sat pulse with SPINS trajectory or (f) spoke trajectory. The ratio images are still the ratio between the images with fat sat and the ones without fat sat, and oil is still on top of water.

surrogate for measuring relative global SAR [131], was calculated using the following formula:

$$E = \int |b(t)|^2 dt \qquad (4.4.1)$$

The results of the four 4D fat sat pulses and the SLR fat sat pulse are summarized in Table 4.2. We also recorded the global SAR of the sequences used in the experiment from the scanner console under a relatively extreme condition, i.e., T_R of the 3D SPGR sequence was set to be the minimum (13 ms), the results of which are also

shown in Table 4.2. Subtracting SAR of the sequence with no fat sat from the other SAR values in Table 4.2 yields the SAR values induced only by the fat sat pulses, and the values turn out to be roughly proportional to the calculated RF energy values. As expected, the 4D fat sat pulses has much more power than the SLR fat sat pulse, the shorter 4D fat sat pulses induced more SAR than the longer ones, and the SPINS pulses have lower power than the spoke pulses. Although the density of the RF pulses was almost set to be the highest possible, the global SAR is still far below the relevant limit.

Table 4.2: RF energy and measured global SAR in experiment 2

	RF energy $(G^2 \mu s)$	global SAR (W/kg)
5 ms SLR pulse	1.1	0.2
4.8 ms SPINS	9.0	0.4
4.8 ms spokes	11.3	0.4
2.5 ms SPINS	30.5	0.9
2.5 ms spokes	49.3	1.4
no fat sat		0.2

As in experiment 1, the ratio images (every third slice) produced by the five different sequences are shown in Fig. 4.4.3, where fat is still on top of water. To highlight the differences in the fat parts, we show the ratio images in color. The mean and the standard deviation of manually selected fat and water parts in each set of ratio images are shown in Table 4.3. All the pulses kept the water signal very well, but the 4D fat sat pulses worked much better than the SLR fat sat pulse in the fat part in the presence of B_0 inhomogeneity (Fig. 4.4.3). Both of the 4.8 ms 4D fat sat pulses worked very well, and the SPINS pulse is a little better in fat as shown in Fig. 4.4.3 and Table 4.3. In contrast, the 2.5 ms SPINS pulse worked much better than the 2.5 ms spoke pulse. Compared to the 4.8 ms SPINS pulse, the 2.5 ms SPINS pulse worked similarly in terms of overall performance; specifically, it has better mean values in both fat and water but bigger variation in the fat part than the 4.8 ms SPINS pulse (Table 4.3). Since SAR may not be an issue here, we think the

2.5 ms SPINS pulse is the best choice for single-channel excitation studies in terms of pulse length and overall performance.

Table 4.3: Statistics of experiment 2

	mean (fat)	std (fat)	mean (water)	std (water)
5 ms SLR	0.220	0.16	0.974	0.010
4.8 ms SPINS	0.0532	0.024	0.974	0.0077
4.8 ms spokes	0.0598	0.037	0.975	0.0079
2.5 ms SPINS	0.0483	0.040	1.00	0.0084
2.5 ms spokes	0.0784	0.051	0.982	0.018

4.4.2 Phantom Experiments with Parallel Excitation

Similar to the previous phantom experiments, we calculated the ratio images produced by the four different parallel excitation pulses mentioned in Methods section. Every sixth of the 26 axial images and their corresponding field maps are displayed in Fig. 4.4.4. By manually selecting the fat and water parts, the histograms of water and fat parts in the ratio images are shown in Fig. 4.4.4(d). As can be seen, the spoke trajectories still suppressed fat much more robustly than the SLR fat sat pulses in the presence of both B_0 and B_1 inhomogeneity, and all of them worked similarly for water. Due to lower SNR of the parallel excitation system, there are more ratio values in the water part that are greater than 1, compared to the single-channel excitation experiments. Comparing the three 4D fat sat pulses, the 4.8 ms spoke pulse worked the best; the overall performance of the two SPINS trajectories is similar, but the 2.7 ms SPINS pulse worked less robustly in the first few axial slices, one of which is shown in the first column of Fig. 4.4.4(c).

4.4.3 In-Vivo Experiments with Single Channel Excitation

The results of experiment 4 are shown in Fig. 4.4.5, where we display two representative axial slices. Compared to the images without fat sat, both fat suppressed images suppressed the fat inside the marrow, and the 4D fat sat pulse worked slightly

110
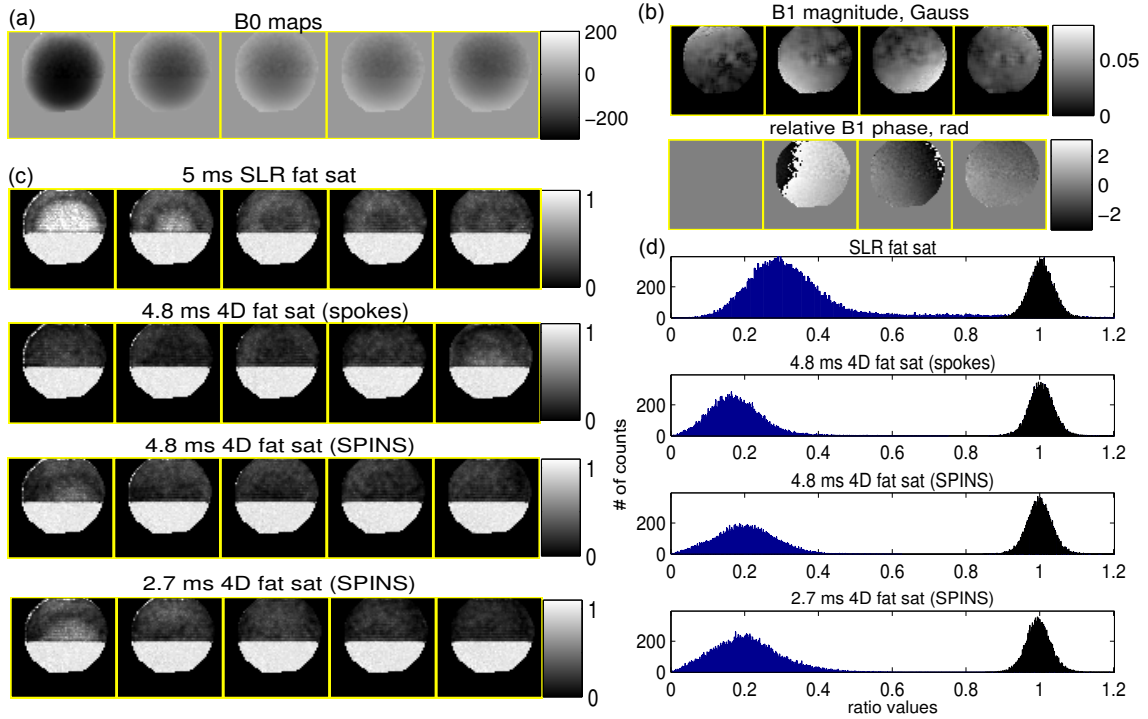
Figure 4.4.4: The B_0/B_1 maps and the results of experiment 3. (a) The B_0 maps (in Hz), where every sixth of the axial slices is shown. (b) The 4-channel B_1 magnitude (top) and relative phase (bottom) of a 2D slice. (c) The ratio images corresponding to (a) by different pulses; 1st row: 5 ms SLR fat sat pulse; 2nd row: 4.8 ms 4D fat sat pulse with spoke trajectory; 3rd row: 4.8 ms 4D fat sat pulse with SPINS trajectory; 4th row: 2.7 ms 4D fat sat pulse with SPINS trajectory; The ratio images are still the ratio between the images with fat sat and the ones without fat sat, and oil is still on top of water. (d) The histograms of the water (black, 200 bins) and fat (blue, 500 bins) M_z according to the ratio images of all the slices.

better. For the fat outside the bones and muscles where B_0 field is more inhomogeneous, the 2.5 ms 4D fat sat pulse worked much better than the 5 ms SLR fat sat pulse.

111

4.5 DISCUSSION

The proposed 4D SPSP fat sat pulse has been demonstrated in various 3T scanner experiments, showing that it can more robustly suppress fat signals with a similar or shorter pulse length in the presence of B_0 and B_1 inhomogeneity compared to the conventional SLR fat sat pulse.

By using the spatial information, the proposed method formulates the fat sat problem as a 4D spectral-spatial problem, which seems more complicated but in fact is quite sensible, as the conventional spectral pulse is generally inefficient for fat sat problems: a) in fact, the SLR fat sat pulse oversamples k_f (time) domain which, for example, only needs sampling about every 1 ms at 3T, so it has a lot of idle time between the necessary samples, which is efficiently used to handle the spatial variations in the 4D fat sat pulse. b) The spectral domain problem is easier when the spatial domain is exploited, as much smaller spatial variations of center frequencies need to be accommodated in the 4D fat sat design, which can largely reduce the pulse length; this is also true when the B_0 /B_1 fields are relatively uniform, where not much $k_x - k_y - k_z$ needs to be traversed, and the 4D fat sat pulse will become similar to a SLR fat sat pulse with a very smooth transition band, which can be much shorter than the standard SLR fat sat pulse. On the other hand, when B_0/B_1 fields have large spatial variations, the design requires large $k_x - k_y - k_z$ coverage which is limited by the k_f sampling rate. So as long as the $k_x - k_y - k_z$ coverage can still address the spatial variations, the pulse length will still be as short; otherwise, pulse length will need to be longer, so that a sharper spectral transition band can be obtained to handle the local spatial variations that are not fully compensated by the limited $k_x - k_y - k_z$ coverages.

We assume certain chemical shifts of fat, e.g., 440 Hz at 3T, which could be inaccurate. In fact, such inaccuracy does not affect the result much within a certain range, because the error of chemical shift will be absorbed into the B_0 map acquired

with the ΔT_E corresponding to the same inaccurate chemical shift, which only makes the design a little harder due to the discontinuous transitions between water and fat in the B_0 map. In the experimental results, however, there were still some residual fat signals that are higher than simulated. It could be caused by some imperfect system conditions, e.g., non-ideal gradient waveforms, inaccurate B_0/B_1 maps, field drift, and inaccurate RF power calibration. In addition, multiple peaks of fat spectrum [74] are not considered in this method, and therefore some minor fat components can not be suppressed.

We have empirically compared the 4D fat sat pulse with different trajectories in experiment 2 and 3. The SPINS pulses worked better than the spoke pulses in experiment 2 in terms of performance and SAR. However, no clear conclusion can be drawn in experiment 3, because although the spoke pulses gain more efficiency from parallel excitation, they need greater performance penalty in order to satisfy the peak RF power limit. All of the 4D fat sat pulses in experiment 3 were designed with peak RF power penalization. As the SPINS pulse naturally has smaller peak RF power than the spoke pulse, there was less of a performance compromise with the SPINS pulse relative to the spoke pulse. We did not test other spoke trajectories that are shorter than 4.8 ms in experiment 3, because the shorter ones, which need even more RF power, had much poorer performance than the 2.7 ms SPINS trajectory in simulations that penalized RF power. Although the 4.8 ms spoke pulse worked only slightly better than the SPINS trajectories in experiment 3, the spoke trajectories had more advantage in simulations without penalizing peak RF power, including the spoke trajectories shorter than 3 ms. So, as we discussed in Theory section, the spoke pulse with the parallel excitation could work better than the SPINS pulse, but the practical limitations on peak RF power reduce the advantage of the spoke pulse. Moreover, SAR in the parallel excitation experiments, which can not be evaluated by equation [4.4.1] or global SAR, needs more investigation, and this may limit the performance of

the spoke pulses further. So, the choice of trajectory in the parallel excitation version depends on specific situations. Furthermore, in addition to these empirical experiments where the trajectory parameters were heuristically chosen, more systematic and rigorous studies can be carried out to compare these two trajectories, e.g., pulse design with joint trajectory optimization. Future studies may also include a study of other types of 3D trajectories that are more suitable for this application. One popular 3D trajectory is the stack-of-spiral trajectory [36], but this trajectory can be very inefficient for a non-spatial-selective pulse design like this work. It is efficient for the patterns where in-plane variations dominate, which is generally not the case in the fat sat problem. As the efficiency for traversing $k_x - k_y - k_z$ is very important in our method, stack-of-spiral trajectory will generally be suboptimal compared to the two trajectories used in this work. Another candidate could be the k_T-points trajectory which is an efficient non-selective trajectory for 3D field inhomogeneity compensation [132]. This trajectory can be automatically optimized easily and also is able to lower peak RF power and SAR, which are favorable for this 4D fat sat pulse problem.

As shown in the results, the single-channel excitation design worked well enough with B_1 inhomogeneity ignored on 3T scanners. In contrast, the parallel excitation pulses worked more poorly than the corresponding single-channel excitation pulses, in terms of performance and the required pulse length. Part of the reason is that the custom hardware may have had some imperfections, such as nonlinearity of the RF amplifiers and some eddy current problems, which are being corrected. We only used half of the eight channel system, which may provide little control in some regions between coils. Furthermore, the B_1 maps measured in the experiments may have errors that can be propagated to the pulse design. The B_1 measurements in low magnitude regions may be unreliable, which is a common problem with BS B_1 mapping. Although we have verified off-line that the B_1 fields of the same phantom along the axial

114

direction were reasonably uniform by looking at the saggital view B_1 maps, the 3D B_1 maps used in the experiments that were replicas of 2D B_1 maps might still have some variations along axial direction. This can also cause pulse design errors. Since the single-channel excitation experiments did not compensate for B_1 inhomogeneity, the parallel excitation 4D fat sat pulse may still be advantages in the applications where B_1 inhomogeneity is more problematic, e.g., fat sat in abdominal imaging at 3T [74].

The 4D fat sat pulse improves fat sat performance at the cost of a more complex experimental procedure. The 4D fat sat pulse requires B_0 mapping and possibly B_1 mapping. These increase the total study time, and the effectiveness of the fat sat pulse is more likely to be affected by subject motions. Thus, it is important to use fast methods for acquiring and processing the B_0 and B_1 scans [133] [1].

Investigation of the proposed method at different main field strengths could be an interesting future work. At lower field where the pulse length of the conventional fat sat is more problematic, the 4D fat sat pulse could be even more advantageous, because sparser sampling along k_f at lower field allows the 4D fat sat pulse to better compensate for spatial variations which is smaller than at 3T, so that the task in the spectral domain can be simplified even more; in other words, the 4D fat sat pulse length may be shortened further at lower field. In addition, SAR is less of a concern at lower field strength. On the other hand, it will be more challenging to design 4D fat sat pulses at fields higher than 3T where B_0 and B_1 inhomogeneity is more severe. In such designs, the required shorter sampling interval along k_f leaves smaller room for the pulse to compensate for the even larger spatial variations, and parallel excitation will probably be required. Since the pulse length of the conventional fat sat is less of an issue at high field, the proposed method will mainly help to compensate for the field inhomogeneities rather than to shorten the pulse length. We have done some simulation studies on 7T 4D fat sat pulse design which showed some promising

results, but SAR may be more problematic.

4.6 Conclusions

We proposed an efficient 4D SPSP fat sat pulse that uniformly suppresses fat without exciting water in the presence of B_0 and B_1 inhomogeneity with single channel or parallel excitation system. In the 3T experiments, the proposed method showed superior performance in terms of fat suppression and pulse length compared to the SLR fat sat pulse. In particular, the proposed pulse was only half of the standard fat sat pulse in the single-channel excitation experiments. We also found that the SPINS trajectory is generally preferred to spoke trajectory in single-channel excitation, but the choice of trajectory in parallel excitation depends on specific situations. This approach must be very useful in a variety of applications at different field strengths.
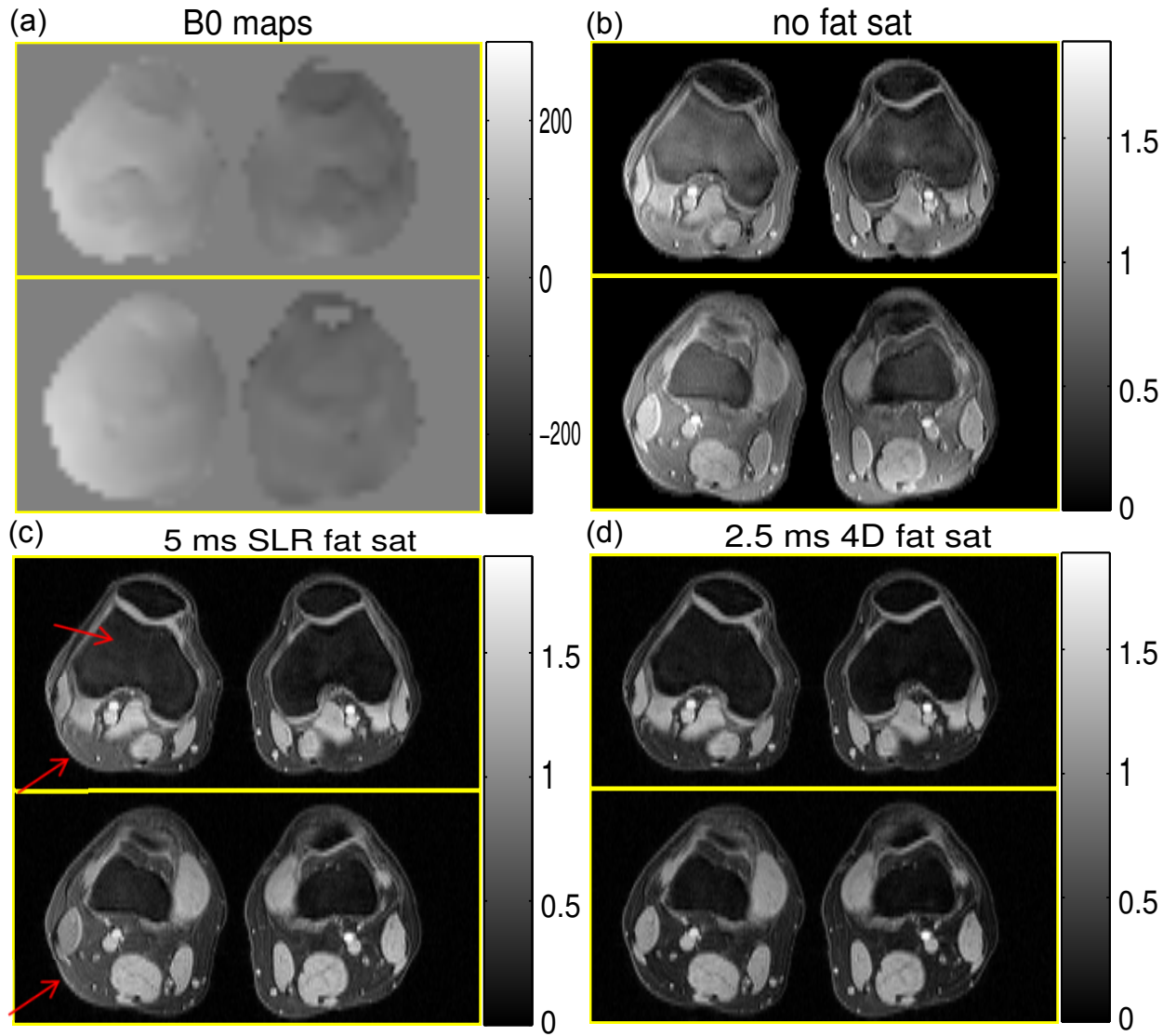
Figure 4.4.5: The B_0 maps and results of the knee imaging, where two representative axial slices are shown. (a) The B_0 maps (in Hz). (b) The images without fat sat. (c) The images with 5 ms SLR fat sat pulse. (d) The images with 2.5 ms 4D fat sat pulse.

CHAPTER V

Simultaneous Fat Saturation and Magnetization Transfer Contrast Imaging with Steady-State Incoherent Sequences[1]

5.1 Introduction

Fat suppression has been commonly used in many MRI applications to suppress undesired adipose tissue signals or prevent chemical shift artifacts. Fat sat(uration) is one of the most popular fat suppression techniques, which uses a spectrally selective pulse to selectively saturate and dephase fat spins preceding the actual imaging pulse sequence [28]. Fat sat typically works well and is compatible with most imaging sequences, but it is sensitive to B_0 and B_1 inhomogeneity. Moreover, the fat sat pulse is long in low field scanners, which limits the minimum T_R for some fast MRI sequences. These problems have been mitigated in [33], where a 4D tailored spectral-spatial (SPSP) fat sat pulse is demonstrated to be robust to B_0/B_1 inhomogeneity and shorter than the standard fat sat pulse by half on 3T scanners.

Another technique that can modify magnetization of tissue in MRI is called "magnetization transfer contrast (MTC) imaging". This technique utilizes the tissue-dependent magnetization transfer (MT) effect which features signal attenuation caused

---

[1]This chapter is based on [95, 96]

118

by the interaction between free hydrogen protons, e.g., those of fluid, and restricted hydrogen protons , e.g. those of macro-molecules [86]. Specifically, the restricted protons, which have much broader spectra, can be saturated by off-resonance pulses and then exchange magnetization with the free protons. Using this tissue-dependent feature, MTC sequences can produce MTC images with useful diagnostic information. MTC imaging can be conducted either only once before a steady-state imaging sequence [72] (turbo MT prep) or in each repetition [87] like the fat sat sequence; in this work, we will focus on the latter, which will be shown to have higher MT sensitivity and thus less specific absorption rate (SAR) penalty when T_R is short.

It has been shown that combining fat sat and MTC are beneficial in many clinical applications, such as cartilage imaging [87] [73], cardiac imaging [72], intracranial angiography [89], breast imaging [90] and lung imaging [134]. In the angiography applications, spoiled gradient-echo sequence (SPGR) has been widely used to produce T_1-weighted or flow-enhanced images with very short imaging time, e.g., time-of-flight (TOF) angiography [72]. SPGR belongs to the class of "steady-state incoherent (SSI) sequences" which eliminate any residual transverse magnetization prior to each RF pulse [6]. SSI sequences are usually compatible with fat sat and MT pulses applied in each repetition. In applications that need more T_2 weighting, e.g., MTC cartilage imaging, balanced steady-state free precession sequence (bSSFP) is one of the preferred sequences, as this fast imaging sequence can produce T_2/T_1 contrast images that have higher signal-to-noise ratio (SNR) than SPGR images. However, a drawback of bSSFP is the banding artifacts caused by B_0 field inhomogeneity; and it belongs to "steady-state coherent (SSC) sequences" [6] which have limited compatibility with fat sat and MT pulses in each repetition. Nielsen *et al.* [2] have proposed an SSI sequence called "small-tip fast recovery sequence (STFR)". It produces bSSFP-like T_2/T_1 contrast images which have higher SNR than SPGR images, but they are free of banding artifacts.

119

Although SSI sequences like SPGR or STFR are compatible with fat sat and MT pulses in each repetition, some limitations may hamper their practical use. Combining both fat sat and MT pulse into one sequence may largely increase minimal T_R which may make it impractical in applications like breath-hold imaging, especially in low field scanners. In higher field scanners, SAR penalty may be of a concern when fat sat and MT pulses are both incorporated into the sequence.

In this work, we propose to combine the multi-dimensional tailored SPSP fat sat (MD fat sat) pulse proposed in Chapter IV to SSI sequences including SPGR and STFR. We found that the short-T_R SSI sequences with this efficient MD fat sat pulse can suppress fat and produce MT effect simultaneously. With only the MD fat sat pulse (with gradient crusher), which is even much shorter than the standard spectrally selective fat sat pulse, the proposed sequences have less limitation on the minimal T_R and potentially lower the overall SAR. In addition, the MD fat sat pulse is also robust to B_0/B_1 inhomogeneity, which mitigates the general problem in fat sat imaging. Furthermore, we found that the conventional RF spoiling scheme that is typically used for SPGR and STFR does not work when RF pulses with crushers like fat sat is applied, so we introduce a modified RF spoiling scheme is for the proposed sequences.

In this work, we demonstrate the proposed methods on 3T scanners. In addition to several simulation studies and phantom experiments, we applied the proposed sequences on human brain imaging, cartilage imaging and TOF-based MR angiography in brain.
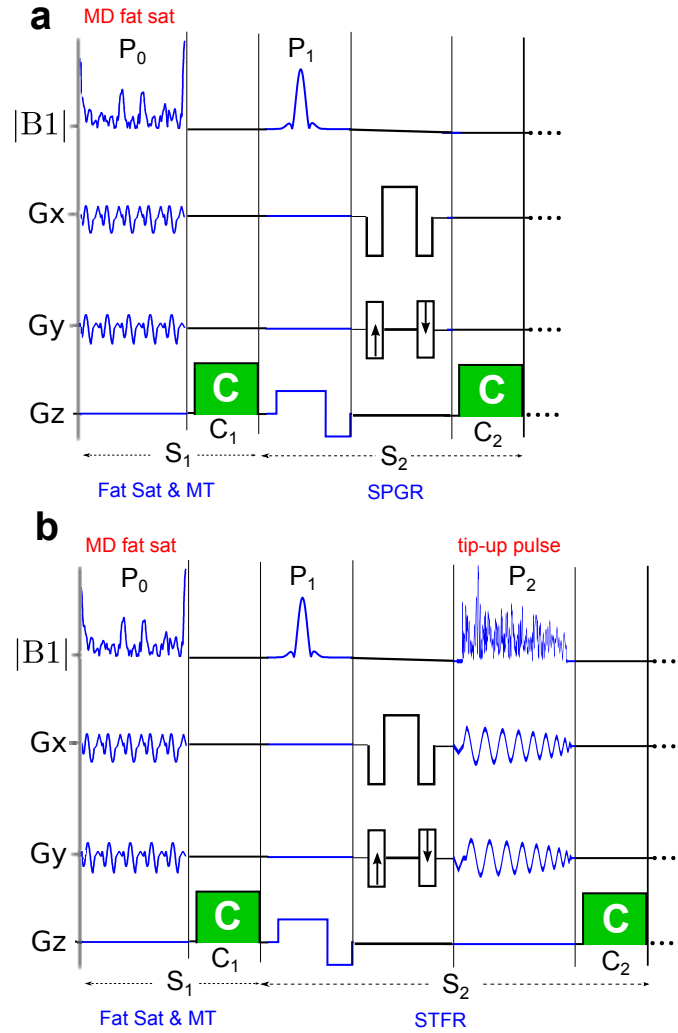
Figure 5.2.1: The illustrative diagram of the 2D version of the proposed pulse sequences. a: FSMT-SPGR; b: FSMT-STFR.

5.2 Theory

5.2.1 Steady-state Incoherent Sequences with Fat Sat

Fig. 5.2.1 illustrates the 2D version of the proposed fat sat and MTC SPGR (FSMT-SPGR) and fat sat and MTC STFR (FSMT-STFR). In FSMT-SPGR, the fat sat and MT part (S_1) with the MD fat sat (P_0) is added prior to the regular excitation pulse (P_1) of SPGR (S_2) in each repetition, and both S_1 and S_2 have a gradient crusher, i.e., C_1 & C_2. This 2D version of FSMT-SPGR uses a 3D SPSP fat

sat pulse [96] [95] which is tailored to the B_0/B_1 field using the same method proposed in Chapter IV, and the only difference is that repeated 2D spiral-out trajectories are used to cover the 3D SPSP k-space. The 3D version of the FSMT-SPGR uses the same 4D fat sat pulse used in Chapter IV. Compared to SPGR, the main difference of the 2D STFR is the 2D tailored tip-up pulse (P_2) at the end of each repetition which is tailored to tip up the excited spins back to the longitudinal axis according to local off-resonance frequencies [2]. By adding to the tip-up pulse to recycle spins, STFR can produce high SNR T_2/T_1 contrast images. Another difference of STFR from SPGR is that its net gradient areas between the tip-down excitation and the tip-up pulse have to be zero, so that the spin behaviors are more controllable by the tip-up pulse.

Both the regular SPGR and STFR without fat sat need gradient crushers to spoil the residual transverse magnetization before the next imaging cycle, and RF spoiling is also required when $T_R < T_2$ [83] [2]. RF spoiling removes the residual transverse signal by quadratically varying the global RF phase, which produces incoherent intra-voxel spin behaviors. In SPGR without fat sat, the global phase of P_1 varies as the following quadratic function:

$$\Phi_{P_1}(n) = \frac{a}{2}n^2 + bn + c \qquad (5.2.1)$$

where a, b, c are constants, and n is the number of repetitions. The quadratically changing phase guarantees that the signal of all the voxels reach a homogeneous steady-state, and the residual signal at the end of each repetition can be kept to almost zero by choosing a particular value of a, e.g., 117^0. For the STFR without fat sat, as the net gradient areas in between P_1 and P_2 are zero, the whole part that contains P_1 and P_2 can be treated as a single pulse from the RF spoiling's point of view. Thus, STFR works with the same RF spoiling as SPGR when P_2 keeps the

same global RF phase as P_1 [2].

However, the SSI sequences with additional crushers in each repetition, e.g., fat sat sequences, may not work robustly with the conventional RF spoiling scheme, i.e., P_0 keeps the same global phase as P_1 (and P_2). For SPGR with fat sat, this RF spoiling scheme only guarantees the signals to reach steady state with perfect fat sat where water/fat only experiences one RF pulse, i.e., P_1/P_0, in each repetition, which rarely happens in practice. When using the conventional fat sat, even if the B_0 inhomogeneity is not severe enough to have water excited by the fat sat pulse, fat signals can never be perfectly eliminated in the presence of B_0/B_1 inhomogeneity; then fat spins can be excited both by P_0 and P_1, and the additional crusher C_1 will alter the signal's progression to steady state. Similarly, STFR with fat sat is only guaranteed to reach steady state with perfect fat sat and T_1 relaxation of fat between P_0 and P_2 ignored. Although the MD fat sat pulse can largely reduce imperfect fat sat in the presence of B_0/B_1 inhomogeneity, it is still not guaranteed to work perfectly in all the cases. Furthermore, in the case that P_2 and the MD fat sat pulse are not designed for the whole object, the uncontrolled out-of-slice/slab parts of the object can also produce non-steady-state signals [96]. Therefore, to improve the robustness of the SSI sequences with fat sat, we propose to modify the conventional RF spoiling scheme to guarantee steady state reaching with imperfect fat sat. The new RF spoiling scheme is to apply the quadratic RF phase variation to each "sub-unit that contains a crusher" instead of each repetition. The functions of the global phase of each pulse in SPGR with fat sat then becomes:

$$
\begin{aligned}
\Phi_{P_0}(n) &= \frac{a}{2}(2n - 1)^2 + b(2n - 1) + c \\
\Phi_{P_1}(n) &= \frac{a}{2}(2n)^2 + b(2n) + c
\end{aligned}
\tag{5.2.2}
$$

If the two crushers C_1 and C_2 have the same area, this modified RF spoiling will guarantee the sequence to reach steady state. Keeping the global phase of P_2 the

same as P_1, STFR with fat sat works similarly with the modified RF spoiling scheme.

5.2.2   Simultaneous Fat Sat and MTC Imaging
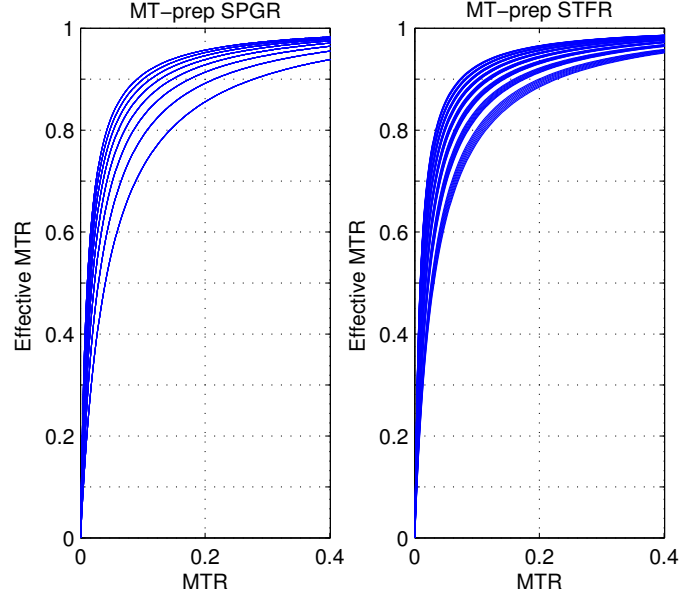
Figure 5.2.2: The plot of the effective MTR in terms of MTR for MTC SSI sequences; $0.5 \text{ s} \leqslant T_1 \leqslant 2 \text{ s}$, $50 \text{ ms} \leqslant T_2 \leqslant 200 \text{ ms}$. It shows that both sequences are sensitive to small magnetization attenuation caused by MT effect.

It is mentioned in the introduction that MT pulse applied in each repetition of SSI sequences produces higher MT effects than the turbo type MT prep which is applied once before a train of repetitions. Suppose MT ratio (MTR) is defined as the ratio between the reduced magnetization caused by MT and the original magnetization, and then the steady-state longitudinal magnetization of MTC SPGR prior to each P_1 with respect to MTR is:

$$M_z(r) = M_0 \frac{(1-r)E_{1s}(1-E_{1d}) + (1-E_{1s})}{1-(1-r)E_{1s}E_{1d}\cos\alpha} \tag{5.2.3}$$

where r is MTR, M_0 is equilibrium magnetization, $E_{1s} \triangleq e^{-\frac{T_s}{T_1}}$, $E_1 \triangleq e^{-\frac{T_d}{T_1}}$, T_s is the duration of each gradient crusher, T_d is the duration of each repetition excluding

the MT part, α is the flip angle, relaxation during the MT pulse is ignored. The corresponding function of MTC STFR with respect to MTR is:

$$M_z(r) = M_0 \frac{[(1-r)E_{1s}^2(1-E_{1f})\cos\alpha + (1+(1-r)E_{1s})(1-E_{1s})]}{1-(1-r)E_{1s}^2(E_{2f}\sin^2\alpha - E_{1f}\cos^2\alpha)} \qquad (5.2.4)$$

where $E_{1f} \triangleq e^{-\frac{T_f}{T_1}}$, $E_{2f} \triangleq e^{-\frac{T_f}{T_2}}$, T_f is the duration between the peak of P_1 and the beginning of P_2, and relaxation during tip-up and MT pulse is ignored.

To show that such MTC SSI sequences are more sensitive to MT effect than the turbo MT-prep sequences, we plot sets of curves of $1 - M_z(r)/M_z(0)$ for ranges of T_1 and T_2 values in Fig. 5.2.2, where $1 - M_z(r)/M_z(0)$ is the "effective MTR" of SSI sequences and it corresponds to the MTR measured from images. The sequence parameters were set as follows: $T_d = 10ms$, $T_s = 1ms$ and $T_f = 8ms$. Note that MTR is equal to the effective MTR of the turbo MT prep sequences, so the plots show that with reasonable T_1 and T_2 values, MTC SSI sequences with MT pulses applied in each repetition are much more sensitive to MT effect than the corresponding turbo MT prep sequences. Such MT sensitivity increases with shorter T_R or longer T_1 and does not change much with different T_2 values.

With this property, we propose to use SSI sequences with MD fat sat to generate MT effect and suppress fat simultaneously. In fact, despite that such sequences are MT sensitive, SSI sequences with the conventional spectrally selective fat sat pulse can not produce enough MT effect for clinical use, as the conventional fat sat pulses are low energy pulses compared to typical MT pulses and MT effects is proportional to RF energy. However, the proposed MD fat sat produces much higher RF energy than the conventional fat sat pulse, because this short efficient tailored SPSP pulse needs to handle both spectral and spatial variations by traversing the excitation k-space very rapidly, which leads to higher RF amplitude and thus higher RF energy. In addition, the MD fat sat is about 3.5 ppm off the center frequency which is much lower than

the off-resonance frequency of the conventional MT pulses. This can further increase the MT effects induced by the MD fat sat as MT effects decrease with off-resonance frequency. Thus, we think that the proposed MD fat sat can potentially produce non-trivial MT effects while suppressing fat signal.

5.3 Methods

5.3.1 Simulation and Phantom Experiment I: RF Spoiling Schemes

We first compare the conventional RF spoiling scheme and the adapted RF spoiling scheme by Bloch equation simulations. We simulated the signal evolutions of the integrated magnetization of a 0.5 cm voxel with 5000 isochromats for fat or water with fat-sat SPGR or fat-sat STFR. We chose some typical values for the fat spin and the water spin: $T_{1,fat}/T_{2,fat} = 200$ ms/70 ms, $T_{1,water}/T_{2,water} = 1$ s/100 ms; the sequence parameters were: $T_R = 10$ ms, the tip angle of P_1 (and P_2) was 20^0 for both water and fat, the tip angle of P_0 was 80^0 for fat and 20^0 for water to simulate imperfect fat sat, and the parameter a in (5.2.1) and (5.2.2) was 117^0. We simulated evolutions of the transverse magnetization of fat and water right after P_1 for the first 200 and 500 repetitions (2 s and 5 s) respectively, which are long enough to test steady state reaching.

In addition, we also applied fat-sat SPGR in a phantom scan on a 3T GE scanner (GE Healthcare, Milwaukee, WI, USA). The phantom was a cylindrical phantom filled with distilled water and vegetable oil. The fat sat part used a conventional spectrally selective fat sat pulse designed by the Shinnar-Le Roux (SLR) algorithm [18]. The SLR fat sat pulse is 5 ms long and has a 400 Hz minimal phase passband for fat (center frequency is -435 Hz), which is typically a standard setting for 3T fat sat. With this fat sat pulse, a 3D SPGR with spin-warp readout was applied using the conventional and the adapted RF spoiling schemes respectively, and the imaging parameters were:

$T_R = 13$ ms, FOV = 14 cm $\times$14 cm $\times$14 cm, data size = $64 \times 64 \times 14$, $a = 117^0$. A set of images without fat sat was also acquired for reference.

5.3.2 Phantom Experiment II: Fat Sat Pulses

The 4D SPSP fat sat pulse which is used for 3D or multi-slice imaging has been demonstrated in Chapter IV. In our experiments with fat-sat SSI sequences, we also carried out 2D scans which only need 3D version of the MD fat sat pulse. We carried out some phantom experiments on the 3T GE scanner to test 2D SSI sequences with 3D SPSP fat sat. The phantom was the same cylindrical water/oil phantom used in the previous experiment. Similar to Chapter IV, we designed each 3D fat sat pulse only based on a 2D B_0 field map, assuming that B_1 inhomogeneity is acceptable in our single channel excitation experiments. These 3D fat sat pulses were compared with the 5 ms SLR fat sat pulse used in the previous experiment. The goal of this study is to demonstrate that SSI sequences with 3D fat sat pulse are more robust to B_0 inhomogeneity than the ones with the SLR fat sat pulse.

We carried out two experiments to test fat-sat SPGR and fat-sat STFR respectively. In each experiment, the fat sat sequence was applied to different slices of the phantom to acquire multiple 2D axial slice images, where each 3D fat sat pulse was designed to the corresponding 2D B_0 map; for STFR sequence, the 2D tailored tip-up pulse (P_2) was also designed individually for each slice. We acquired B_0 maps from two gradient echo images with different echo times, and the echo time difference needs to have water and fat spins in-phase, e.g., $\Delta T_E = 2.272$ ms at 3T, to eliminate the phase difference caused by chemical shift. All the 3D fat sat pulses, which were only 2.1 ms long, use 5 repetitions of 2D spiral-out excitation k-space trajectories, and the adapted RF spoiling scheme was applied to the fat sat sequences. All the data were acquired with 2D spin-warp k-space trajectories, and the imaging parameters of fat-sat SPGR were: FOV = 14 cm $\times$14 cm, slice thickness = 6 mm, data size = 64×64,

$a = 117^0$, and $T_R = 11.6$ ms and 14.5 ms for the sequence with the 2.1 ms 3D fat sat pulse and the 5 ms SLR fat sat pulse respectively. The imaging parameters of the fat-sat STFR experiments were the same except that T_R were 4.9 ms longer than the corresponding SPGR sequences respectively. For each fat suppressed image, we also acquired its corresponding non-fat-suppressed image with the fat sat pulse turned off in the sequence.

5.3.3 Phantom Experiment III: Simultaneous Fat Sat and MTC Imaging

To test MT effects, we made a special cylindrical MT phantom that is filled with mixture of Prolipid 161 (Ashland Specialty Ingredients) and $NiCl_2$ solution. The material has similar T_1, T_2 and MT values to white matter at 3T. In addition, we made a spherical phantom that is filled with mineral oil and distilled water doped with $MnCl_2$, and the $MnCl_2$ solution was carefully tuned to match the T_1 and T_2 values of the MT phantom material at 3T. To test the effect of simultaneous fat sat and MTC, we put both phantoms in one field of view and applied the proposed FSMT-SPGR and FSMT-STFR respectively on the 3T scanner. Similar to the previous phantom experiment, we first acquired a 2D B_0 map, and then designed 3D SPSP fat sat pulse and the tailored tip-up pulse based on the field map. FOV of the field map used in the design was 18 cm ×18 cm, and the pulse length was increased to 2.7 ms with 7 repetitions of spiral-out trajectories to accommodate the B_0 field that has big variations between the two phantoms (Fig. 5.4.4). With the designed pulses, the FSMT-SPGR and FSMT-STFR with 2D spin-warp readout were applied respectively to the same part of the object with the FSMT part on or off, and the imaging parameters were: FOV = 18 cm ×18 cm, slice thickness = 6 mm, data size = 64×64, $a = 117^0$, and $T_R = 16$ ms for both SPGR and STFR.

5.3.4 In-Vivo Experiments I: Simultaneous Fat Sat and MTC Imaging in Brain

Furthermore, we tested the proposed FSMT-SPGR and FSMT-STFR sequences in two *in-vivo* experiments respectively on the 3T GE scanner, where we scanned axial brain slices of healthy subjects. Similar to the phantom experiments, 2D B_0 maps were first acquired for the 3D SPSP fat sat pulse design and the tailored tip-up pulse of the STFR sequence. For both the SPGR and STFR experiments, the 3D fat sat pulse was 2.3 ms long with 7 repetitions of 2D spiral-out trajectories. In each experiment, the SSI sequence with 2D spin-warp readout was applied to acquire 2D brain images when the designed FSMT part was on or off respectively. The imaging parameters for the SPGR experiment were: FOV= 24 cm $\times$24 cm, slice thickness = 6 mm, data size = 256×256, $a = 117^0$, and $T_R = 15.3$ ms. The SPGR sequence imaged an axial slice around the level of eyes, while the STFR experiment imaged a more superior axial brain slice. The imaging parameters of the STFR sequence were the same as the SPGR sequence except that T_R was 19.1 ms.

5.3.5 In-Vivo Experiments II: Cartilage Imaging

We then investigated the proposed sequence in the application of cartilage imaging where contrast between synovial fluid and cartilage is desired. Fat suppression is generally beneficial to this application because it can eliminate the surrounding fat that would obscure the tissue of interest [135] [136]. MTC is useful for T_2 weighted [137] or T_2/T_1 weighted cartilage imaging [135], where synovial fluid appears brighter than cartilage, so MT can enhance the fluid-cartilage contrast by attenuating cartilage signals.

Therefore, we applied the proposed FSMT-STFR which produces T_2/T_1-like contrast [2] to cartilage imaging in human knees. 2D STFR with 3D fat sat is designed for an axial slice based on a 2D B_0 map acquired with SPGR sequences, and the

image data were acquired with 2D spin-warp readout. The 3D fat sat pulse was 2.1 ms long using 7 repetitions of spiral-out trajectories. One additional image was taken with the 3D fat sat pulse off as the reference. Other imaging parameters are: slice thickness = 6 mm, T_R is 18.5 ms, flip angle = 16^0, $a = 117^0$, 1.09 mm$\times$1.09 mm resolution, FOV = 28 cm $\times$14 cm.

5.3.6   In-Vivo Experiments III: MR Angiography in Brain

Furthermore, we applied the proposed FSMT-SPGR to MR angiography (MRA) in human cerebral arteries where fat suppression and MT can help suppressing surrounding fat and other background tissue respectively. We acquired 3D time-of-flight (TOF) images at a 4 cm thick axial slab around the circle of Willis with a 3D SPGR sequence. In addition, 4D fat sat pulse was designed based on the 3D B_0 map of an extended 3D axial slab that covered the imaging slab and its adjacent inferior axial slab (4 cm thick). By designing for this extended volume, direct excitation of the arterial blood in the upstream region by the 4D fat sat pulse can be largely reduced, because 4D fat sat pulse has unpredictable effects to out-of-ROI regions. The 4D fat sat pulse was 2.5 ms long using a repeated 3D spiral trajectory [128]. The image data were acquired with 3D spin-warp readout, and two sets of images were taken with the FSMT part on or off respectively. The imaging parameters are: $T_E = 3.28$ ms, $T_R = 11.4$ ms, flip angle = 20^0, $a = 117^0$, 0.94 mm$\times$0.94 mm$\times$2 mm resolution, FOV = 24 cm $\times$24 cm $\times$4 cm.

5.4   Results

5.4.1   Simulation and Phantom Experiment I: RF Spoiling Schemes

Fig. 5.4.1 shows the signal evolutions of fat or water when fat-sat SPGR or fat-sat STFR is applied with the conventional RF spoiling scheme or the adapted RF
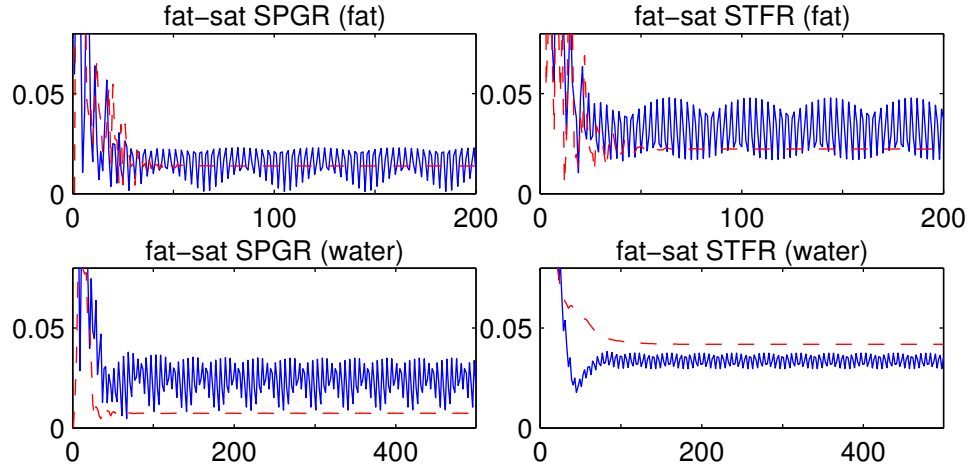
Figure 5.4.1: Signal evolutions of fat spin (upper row) and water spin (lower row) using fat-sat SPGR (left column) and fat-sat STFR (right column) with different RF spoiling schemes. Every longitudinal axis denotes the ratio between the transverse magnetization right after P_1 and the magnetization at equilibrium, M_{xy}/M_0; every horizontal axis denotes the number of repetitions. The signal can reach steady state with the adapted RF spoiling scheme (dashed lines), but can not with the conventional RF spoiling scheme (solid lines).

spoiling scheme. In all the four plots, the sequence with the conventional RF spoiling scheme can not reach steady state (blue solid lines), but the one with the adapted RF spoiling scheme reaches steady state after 100 repetitions at most (red dashed lines). With the signal oscillating over repetitions, the data of the conventional RF spoiling scheme are inconsistent in the k-space, which causes ghosting artifacts. This is shown in Fig. 5.4.2 where the image acquired with the conventional RF spoiling scheme has ghosting artifacts along the phase-encoding direction of the spin-warp trajectory, while the one with the adapted RF spoiling scheme shows a fat-suppressed image free of ghosting artifacts.

5.4.2 Phantom Experiment II: Fat Sat Pulses

Fig. 5.4.3 shows the resulting images produced by fat-sat SPGR and fat-sat STFR as well as the corresponding B_0 maps. Specifically, the original images without fat sat
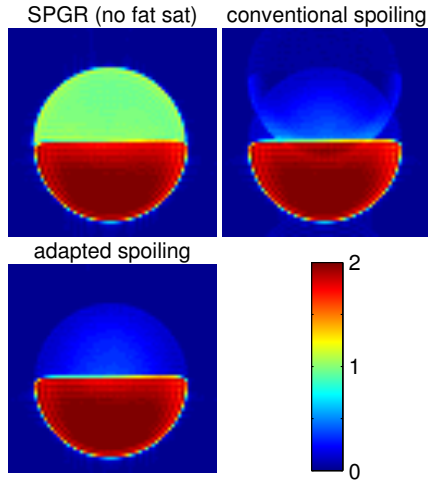
Figure 5.4.2: An axial slice of the 3D SPGR images of the cylindrical phantom (oil on top of water) where all three images are at the same color scale: upper-left: SPGR with fat sat off; upper-right: SPGR with fat sat on, conventional RF spoiling; lower-left: SPGR with fat sat on, adapted RF spoiling. The image with the conventional RF spoiling has ghosting artifacts due to data inconsistency, and the one with the adapted spoiling scheme is free of these artifacts.

are in the first column, the B_0 maps are in the second column, and the ratio images by the 3D fat sat and the SLR fat sat are shown in the third and fourth columns respectively. The ratio image is calculated by taking the ratio between the image with fat sat and the corresponding image without fat sat, so it should range from 0 to 1 in theory. The first two rows show the results by SPGR sequences and the STFR results are shown in the last two rows.

As seen in the B_0 maps, we picked two slices of the phantom that have relatively extreme off-resonance frequencies to demonstrate the principle. The original images by SPGR are uniform in both oil (top) and water (bottom) parts, but STFR images are not as uniform in oil parts, because the tailored tip-up pulses were only designed for water and have off-resonance effects on fat, which makes fat suppression more important in STFR imaging. As seen in the last column in Fig. 5.4.3, SLR fat sat did not suppress fat signal completely in regions with large off-resonance frequencies. In addition, comparing the two STFR results in the last column, SLR fat sat worked
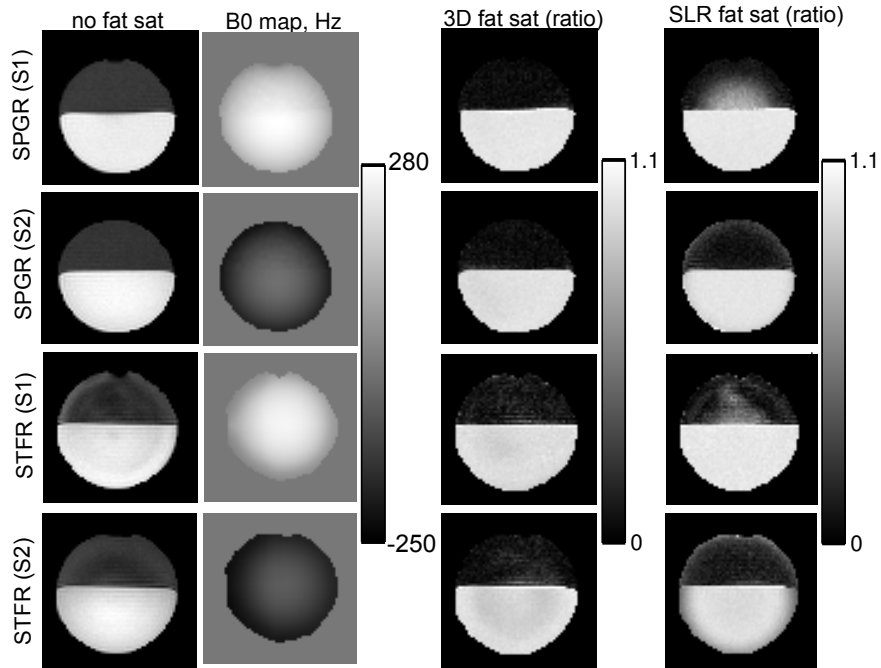
Figure 5.4.3: The results of the phantom experiments for testing fat-sat SPGR and fat-sat STFR where we picked two representative slices for each sequence. From left to right, 1st column: the original images with no fat sat (oil on top of water), 2nd column: B_0 maps, 3rd column: the ratio images with the 3D fat sat pulse, 4th column: the ratio images with the SLR fat sat pulse. The top 2 rows: SPGR results; the bottom 2 rows: STFR results. The ratio image is calculated by taking the ratio between the image with fat sat and the corresponding image without fat sat.

generally well for water parts, except for the edges where off-resonance frequencies are negative (last row), which is because the frequency response of the SLR pulse is asymmetric around the center frequency of water. However, although the B_0 maps of the SPGR experiments are similar to those of the STFR experiments respectively, SPGR with SLR fat sat worked well for water in both slices, which shows that the fat-sat SPGR sequence with these particular parameters and object materials is less sensitive to water selection from fat sat pulse than the fat-sat STFR used in this experiment. In contrast, the SSI sequences with 3D fat sat worked quite robustly for both water and fat in the presence of B_0 inhomogeneities. In addition, the 3D fat sat

133

pulse is 58% shorter than the SLR fat sat pulse.

5.4.3 Phantom Experiment III: Simultaneous Fat Sat and MTC Imaging
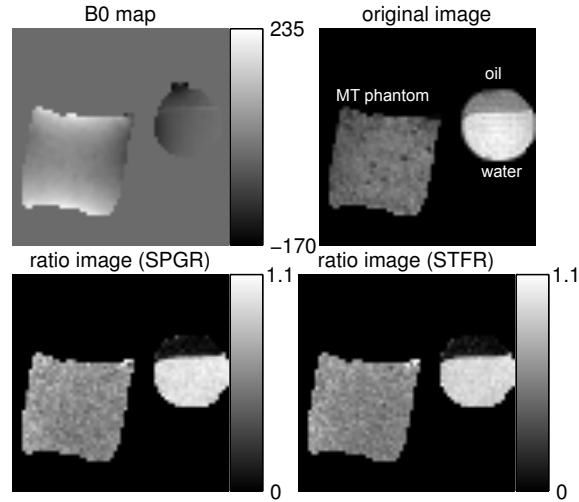
Figure 5.4.4: The B_0 map and the resulting images of Phantom experiment III. Upper-left: B_0 map; upper-right: the original SPGR image with FSMT part off where oil, water and the MT phantom are labeled; lower-left: the ratio image of SPGR taken between the one with FSMT contrast and the one without; lower-right: the ratio image of STFR. These two sequences show similar performance on suppressing fat and producing MTC.

Fig. 5.4.4 shows the B_0 map and the corresponding ratio images produced by FSMT-SPGR (lower left) and FSMT-STFR (lower right), and the ratio images are taken between the images with FSMT contrast and the corresponding images without FSMT contrast. Both sequences simultaneously suppress fat and attenuate the MT phantom while the water signal is still kept at the similar level. By manually segmenting each image into the three parts, we calculated the average ratios of these three materials, which are summarized in Table 5.1. In general, FSMT-SPGR and FSMT-STFR worked similarly in terms of fat suppression, MT effect and water selection, and FSMT-SPGR suppresses fat a little more effectively and attenuates water and MT phantom slightly less than FSMT-STFR. It is true that there may be some

direct excitation of the fat sat pulse to the MT phantom that can contribute to the attenuation in the MT phantom regions, and this effect is hard to be separate from MT effect. However, according to the simulations of the pulses (not shown), direct excitation in the MT phantom regions was very similar to direction excitation in the water regions. Since we do not observe much direction excitation in the water regions, we believe the attenuation in the MT phantom regions is mainly caused by MT effect of the fat sat pulse.

Table 5.1: Average Signal Ratios of the Different Materials

	oil	water	MT phantom
FSMT-SPGR	0.076	0.970	0.621
FSMT-STFR	0.086	0.924	0.610

5.4.4 In-Vivo Experiments I: Simultaneous Fat Sat and MTC Imaging in Brain

The brain imaging results are shown in Fig. 5.4.5, where the SPGR images are at the top and the STFR images are at the bottom. Both sequences effectively suppress the fat tissue around skulls and optical nerves (top row). In addition, white matter is largely attenuated by both sequences due to MT effect. With the particular settings in this experiment, FSMT-STFR shows larger MT effects than FSMT-SPGR; specifically, white matter signal attenuation in the SPGR image is 30% - 50% while FSMT-STFR reduced white matter signal by 50% - 70%.

5.4.5 In-Vivo Experiments II: Cartilage Imaging

Fig. 5.4.6 shows the cartilage imaging results comparing the image with no FSMT contrast (middle) to the one with FSMT contrast by the 3D fat sat pulse (bottom), and the corresponding B_0 map is shown at the top. Fat suppression removed the fat tissue surrounding the cartilage and joint fluid areas and also helped removing the

135
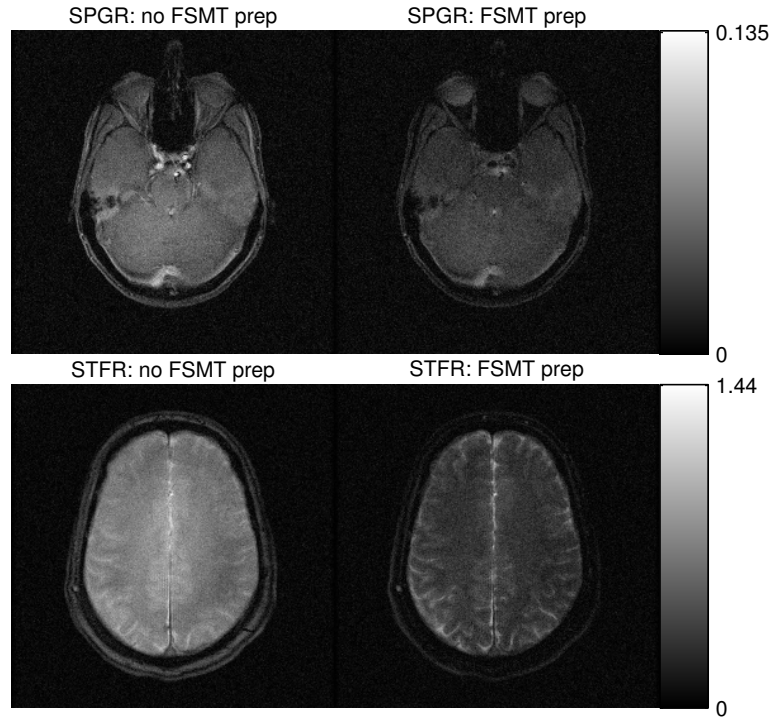
Figure 5.4.5: The images acquired in the *in-vivo* experiments on human brain. Upper row: the SPGR experiment result; lower row: the STFR experiment result. Left column: the images without FSMT contrast; right column: the images with FSMT contrast. Images in the same row are in the same gray scale.

posterior fat that has artifacts due to the tailored tip-up pulse of STFR. In particular, the 3D fat sat worked very well in the regions with large B_0 inhomogeneity, such as the posterior fat regions. In addition, MT effects suppressed cartilage and muscle signals, and thus highlighted the synovial fluid signals which are pointed out by the red arrows.

5.4.6 In-Vivo Experiments III: MR Angiography in Brain

Fig. 5.4.7 shows the results of the MRA experiment where the maximum intensity projections (MIP) of the image with no FSMT contrast (left) and the one with FSMT contrast (right) are shown. In the presence of B_0 inhomogeneity, the 4D fat sat largely suppressed the fat tissue around skull in the MIP with FSMT contrast, except that
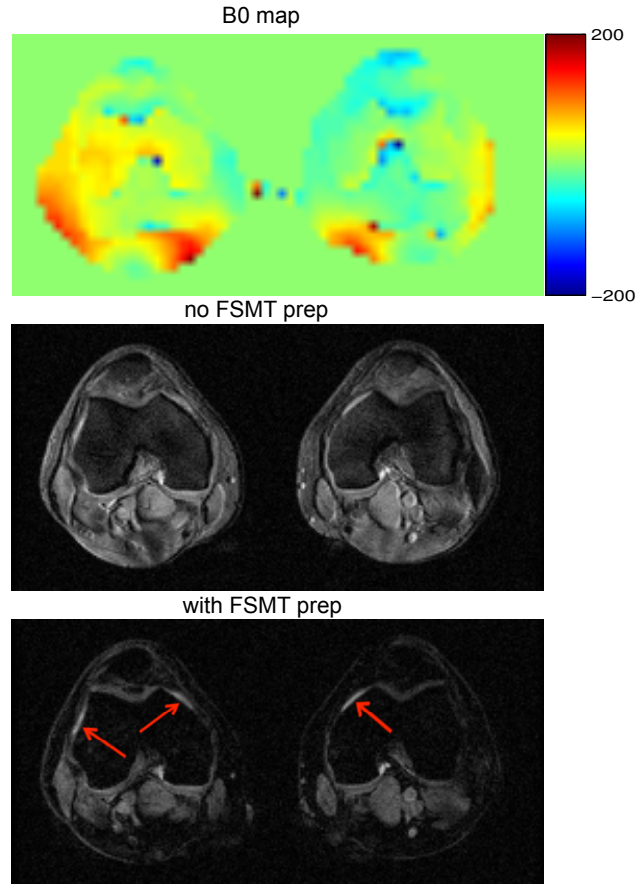
Figure 5.4.6: The resulting images of the cartilage imaging and the corresponding B_0 map (top). The image with no fat sat and MTC is at the middle, and the image with fat sat and MTC is at the bottom. These two images are in the same gray scale. The red arrows point to synovial fluid which is highlighted better in the image with simultaneous fat suppression and MTC.

part of fat around the left optical nerve is not suppressed well due to large off-resonance effect (about 300 Hz). Furthermore, MT effects produced by the 4D fat sat pulse largely reduced the background signals, and the arteries are better delineated in the MIP compared to the one without FSMT contrast, which is pointed out by the red arrows. Note that those two images are respectively normalized to their own maximal intensity, because the blood signal was also attenuated due to some direct excitation from the imperfect fat sat pulse, which is why the unsuppressed fat and optical nerve posterior to the left eye are bright in the FSMT contrast image. In
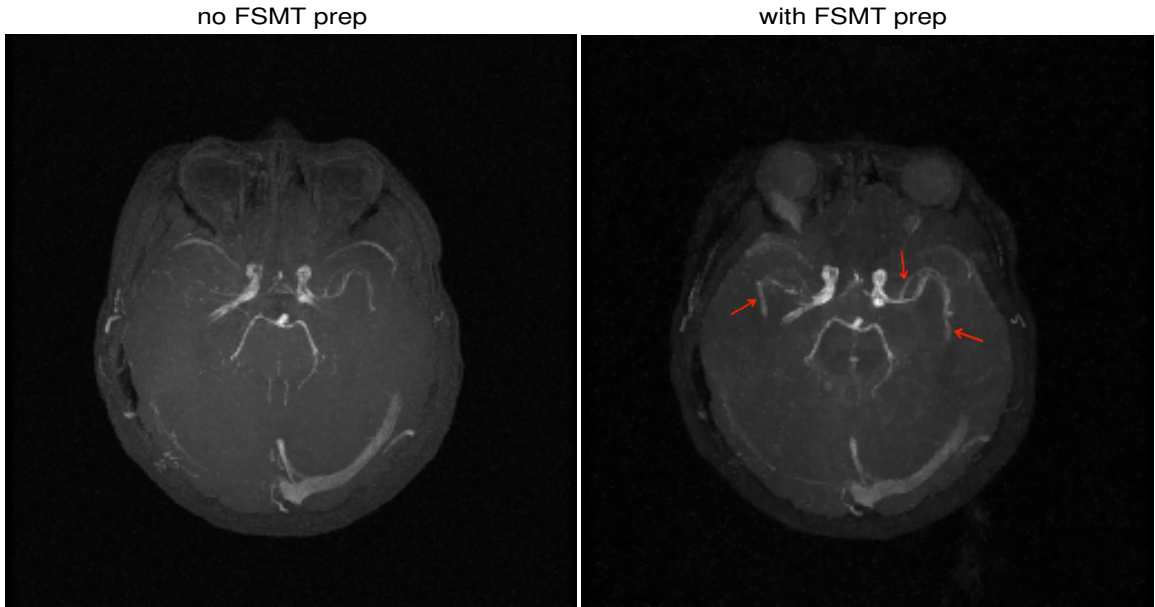
Figure 5.4.7: The results of the MRA experiments where the MIP with no FSMT contrast is on the left and the one with FSMT contrast is on the right. Red arrows point to the arteries that are better delineated due to MT effect and two of the fatty regions that are suppressed by the fat sat.

addition, some veins, especially the ones anterior to the circle of Willis, are darker in the FSMT contrast image, because the 4D fat sat pulse that was designed only for the imaging slab and the upstream region of the arteries may suppress the upstream regions of the veins. This may be a good feature that can reduce the need of vein suppression pulses. In general, the proposed FSMT-SPGR sequence improved the TOF MRA in the brain by simultaneously suppressing fat and background tissue.

5.5 Discussion and Conclusions

We proposed to apply the multi-dimensional SPSP fat sat pulse to SSI sequences, i.e., SPGR and STFR, to simultaneously do fat suppression and MTC. We demonstrated that an adapted RF spoiling scheme is required for fat-sat SSI sequences to reach steady state. Compared to the conventional SLR fat sat, the MD fat sat is more robust to field inhomogeneity, and it can additionally produce MTC with SSI

sequences having high sensitivity to magnetization attenuation. Examples of cartilage imaging and brain MRA show that the proposed FSMT-SSI sequences can produce images that appear to be better for clinical use.

For the adapted RF spoiling, the parameter a in [5.2.2] needs to be properly chosen to completely remove the remnant transverse magnetization at the end of each repetition. We empirically chose $a = 117^0$ for all our experiments based on simulations and some phantom experiments. There are also other good values for the fat-sat SSI sequences with the adapted RF spoiling, such as 74^0 for fat-sat SPGR and 76^0 for fat-sat STFR. For fat-sat SPGR imaging in particular, most spins only experience one crusher in each repetition when B_0 map is uniform, and then the sequence would almost work as the conventional RF spoiling but with 2 times linear phase increments. In this case, $a = 117^0/2$ may be a good choice.

We have shown that the proposed sequences are sensitive to magnetization attenuation induced by MT effect, which also means that these sequences are very sensitive to direction excitation of water by imperfect MD fat sat or SLR fat sat pulse in the presence of field inhomogeneity. We observed significant signal drop in MT-free materials with SLR pulse that has ripples in the water band smaller than 5% of the fat band amplitude, which is consistent to Fig. 5.2.2. Thus, the SLR fat sat pulse used in our experiments were designed with very strict restriction on the amplitude of ripples around water spectrum, and the MD fat sat design had to set high standards on fitting the target pattern of the water bands. In contrast, these sequences are not so sensitive to inaccurate fat suppression, so MD fat sat design sets very small penalty for inaccurate fat band fitting to accommodate the high demands in water bands.

B_1 inhomogeneity can be ignored in our 3T experiments, but there are cases where B_1 inhomogeneity can be a potential issue, e.g., breast imaging [138]. Then the MD fat sat can help to compensate for B_1 inhomogeneity or even use parallel excitation, which is another advantage over the conventional SLR fat sat. Although global SAR

was kept below the limit in our experiments, local SAR penalty may be problematic when parallel excitation is used. Moreover, MT effects by the parallel excitation version of the MD fat sat may need further investigation.

One advantage of SSI sequences over bSSFP for MTC imaging is that MTC SSI sequences can adjust the amplitude of MT effects more easily. The proposed sequences can also adjust MT effects by changing regularization parameter for RF power penalization. In our experiments, the RF energy of the MD fat sat pulse was able to be reduced by up to 5-10 times with acceptable penalty on fat suppression performance, which may have very minimal MT effects. Thus, the proposed sequences with RF power penalization can potentially be used for applications that only need fat suppression.

A drawback of the proposed sequences is that it is hard to separate the fat sat effect and the MT effect. Although we empirically demonstrated that the majority of the attenuation should be caused by MT effect, it is hard to precisely quantify the attenuation caused by MT effect only. In addition, it is also difficult to obtain the images with the fat sat effect only. Hence, this type of sequences are mainly used for generating MT contrast rather than quantitative MT studies.

This work shows the applications of the proposed sequences on cartilage imaging and MRA in brain at 3T. It would be interesting to investigate the proposed sequences in other clinical applications that can benefit from fat suppression and MTC, e.g., cardiac imaging and breast imaging. Furthermore, as Chapter IV has pointed out other potential benefits and issues of the MD fat sat pulse at other field strengths, future work may include studies of the proposed sequences at other field strengths.

CHAPTER VI

Balanced SSFP-like Imaging with Simultaneous Water-Fat Separation and Band Reduction using Small-tip Fast Recovery[1]

6.1 Introduction

Balanced SSFP provides high SNR efficiency and useful T_2/T_1 weighting, but it suffers from bright fat signal and off-resonance banding artifacts. Recently, a bSSFP-based method was proposed for simultaneously suppressing fat and banding artifacts from two phase-cycled acquisitions [81]. That method requires large tip angle excitation which may be undesirable in some applications, e.g., DESPOT2 [139], and leads to increased SAR. We propose to use an alternative steady state imaging sequence, referred to as Small-Tip Fast Recovery imaging (STFR) [2], to do water-fat separation and suppress banding artifacts, which works well for flip angles ranging from 16^0 to 90^0. Specifically, this method is based on the gradient crusher based STFR (G-STFR) [85] that is equivalent to the chimera SSFP [140]. The proposed method was demonstrated in phantom and in-vivo experiments on a 3T scanner.

---

[1]This chapter is based on [97]

6.2 Theory

Similar to [81], the proposed method works by linearly combining two phase-cycled acquisitions with B_0 map acquired separately. The noiseless reconstructed images of the two acquisitions are modeled as:

$$\begin{cases} S_1(\boldsymbol{x}) = W(\boldsymbol{x})P_1(f_W(\boldsymbol{x})) + F(\boldsymbol{x})P_1'(f_F(\boldsymbol{x})) \\ \\ S_2(\boldsymbol{x}) = W(\boldsymbol{x})P_2(f_W(\boldsymbol{x})) + F(\boldsymbol{x})P_2'(f_F(\boldsymbol{x})) \end{cases} \tag{6.2.1}$$

where $S_1(\boldsymbol{x})$ and $S_2(\boldsymbol{x})$ are pixel values of the two acquisitions at location $\boldsymbol{x}$, $W(\boldsymbol{x})$ and $F(\boldsymbol{x})$ are the transverse magnetizations of water and fat respectively, $P_i(\cdot)$ and $P_i'(\cdot)$ are signal profiles of the ith acquisition in terms of $f_W(\boldsymbol{x})$ and $f_F(\boldsymbol{x})$ which are the offset frequencies of water and fat respectively, e.g., $f_F(\boldsymbol{x}) = f_W(\boldsymbol{x}) - 440$ Hz at 3T. $P_i(\cdot)$ and $P_i'(\cdot)$ are both normalized so that the tissue contrast is preserved in $W(\boldsymbol{x})$ and $F(\boldsymbol{x})$; $P_i(\cdot)$ and $P_i'(\cdot)$ are centered around the water and fat center frequencies respectively, and they are not exactly the same as each other due to large difference of T_1; however, it is shown below that $P_i(\cdot)$ and $P_i'(\cdot)$ are relatively insensitive to T_1, T_2 values within their own reasonable ranges. Since $P_i(\cdot)$ and $P_i'(\cdot)$ can be determined based on imaging parameters and our G-STFR signal model accurately [85], there is no approximation necessary for $P_i(\cdot)$ and $P_i'(\cdot)$, unlike the sinusoidal assumption in [81]. Calculations of the linear combination weights $\alpha_i^W(\boldsymbol{x})$, which are used for calculating water-only images, are described as:

$$\begin{cases} \alpha_1^W(\boldsymbol{x})P_1(f_W(\boldsymbol{x})) + \alpha_2^W(\boldsymbol{x})P_2(f_W(\boldsymbol{x})) = 1 \\ \\ \alpha_1^W(\boldsymbol{x})P_1'(f_F(\boldsymbol{x})) + \alpha_2^W(\boldsymbol{x})P_2'(f_F(\boldsymbol{x})) = 0 \end{cases} \tag{6.2.2}$$

where the spectra of water and fat are set to be 1 and 0 respectively. Similarly, we can also calculate fat-only images by calculating the linear combination weights $\alpha_i^F(\boldsymbol{x})$ as

follows:

$$
\begin{cases}
\alpha_1^F(\boldsymbol{x})P_1(f_W(\boldsymbol{x})) + \alpha_2^F(\boldsymbol{x})P_2(f_W(\boldsymbol{x})) = 0 \\
\alpha_1^F(\boldsymbol{x})P_1{}'(f_F(\boldsymbol{x})) + \alpha_2^F(\boldsymbol{x})P_2{}'(f_F(\boldsymbol{x})) = 1
\end{cases}
\tag{6.2.3}
$$

For a given imaging sequence, these weights can be pre-computed offline for reasonable ranges of frequencies, and the weights for each pixel can be looked up from this pre-computed table according to the local B_0 inhomogeneity during the real-time experiment. With the linear combination weights for each pixel, we can calculate the water-only and fat-only images as follows on a pixel-by-pixel base:

$$
\begin{cases}
W(\boldsymbol{x}) = \alpha_1^W(\boldsymbol{x})S_1(\boldsymbol{x}) + \alpha_2^W(\boldsymbol{x})S_2(\boldsymbol{x}) \\
F(\boldsymbol{x}) = \alpha_1^F(\boldsymbol{x})S_1(\boldsymbol{x}) + \alpha_2^F(\boldsymbol{x})S_2(\boldsymbol{x})
\end{cases}
\tag{6.2.4}
$$

We proposed a G-STFR sequence with both the tip-down and the tip-up pulses to be the same regular selective or hard excitation pulses. Empirically, we found that the profiles are insensitive to flip angles ranging from 16^0 to 90^0 which cover the optimal values for most applications.

For better robustness, we proposed an iterative method to calculate $\alpha_1^W(\boldsymbol{x})$ and $\alpha_1^F(\boldsymbol{x})$ as follows:

$$
\begin{bmatrix} \hat{\alpha}_1^W(\boldsymbol{x}) \\ \hat{\alpha}_2^W(\boldsymbol{x}) \end{bmatrix} = \operatorname*{argmin}_{\alpha_1^W(\boldsymbol{x}), \alpha_2^W(\boldsymbol{x})} \left\| \begin{bmatrix} 1 \\ 0 \end{bmatrix} - \left| \begin{bmatrix} P_1(f_W(\boldsymbol{x})) & P_2(f_W(\boldsymbol{x})) \\ P_1{}'(f_F(\boldsymbol{x})) & P_2{}'(f_F(\boldsymbol{x})) \end{bmatrix} \begin{bmatrix} \alpha_1^W(\boldsymbol{x}) \\ \alpha_2^W(\boldsymbol{x}) \end{bmatrix} \right| \right\|_2^2
\tag{6.2.5}
$$

which is an example for calculating $\alpha_i^W(\boldsymbol{x})$; in 6.2.5, absolute values are taken to relax the irrelevant phase of water image, which is a magnitude least square problem [35]. By adjusting the free procession time such that water and fat sit at the peak or the bottom in each magnitude profile, the problem can be manipulated to be very well-conditioned, so regularization is not necessary in 6.2.5 to control the magnitude of

$\alpha_i^W(\boldsymbol{x})$ or $\alpha_i^F(\boldsymbol{x})$.
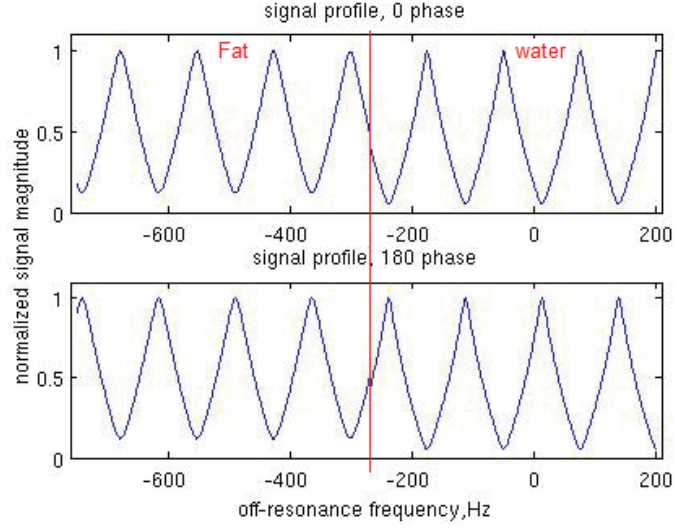
Figure 6.2.1: Profiles of 0 and 180^0 phase-cycled signals by the proposed G-STFR sequence. These profiles are produced by typical T_1, T_2 values of water and fat for demonstration purpose.
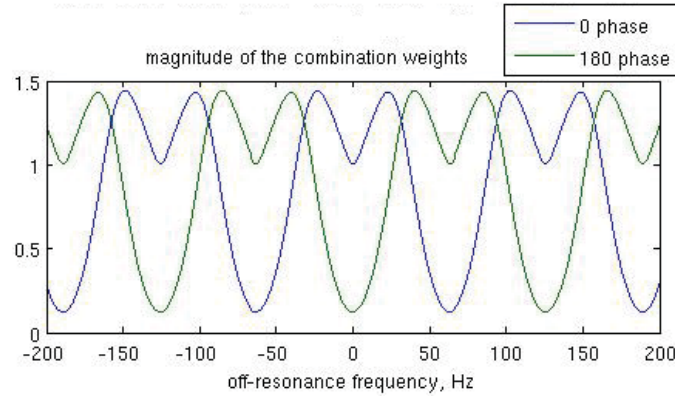
Figure 6.2.2: Examples of the magnitudes of the linear combination weights $\alpha_i^W(\boldsymbol{x})$ for water-only imaging.

Furthermore, since the signal profiles are calculated assuming infinitely narrow spectra of each component in the voxel, which is not true in practice, we assume Lorentzian-shaped spectra for water and fat which are convolved with $P_i(\cdot)$ and $P_i'(\cdot)$ respectively to produce more realistic signal profiles. Fig. 6.2.1 demonstrates some examples of $P_i(\cdot)$ and $P_i'(\cdot)$, and examples of the magnitudes of the linear combination

144

weights $\alpha_i^W(\boldsymbol{x})$ for water-only imaging are shown in Fig. 6.2.2. As seen in this example, the magnitude of the weights are smaller than 1.5, which means there will not be much noise amplification when applying the linear combinations.

6.3 Methods and Results

6.3.1 Simulations

We first simulated the complex signal profiles, i.e., $P_i(\cdot)$ and $P_i'(\cdot)$, of water and fat produced by G-STFR over ranges of tissue parameters, i.e., 40 ms $\leqslant T_{2,fat} \leqslant 100$ ms, 150 ms $\leqslant T_{1,fat} \leqslant 250$ ms, 60 ms $\leqslant T_{2,water} \leqslant 200$ ms, and 0.6 s $\leqslant T_{1,water} \leqslant 2$ s. The results in Fig. 6.3.1 demonstrate that the signal profiles are relatively insensitive to different tissue types, so the method can work based on certain uniform tissue parameters.
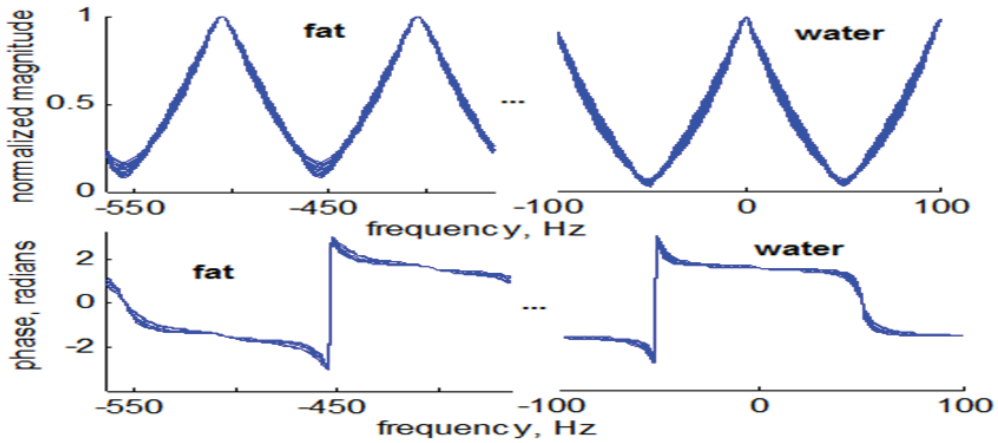
Figure 6.3.1: G-STFR signal profiles for ranges of T_1, T_2 values.

6.3.2 Phantom Experiments

We tested the method in a spherical phantom filled with water (MnCl$_2$ doped) and mineral oil on a 3T GE scanner. The actual T_1, T_2 values are: $T_{1,oil} \approx 200$ ms, $T_{2,oil} \approx 22$ ms, $T_{1,water} \approx 1$ s, $T_{2,water} \approx 80$ ms. A linear gradient was turned on to

generate some B_0 inhomogeneity ($-90 \sim 130$ Hz). 3D G-STFR was used to acquire $S_1(\boldsymbol{x})$ and $S_2(\boldsymbol{x})$: FOV $= 24 \times 24 \times 10$ cm, spin-warp readout, $64 \times 64 \times 20$ matrix size, $T_R = 8$ ms, $T_E = 3.1$ ms, the free procession time $T_{free} = 5.4$ ms, flip angles were about 35^0. To demonstrate the robustness of the method to model mismatch, we used inaccurate T_1, T_2 values to calculate $\alpha_i^W(\boldsymbol{x})$ and $\alpha_i^F(\boldsymbol{x})$, i.e., $T_{1,oil} = 150$ ms, $T_{2,oil} = 70$ ms, $T_{1,water} = 2$ s, $T_{2,water} = 120$ ms. In addition, a bSSFP image with $T_R = 5.38$ ms was acquired for the same object.
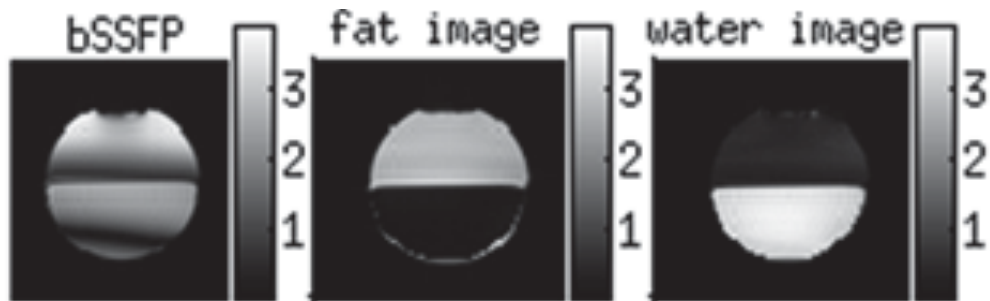
Figure 6.3.2: The phantom experiment result.

Fig. 6.3.2 shows results from one of the axial slices: The proposed method makes relatively uniform water (on the bottom) and fat (on the top and some attached to the bottom) images without banding artifacts compared to the bSSFP image.

6.3.3 In-vivo Experiments

Furthermore, the method was tested with the same 3D G-STFR sequence in a human head on the 3T GE scanner. We acquired 3D images of a 4 cm thick axial slab around eyes: FOV $= 24 \times 24 \times 10$ cm, spin-warp readout, $256 \times 256 \times 20$ matrix size, $T_R = 10.6$ ms, $T_E = 4.0$ ms, the free procession time $T_{free} = 8.0$ ms, flip angles are about 20^0. A corresponding bSSFP image with $T_R = 8.0$ ms was acquired. We use uniform tissue parameters for the reconstruction: $T_{1,fat} = 200$ ms, $T_{2,fat} = 70$ ms, $T_{1,water} = 1$ s, $T_{2,water} = 100$ ms.

Fig. 6.3.3 shows one of the slices, where the fat (behind eye balls and around

skull) and the water image are separated. With a relatively uniform B_0 field, we only observe a small banding artifact in bSSFP (pointed by the red arrow) which is removed by the proposed method. There are still some artifacts in the combined results: the flow-induced artifacts around the through-slab arteries can be reduced by exciting a thicker slab and/or applying flow compensation gradients; moreover, the eye balls are not reconstructed well in both images, which might be due to eye motion between scans.
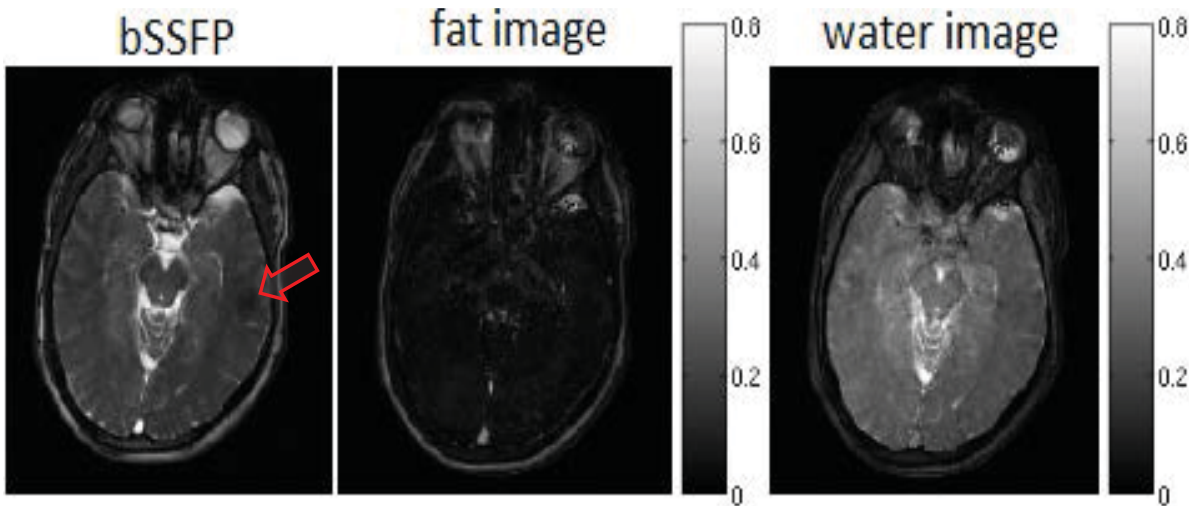
Figure 6.3.3: The in-vivo experiment result.

6.4   Conclusions

The proposed method for steady-state water fat separation and banding artifacts suppression is demonstrated at 3T. This steady-state method works for a wide range of flip angles and T_1, T_2 values, and it can potentially be an alternative to the bSSFP-based method which commonly requires high flip angle and thus high SAR.

However, some more work is still needed to improve the robustness of the method for different applications. We have investigated its use in human knees and calves at 3T, but the fat could not be suppressed completely in those experiments. We suspect

that the results are too sensitive to B_0 mapping errors in the regions where the signals are away from the bottoms and the peaks of the signal profiles (Fig. 6.2.1). Thus, one may consider to improve the signal model or modify the sequence to change the signal profiles, so that the methods can better tolerate such model mismatches.

CHAPTER VII

Future Work

For the separate magnitude and phase regularization discussed in Chapter II, more work can be done to improve the optimization algorithm for the phase. The nonlinear CG with backtracking line search generally works well in our experiments, but it is not guaranteed to converge fast enough all the time. Hence, one may investigate other optimization algorithms, such as optimization transfer [62] and nonlinear CG with monotonic line search [115] combined with augmented Lagrangian methods [141]. Furthermore, the method can potentially be improved by taking advantage of the correlation between the magnitude and the phase maps, such as boundary information. One drawback of this method is the additional regularization parameters that need to be determined, which are manually set in this work. One may investigate more automatic parameter selection methods, such as spatial resolution analysis based method [98] and Monte Carlo SURE-based method [142]. In addition, one may investigate the use of this work on more clinical applications other than temperature mapping and velocity mapping. This work can also be modified or extended to other applications that need phase reconstruction, and the work for BS B_1 mapping (Chapter III) is one example. More broadly, the method may be extended to applications outside MRI fields, e.g., terahertz imaging, holography, synthetic aperture radar and sonar [143].

For the BS B_1 mapping work discussed in Chapter III, the proposed alternating optimization for the regularized B_1 estimation can be improved to converge faster. Optimization for the B_1 magnitude may be accelerated by designing a monotonic line search method, and the phase part may also be improved with better surrogate functions for the monotonic line search. One may also investigate alternatives to the alternating optimization methods. Instead of estimating composite B_1 maps, regularized estimation of the individual B_1 maps directly can avoid noise amplification from decomposition of the composite B_1 maps. This could be challenging, because this method will involve an even more nonlinear and nonconvex cost function and it will be very challenging to design MLS updates for both B_1 magnitude and phase. For the coil combination optimization, one may compare the proposed method with existing solutions other than "all-but-one". Although the optimized coil combination works in practice, this CRLB analysis is only an approximation because the MLE of B_1 magnitude and phase are biased estimators in general. Furthermore, more estimation bias may be introduced if we include regularization to this method. Thus, future work could be to design a coil combination optimization based on the biased CRLB analysis [122] which is theoretically valid for the proposed regularized estimation. In addition, the proposed coil combination optimization does not contrain SAR, which could be of a concern in BS B_1 mapping sequences. Applying complex weights to PEX channels may cause unpredictable local SAR increase without the knowledge of local electromagnetic properties of the tissue [123], so a future work can be to consider SAR limit in the coil combination optimization, especially for high field PEX B_1 mapping. Moreover, simulated annealing produces random results which are not very robust and also highly depend on initial guess, so other optimization algorithms can be investigated for this problem. We only investigated the coil combination optimization for phantoms and simulations on human brain using SPGR based BS B_1 mapping sequences, so one may investigate this method on *in-vivo* experiments of different

150

parts of human body and with different BS B_1 mapping sequences. More future work could be done to investigate the proposed methods on applications at different field strengths. Although the proposed coil combination optimization was developed for BS B_1 mapping sequence, the framework of the CRLB based coil combination optimization can be applied to other popular multi-coil B_1 mapping methods, e.g., AFI [46].

For the 4D fat sat pulse design discussed in Chapter IV, there will be many opportunities to improve and extend the work on both technical side and clinical side in the future. First of all, the strategies for the phase initialization in the STA design is an open problem, and we suggest starting with randomly varying the phase over spatial locations while keeping it linear over frequency or using a longer pulse to initialize the phase. For the parallel excitation version of the design, more phantom and *in-vivo* experiments are needed for investigation. Other than the spoke trajectory and SPINS trajectory, one may study other 3D k-space trajectory, such k_T-points trajectory. Optimization of the k-space trajectory is another open problem for further research. Another idea that can possibly improve the design is to incorporate the spatial distribution of water or fat into the design, which may be obtained by segmentation of the images acquired for field mapping. In addition, the study of local SAR needs to be incorporated into the design before further research on clinical applications. Certainly, more research is needed for the clinical use of this work, such as abdominal imaging. Furthermore, investigation of the proposed method at different main field strengths could be an interesting future work. At lower field where the pulse length of the conventional fat sat is more problematic, the 4D fat sat pulse could be even more advantageous, because sparser sampling along k_f at lower field allows the 4D fat sat pulse to better compensate for spatial variations which is smaller than at 3T, so that the task in the spectral domain can be simplified even more. In addition, SAR is less of a concern at lower field strength. On the other hand, it will

be more challenging to design 4D fat sat pulses at fields higher than 3T where B_0 and B_1 inhomogeneity is more severe. In such designs, the required shorter sampling interval along k_f leaves smaller room for the pulse to compensate for the even larger spatial variations, and parallel excitation will probably be required. Since the pulse length of the conventional fat sat is less of an issue at high field, the proposed method will mainly help to compensate for the field inhomogeneities rather than to shorten the pulse length. We have done some simulation studies on 7T 4D fat sat pulse design which showed some promising results, but SAR may be more problematic.

For the fat sat and MT work discussed in Chapter V, one may design experiments to separate the fat sat effect and the MT effect. Although it is demonstrated in the section 5.4.3 that the majority of attenuation in the MT phantom should be caused by MT effect, more precise studies may be required for quantitative MT studies. Moreover, the phase increments in the adapted RF spoiling schemes may be optimized for better robustness. Similar to the fat sat pulse work, further research of this work includes investigation of the sequences on different field strengths and other clinical applications, e.g., breast imaging, lung imaging and cardiac imaging. It is also interesting to study the parallel excitation version of the proposed method. The study of local SAR for the proposed sequences is also very important. Furthermore, it may also be interesting to investigate the proposed pulse for other saturation transfer techniques, such as chemical exchange saturation transfer [144].

For the water-fat separation work discussed in Chapter VI, some more work is still needed to improve the robustness of the method for different applications. In some situations, the reconstruction results of the proposed method may be too sensitive to B_0 mapping errors. Thus, one may consider to improve the signal model or modify the sequence to change the signal profiles, so that the methods can better tolerate such model mismatches.

APPENDICES

APPENDIX A

Separate magnitude and phase regularization

A.1 The cost function for x

$$\Psi(\boldsymbol{x}, \boldsymbol{m}^{(n)}) = \|\boldsymbol{y} - A\boldsymbol{m}^{(n)} e^{i\boldsymbol{x}}\|^2 + \beta_1 R_x(\boldsymbol{x}) + \beta_2 \|U'\boldsymbol{m}^{(n)}\|_1 \tag{A.1}$$

where $R_x(\boldsymbol{x})$ represents any possible regularizer for the phase map, including the four regularizers discussed in Chapter II.

A.2 Newton Raphson algorithm in the line search for PCG

Let define a 1D cost function for the optimized step size α:

$$f_n(\alpha) = \Psi_l(\boldsymbol{x}^{(n)} + \alpha\boldsymbol{d}^{(n)}, \boldsymbol{m}^{(n)}) \tag{A.1}$$

where $\boldsymbol{d}^n$ is the search direction for $\boldsymbol{x}^{(n+1)}$ by PCG. Using 2.2.8:

$$f_n(\alpha) = L(\boldsymbol{x}^{(n)} + \alpha\boldsymbol{d}^{(n)}) + \beta_l R_l(\boldsymbol{x}^{(n)} + \alpha\boldsymbol{d}^{(n)}) \tag{A.2}$$

where $L(\boldsymbol{x}) \triangleq \|\boldsymbol{y} - A\boldsymbol{m}^{(n)}e^{i\boldsymbol{x}}\|^2$.

Then we update $\boldsymbol{x}$ as the following:

$$\boldsymbol{x}^{(n+1)} = \boldsymbol{x}^{(n)} + \hat{\alpha}_n \boldsymbol{d}^{(n)} \tag{A.3}$$

where $\hat{\alpha}_n$ denotes the optimized step size α and it is updated as follows:

$$\alpha^{(k+1)} = \alpha^{(k)} - \frac{\dot{f}_n(\alpha^{(k)})}{\ddot{f}_n(\alpha^{(k)})} \tag{A.4}$$

where

$$\dot{f}_n(\alpha) = \boldsymbol{d}^{(n)'}[\nabla L(\boldsymbol{x}^{(n)} + \alpha \boldsymbol{d}^{(n)}) + \beta_1 \nabla R_l(\boldsymbol{x}^{(n)} + \alpha \boldsymbol{d}^{(n)})] \tag{A.5}$$

$$\ddot{f}_n(\alpha) = \boldsymbol{d}^{(n)'}[\nabla^2 L(\boldsymbol{x}^{(n)} + \alpha \boldsymbol{d}^{(n)}) + \beta_1 \nabla^2 R_l(\boldsymbol{x}^{(n)} + \alpha \boldsymbol{d}^{(n)})]\boldsymbol{d}^{(n)} \tag{A.6}$$

A.3 Gradients and Hessian matrices (real unknowns)

a) The data fit term $L(\boldsymbol{x})$:

$$\nabla L(\boldsymbol{x}) = 2\mathsf{Re}\{\mathsf{diag}\{ie^{-i\boldsymbol{x}}\}[A_m{}'(\boldsymbol{y} - A_m e^{i\boldsymbol{x}})]\} = 2\mathsf{Re}\{\boldsymbol{g}_1(\boldsymbol{x})\} \tag{A.1}$$

$$\nabla^2 L(\boldsymbol{x}) = 2\mathsf{Re}\{\mathsf{diag}\{e^{-i\boldsymbol{x}} \cdot * A_m{}'(\boldsymbol{y} - A_m e^{i\boldsymbol{x}})\} + \mathsf{diag}\{e^{-i\boldsymbol{x}}\}A_m{}'A_m\mathsf{diag}\{e^{i\boldsymbol{x}}\}\} \tag{A.2}$$

where $A_m \triangleq A * \mathsf{diag}\{\boldsymbol{m}^{(n)}\}$, ".*" means entry-by-entry multiplication, $\boldsymbol{g}_1(\boldsymbol{x}) \triangleq \mathsf{diag}\{ie^{-i\boldsymbol{x}}\}[A_m{}'(\boldsymbol{y} - A_m e^{i\boldsymbol{x}})]$. Note that since $\nabla^2 L(\boldsymbol{x})$ is only used in A.6, the equation A.2, which is very expensive, does not need to be computed explicitly. Combing

A.6-A.2 yields an efficient expression for $\ddot{f}_n(\alpha)$:

$$\ddot{f}_n(\alpha) = 2(\text{Re}\{\boldsymbol{d}^{(n)'}[(-i\boldsymbol{g}_1(\boldsymbol{x_d}).*\boldsymbol{d}^{(n)})]\} + \boldsymbol{b}_1'\boldsymbol{b}_1) + \ddot{f}_{R,n}(\alpha) \tag{A.3}$$

where $\boldsymbol{x_d} \triangleq \boldsymbol{x}^{(n)} + \alpha\boldsymbol{d}^{(n)}$, $\boldsymbol{b}_1 \triangleq A_m\text{diag}\{e^{i\boldsymbol{x_d}}\}\boldsymbol{d}^{(n)}$, and $\ddot{f}_{R,n}(\alpha) \triangleq \beta_1\boldsymbol{d}^{(n)'}\nabla^2 R_x(\boldsymbol{x_d})\boldsymbol{d}^{(n)}$.

b) The regularizers $R_l(\boldsymbol{x})$:

(1) Regularizer 1:

$$R_1(\boldsymbol{x}) = \|C\boldsymbol{x}\|^2 \tag{A.4}$$

$$\nabla R_1(\boldsymbol{x}) = 2C'C\boldsymbol{x} \tag{A.5}$$

$$\nabla^2 R_1(\boldsymbol{x}) = 2C'C \tag{A.6}$$

In A.3, $\ddot{f}_{R,n}(\alpha)$ can be simplified as: $\ddot{f}_{R,n}(\alpha) = 2\beta_1\|C\boldsymbol{d}^{(n)}\|^2$.

(2) Regularizer 2:

$$R_2(\boldsymbol{x}) = \|Ce^{\boldsymbol{x}}\|^2 \tag{A.7}$$

$$\nabla R_2(\boldsymbol{x}) = -2\text{Re}\{ie^{-i\boldsymbol{x}}.*[C'C\boldsymbol{x}]\} = -2\text{Re}\{\boldsymbol{g}_2(\boldsymbol{x})\} \tag{A.8}$$

$$\nabla^2 R_2(\boldsymbol{x}) = 2\text{Re}\{\text{diag}\{e^{-i\boldsymbol{x}}\}C'C\text{diag}\{e^{i\boldsymbol{x}}\} - \text{diag}\{e^{-i\boldsymbol{x}}.*(C'Ce^{i\boldsymbol{x}})\}\} \tag{A.9}$$

where $\boldsymbol{g}_2(\boldsymbol{x}) \triangleq ie^{-i\boldsymbol{x}}.*[C'Ce^{i\boldsymbol{x}}]$.

In A.3, $\ddot{f}_{R,n}(\alpha) = 2\beta_1(\text{Re}\{\boldsymbol{d}^{(n)'}[(-i\boldsymbol{g}_2(\boldsymbol{x_d})).*\boldsymbol{d}^{(n)}]\}+\boldsymbol{b}_2'\boldsymbol{b}_2)$, where $\boldsymbol{b}_2 \triangleq C\text{diag}\{e^{i\boldsymbol{x_d}}\}\boldsymbol{d}^{(n)}$.

(3) Regularizer 3:

$$R_3(\boldsymbol{x}) = \sum_{k=1}^{K} \psi_k([C\boldsymbol{x}]_k) \tag{A.10}$$

$$\nabla R_3(\boldsymbol{x}) = C'\mathsf{diag}\{\omega_\psi(C\boldsymbol{x})\}C\boldsymbol{x} \tag{A.11}$$

$$\nabla^2 R_3(\boldsymbol{x}) = C'\mathsf{diag}\{\ddot{\psi}_k(C\boldsymbol{x})\}C \tag{A.12}$$

In A.3, $\ddot{f}_{R,n}(\alpha) = 2\beta_1 \boldsymbol{p}'\mathsf{diag}\{\ddot{\psi}_k(C\boldsymbol{x_d})\}\boldsymbol{p}$, where $\boldsymbol{p} \triangleq C\boldsymbol{d}^{(n)}$.

(4) Regularizer 4:

$$R_4(\boldsymbol{x}) = \sum_{k=1}^{K} \psi_k(|[Ce^{i\boldsymbol{x}}]_k|) \tag{A.13}$$

$$\nabla R_4(\boldsymbol{x}) = -\mathsf{Re}\{e^{-i\boldsymbol{x}}.*[C'\mathsf{diag}\{\omega_\psi(|Ce^{i\boldsymbol{x}}|)\}Ce^{i\boldsymbol{x}}\} \tag{A.14}$$

$$
\begin{aligned}
\nabla^2 R_4(\boldsymbol{x}) = {}& -\mathsf{Re}\{\mathsf{diag}\{e^{-i\boldsymbol{x}}.*[C'\mathsf{diag}\{\omega_\psi(|Ce^{i\boldsymbol{x}}|)\}Ce^{i\boldsymbol{x}}]\}\} \\
& + \mathsf{Re}\{\mathsf{diag}\{e^{-i\boldsymbol{x}}\}C'\mathsf{diag}\{\omega_\psi(|Ce^{i\boldsymbol{x}}|)\}C\mathsf{diag}\{e^{i\boldsymbol{x}}\}\} \\
& + \mathsf{Re}\{i*\mathsf{diag}\{e^{-i\boldsymbol{x}}\}C'\mathsf{diag}\{\dot{\omega}_\psi(|Ce^{i\boldsymbol{x}}|)\}.*(Ce^{i\boldsymbol{x}})./|Ce^{i\boldsymbol{x}}|\}\} \\
& *\mathsf{Re}\{i*\mathsf{diag}\{Ce^{i\boldsymbol{x}}\}C\mathsf{diag}\{e^{-i\boldsymbol{x}}\}\}
\end{aligned}
\tag{A.15}
$$

If $\boldsymbol{g}_3(\boldsymbol{x}) \triangleq ie^{-i\boldsymbol{x}}.*[C'\mathsf{diag}\{\omega_\psi(|Ce^{i\boldsymbol{x}}|)\}\boldsymbol{h}(\boldsymbol{x})]$ and $\boldsymbol{h}(\boldsymbol{x}) \triangleq Ce^{i\boldsymbol{x}}$, then in A.3, $\ddot{f}_{R,n}(\alpha) = 2\beta_1(\mathsf{Re}'[(-i\boldsymbol{g}_3(\boldsymbol{x_d})).*\boldsymbol{d}^{(n)}]\} + \boldsymbol{b_2}'\mathsf{diag}\{\omega_\psi(|\boldsymbol{h}(\boldsymbol{x_d})|)\}\boldsymbol{b_2} + \boldsymbol{b_3}\boldsymbol{b_4})$, where $\boldsymbol{b_3} \triangleq \mathsf{Re}\{i\boldsymbol{b_2}'\mathsf{diag}\{\dot{\omega}_\psi(|\boldsymbol{h}(\boldsymbol{x_d})|).*(\boldsymbol{h}(\boldsymbol{x_d}))./|\boldsymbol{h}(\boldsymbol{x_d})|\}\}$, $\bar{x}$ denotes the conjugate of x, and $\boldsymbol{b_4} \triangleq \mathsf{Re}\{i*\mathsf{diag}\{\boldsymbol{h}(\boldsymbol{x_d})\}\bar{\boldsymbol{b}}_2\}$.

APPENDIX B

Bloch-Siegert B_1 mapping

B.1 Optimization Algorithms for the Regularized Estimation

The detailed derivations for the optimization algorithm used for the regularized BS estimations (3.2.7), i.e. CG-LS, are shown in this section. For a general cost function $\Psi(\boldsymbol{x})$ of the unknown $\boldsymbol{x}$, an optimized step size α needs to be determined in each iteration of the CG algoritm. α in the nth iteration is found by optimizing the line search function $f_n(\boldsymbol{\alpha})$:

$$
\begin{aligned}
f_n(\alpha) &\triangleq \Psi(\boldsymbol{x}^{(n)} + \alpha \boldsymbol{d}^{(n)}) \\
&= L(\boldsymbol{x}^{(n)} + \alpha \boldsymbol{d}^{(n)}) + \beta R(\boldsymbol{x}^{(n)} + \alpha \boldsymbol{d}^{(n)})
\end{aligned}
\tag{B.1}
$$

where $\boldsymbol{d}^{(n)}$ denotes the search direction for $\boldsymbol{x}^{(n+1)}$ by CG algorithm, the cost function is the sum of data fit term $L(\boldsymbol{x}^{(n)} + \alpha \boldsymbol{d}^{(n)})$ and regularization term $R(\boldsymbol{x}^{(n)} + \alpha \boldsymbol{d}^{(n)})$, and β is the scalar regularization parameter. $\boldsymbol{x}$ is updated in the algorithm as follows:

$$
\boldsymbol{x}^{(n+1)} = \boldsymbol{x}^{(n)} + \hat{\alpha}_n \boldsymbol{d}^{(n)}
\tag{B.2}
$$

where $\hat{\alpha}_n$ is the optimized step size and it is optimized by iterative updates as follows:

$$\alpha_n^{(m+1)} = \alpha_n^{(m)} - \frac{\dot{f}_n(\alpha_n^{(m)})}{\breve{c}^{(m)}} \tag{B.3}$$

where $\breve{c}^{(m)} = \ddot{f}_n(\alpha^{(m)})$ when it is BLS and $\breve{c}^{(m)}$ is independent of $\alpha^{(m)}$ and is an upper bound of $\ddot{f}_n(\alpha)$ when it is MLS.

We use CG-BLS for the B_1 magnitude updates where the step size update is done by plugging $\breve{c}^{(k)} = \ddot{f}_n(\alpha)$ into (B.3). For the B_1 phase, we use CG-MLS and the derivation for the design of $\breve{c}^{(k)}$ is shown in the following:

$$\ddot{f}_n(\alpha) = \ddot{L}(\boldsymbol{x}^{(n)} + \alpha \boldsymbol{d}^{(n)}) + \beta \ddot{R}(\boldsymbol{x}^{(n)} + \alpha \boldsymbol{d}^{(n)}) \tag{B.4}$$

According to (3.2.7):

$$\begin{aligned}
\nabla^2 L(\tilde{\boldsymbol{\phi}}) &= \mathsf{diag}\{\frac{\partial L^2(\tilde{\boldsymbol{\phi}})}{\partial \phi_j^2}\} \\
&= \mathsf{diag}\{ \sum_{\varsigma=+,-} 2Re\{\boldsymbol{S}_j^\varsigma \boldsymbol{M}_j^\varsigma e^{-i(\boldsymbol{K}_{BS,j}^\varsigma \tilde{\boldsymbol{B}}_j^2 + \tilde{\phi}_j')}\}\} \\
&\leq \mathsf{diag}\{ \sum_{\varsigma=+,-} 2|\boldsymbol{S}_j^\varsigma \boldsymbol{M}_j^\varsigma|\}
\end{aligned} \tag{B.5}$$

where $j = 1, 2, \ldots, N \times N_p$, and $Re\{\cdot\}$ denotes the real part of the number. Therefore,

$$\begin{aligned}
\ddot{L}(\boldsymbol{x}^{(n)} + \alpha \boldsymbol{d}^{(n)}) &= \boldsymbol{d}^{(n)H}[\nabla^2 L(\boldsymbol{x}^{(n)} + \alpha \boldsymbol{d}^{(n)})]\boldsymbol{d}^{(n)} \\
&\leq \boldsymbol{d}^{(n)H} \mathsf{diag}\{ \sum_{\varsigma=+,-} 2|\boldsymbol{S}_j^\varsigma \boldsymbol{M}_j^\varsigma|\}\boldsymbol{d}^{(n)}
\end{aligned} \tag{B.6}$$

159

The regularization term:

$$R(\boldsymbol{x}^{(n)} + \alpha \boldsymbol{d}^{(n)}) = \|Ce^{i(\boldsymbol{x}^{(n)} + \alpha \boldsymbol{d}^{(n)})}\|^2$$

$$= \sum_k |\sum_j c_{kj} e^{i(x_j^{(n)} + \alpha d_j^{(n)})}|^2$$

$$= \sum_k |\sum_j z_{kj} e^{i\alpha d_j^{(n)}}|^2$$

$$= \sum_k (\sum_j z_{kj}^* e^{-i\alpha d_j^{(n)}})(\sum_l z_{kl} e^{i\alpha d_l^{(n)}})$$

$$= \sum_k \sum_j |z_{kj}|^2 \qquad\qquad\qquad\qquad (B.7)$$

$$+ 2\sum_k \sum_j \sum_{l>j} Re\{z_{kj}^* z_{kl} e^{i\alpha(d_l^{(n)} - d_j^{(n)})}\}$$

$$= \sum_k \sum_j |z_{kj}|^2$$

$$+ 2\sum_j \sum_{l>j} |p_{jl}| \cos(\alpha(d_l^{(n)} - d_j^{(n)}) + \angle p_{jl})$$

where $k = 1, 2, \ldots, N_i$, N_i is the number of rows of the finite differencing matrix C, $j = 1, 2, \ldots, N_p$, $l = 1, 2, \ldots, N_p$, c_{kj} is the element in the kth row jth column of C, $z_{kj} \triangleq c_{kj} e^{ix_j^{(n)}}$, and $p_{jl} \triangleq \sum_k z_{kj}^* z_{kl}$. Therefore,

$$\ddot{R}(\boldsymbol{x}^{(n)} + \alpha \boldsymbol{d}^{(n)}) \leq 2\sum_j \sum_{l>j} |p_{jl}|(d_l^{(n)} - d_j^{(n)})^2$$

$$= \sum_j \sum_l |p_{jl}|(d_l^{(n)} - d_j^{(n)})^2 \qquad\qquad (B.8)$$

$$= 2[\sum_j \sum_l |p_{jl}|d_j^{(n)2} - \sum_j \sum_l d_j^{(n)} |p_{jl}| d_l^{(n)}]$$

$$= 2[\underline{\boldsymbol{1}}^T M \boldsymbol{d}^{(n)} - \boldsymbol{d}^{(n)H} M \boldsymbol{d}^{(n)}]$$

where $\underline{\boldsymbol{1}}$ is the column vector with elements to be 1, M denotes the $N_p \times N_p$ matrix

160

where the element in the kth row and jth column is $|p_{jl}|$.

$$M = |C^H C| = |C^H||C| \tag{B.9}$$

where $|Z|$ denotes the matrix the elements of which are absolute values of those of the matrix Z. Therefore, the curvature $\breve{c}^{(m)}$ in the mth iteration of the step size optimization is designed as follows:

$$
\begin{aligned}
\breve{c}^{(k)} &= \boldsymbol{d}^{(n)^H} \mathsf{diag}\{ \sum_{\varsigma=+,-} 2|\boldsymbol{S}_j^\varsigma \boldsymbol{M}_j^\varsigma|\} \boldsymbol{d}^{(n)} \\
&+ 2[\underline{\boldsymbol{1}}^T |C^H||C|\boldsymbol{d}^{(n)} - \||C|\boldsymbol{d}^{(n)}\|^2]
\end{aligned}
\tag{B.10}
$$

where $|C|$ can be implemented efficiently [145].

B.2 CRLB Analysis

This section shows the detailed derivation for the CRLB analysis discussed in section II.E. Following (3.3.2), we can get the log-likelihood, $L(\boldsymbol{\theta})$, and its gradient:

$$L(\boldsymbol{\theta}) = -\frac{1}{2\sigma^2}(\boldsymbol{y} - \boldsymbol{\mu}(\boldsymbol{\theta}))^H (\boldsymbol{y} - \boldsymbol{\mu}(\boldsymbol{\theta})) \tag{B.1}$$

$$\nabla L(\boldsymbol{\theta}) = \frac{1}{\sigma^2}[\nabla \boldsymbol{\mu}(\boldsymbol{\theta})]\boldsymbol{\epsilon} \tag{B.2}$$

where the superscripts H denotes Hermitian transpose, and ∇ denotes column gradient of vectors. Thus, the estimation satisfies the regularity condition, i.e., $E(\nabla L(\boldsymbol{\theta})) = \boldsymbol{0}$. The Fisher information $F(\theta)$ of this estimation is:

$$F(\boldsymbol{\theta}) \triangleq E[(\nabla L(\boldsymbol{\theta}))(\nabla L(\boldsymbol{\theta}))^H] = \frac{2M^2}{\sigma^2} \begin{bmatrix} 4K^2 B^2 & 0 \\ 0 & 1 \end{bmatrix} \tag{B.3}$$

161

According to CRLB, if the estimators $[\hat{B}, \hat{\phi}]$ are unbiased, their covariance has a lower bound:

$$\mathsf{cov}([\hat{B}, \hat{\phi}]) \geqslant F(\boldsymbol{\theta})^{-1} \tag{B.4}$$

Assuming $\hat{B}$ and $\hat{\phi}$ are close to the true values, the variance of $\hat{B}e^{i\hat{\phi}}$ can be derived by Taylor expansion approximation. For an arbitrary multi-dimensional function $g(\boldsymbol{z})$, we have:

$$g(\boldsymbol{z}) \approx g(\bar{\boldsymbol{z}}) + \nabla g(\bar{\boldsymbol{z}})(\boldsymbol{z} - \bar{\boldsymbol{z}}) \tag{B.5}$$

$$\mathsf{var}(g(\boldsymbol{z})) \approx \nabla g(\bar{\boldsymbol{z}}) \mathsf{cov}(\boldsymbol{z}) \nabla g(\bar{\boldsymbol{z}})^H \tag{B.6}$$

so if $\boldsymbol{z} = (\hat{B}, \hat{\phi})$, $g(\boldsymbol{z}) = \hat{B}_n e^{i\hat{\phi}}$, $\nabla g(\bar{\boldsymbol{z}}) = E[e^{i\phi}, iBe^{i\phi}]$, and (B.4) are plugged into (B.6), we have:

$$\mathsf{var}(\hat{\tilde{B}}_{n,\boldsymbol{r}}(A)e^{i\hat{\tilde{\phi}}'_{n,\boldsymbol{r}}(A)}) \geqslant \frac{\sigma^2}{2M^2_{n,\boldsymbol{r}}(A)}[\tilde{B}^2_{n,\boldsymbol{r}}(A) + \frac{1}{4K^2\tilde{B}^2_{n,\boldsymbol{r}}(A)}] \tag{B.7}$$

where we have put back the subscripts n, indices $\boldsymbol{r}$, primes and tildes in (3.2.5) except that we put indices $\boldsymbol{r}$ to the subscripts and make A be the argument, as A is the main unknown of this optimization problem.

We assume that noise in different scans is independent with each other, so the covariance $\hat{\tilde{C}}_{\boldsymbol{r}}(A) \triangleq [\hat{\tilde{B}}_{1,\boldsymbol{r}}(A)e^{i\hat{\tilde{\phi}}'_{1,\boldsymbol{r}}(A)}, \ldots, \hat{\tilde{B}}_{N,\boldsymbol{r}}(A)e^{i\hat{\tilde{\phi}}'_{N,\boldsymbol{r}}(A)}]$ is:

$$\mathsf{cov}(\hat{\tilde{C}}_{\boldsymbol{r}}(A)) = \mathsf{diag}\{\mathsf{var}(\hat{\tilde{B}}_{n,\boldsymbol{r}}(A)e^{i\hat{\tilde{\phi}}'_{n,\boldsymbol{r}}(A)})\} \tag{B.8}$$

Using (3.2.9), the covariance of the original individual B_1 estimates $\hat{C}_{\boldsymbol{r}}(A) \triangleq [\hat{B}_{1,\boldsymbol{r}}(A)e^{i\hat{\phi}'_{1,\boldsymbol{r}}(A)}, \ldots, \hat{B}_{N,\boldsymbol{r}}(A)e^{i\hat{\phi}'_{N,\boldsymbol{r}}(A)}]$ is:

$$\mathsf{cov}(\hat{C}_{\boldsymbol{r}}(A)) = A^{-1}\mathsf{cov}(\hat{\tilde{C}}_{\boldsymbol{r}}(A))A^{-H} \tag{B.9}$$

where $z^{-H} \triangleq (z^{-1})^H$. Since the diagonal entries of the covariance matrix are the variances of the elements of the estimator, then by plugging in (B.7) and (B.8) into (B.9), we can get the key formula of this CRLB analysis, which is (3.3.3).

BIBLIOGRAPHY

BIBLIOGRAPHY

[1] L. Sacolick, F. Wiesinger, I. Hancu, and M. Vogel, "B1 mapping by Bloch-Siegert shift," *Magnetic Resonance in Medicine*, vol. 63, no. 5, pp. 1315–1322, 2010.

[2] J.-F. Nielsen, D. Yoon, and D. C. Noll, "Small-tip fast recovery imaging using non-slice-selective tailored tip-up pulses and radiofrequency-spoiling," *Magnetic Resonance in Medicine*, 2012.

[3] J. P. Hornak, J. Szumowski, and R. G. Bryant, "Magnetic field mapping," *Magnetic resonance in medicine*, vol. 6, no. 2, pp. 158–163, 1988.

[4] A. Bernstein Matt, K. King, and X. Zhou, "Handbook of MRI pulse sequences," 2004.

[5] F. Bloch, "Nuclear induction," *Physical review*, vol. 70, no. 7-8, p. 460, 1946.

[6] E. M. Haacke, R. W. Brown, M. R. Thompson, and R. Venkatesan, *Magnetic resonance imaging: physical principles and sequence design*. Wiley-Liss New York:, 1999, vol. 1.

[7] T. S. Ibrahim, R. Lee, A. M. Abduljalil, B. A. Baertlein, and P.-M. L. Robitaille, "Dielectric resonances and¡ i¿ b¡/i¿¡ sub¿ 1¡/sub¿ field inhomogeneity in uhfmri: computational analysis and experimental findings," *Magnetic resonance imaging*, vol. 19, no. 2, pp. 219–226, 2001.

[8] Q. X. Yang, J. Wang, X. Zhang, C. M. Collins, M. B. Smith, H. Liu, X.-H. Zhu, J. T. Vaughan, K. Ugurbil, and W. Chen, "Analysis of wave behavior in lossy dielectric samples at high field," *Magnetic resonance in medicine*, vol. 47, no. 5, pp. 982–989, 2002.

[9] C. H. Cunningham, J. M. Pauly, and K. S. Nayak, "Saturated double-angle method for rapid b1+ mapping," *Magnetic Resonance in Medicine*, vol. 55, no. 6, pp. 1326–1333, 2006.

[10] J. Pauly, D. Nishimura, and A. Macovski, "A k-space analysis of small-tip-angle excitation," *Journal of Magnetic Resonance (1969)*, vol. 81, no. 1, pp. 43–56, 1989.

[11] B. P. Sutton, D. C. Noll, and J. A. Fessler, "Fast, iterative image reconstruction for mri in the presence of field inhomogeneities," *Medical Imaging, IEEE Transactions on*, vol. 22, no. 2, pp. 178–188, 2003.

[12] J. Pauly, D. Nishimura, and A. Macovski, "A linear class of large-tip-angle selective excitation pulses," *Journal of Magnetic Resonance (1969)*, vol. 82, no. 3, pp. 571–587, 1989.

[13] D. Xu, K. F. King, Y. Zhu, G. C. McKinnon, and Z.-P. Liang, "A noniterative method to design large-tip-angle multidimensional spatially-selective radio frequency pulses for parallel transmission," *Magnetic Resonance in Medicine*, vol. 58, no. 2, pp. 326–334, 2007.

[14] W. Grissom, C. Yip, S. Wright, J. Fessler, and D. Noll, "Additive angle method for fast large-tip-angle rf pulse design in parallel excitation," *Magnetic Resonance in Medicine*, vol. 59, no. 4, pp. 779–787, 2008.

[15] D. Xu, K. King, Y. Zhu, G. McKinnon, and Z. Liang, "Designing multichannel, multidimensional, arbitrary flip angle rf pulses using an optimal control approach," *Magnetic Resonance in Medicine*, vol. 59, no. 3, pp. 547–560, 2008.

[16] W. Grissom, D. Xu, A. Kerr, J. Fessler, and D. Noll, "Fast large-tip-angle multidimensional and parallel rf pulse design in MRI," *Medical Imaging, IEEE Transactions on*, vol. 28, no. 10, pp. 1548–1559, 2009.

[17] H. Zheng, T. Zhao, Y. Qian, T. S. Ibrahim, and F. E. Boada, "Improved large tip angle parallel transmission pulse design through a perturbation analysis of the bloch equation," *Magnetic Resonance in Medicine*, vol. 66, no. 3, pp. 687–696, 2011.

[18] J. Pauly, P. Le Roux, D. Nishimura, and A. Macovski, "Parameter relations for the Shinnar-Le Roux selective excitation pulse design algorithm [nmr imaging]," *Medical Imaging, IEEE Transactions on*, vol. 10, no. 1, pp. 53–65, 1991.

[19] C.-Y. Yip, W. A. Grissom, J. A. Fessler, and D. C. Noll, "Joint design of trajectory and rf pulses for parallel excitation," *Magnetic Resonance in Medicine*, vol. 58, no. 3, pp. 598–604, 2007.

[20] A. C. Zelinski, L. L. Wald, K. Setsompop, V. K. Goyal, and E. Adalsteinsson, "Sparsity-enforced slice-selective MRI rf excitation pulse design," *Medical Imaging, IEEE Transactions on*, vol. 27, no. 9, pp. 1213–1229, 2008.

[21] C. Ma, D. Xu, K. F. King, and Z.-P. Liang, "Joint design of spoke trajectories and rf pulses for parallel excitation," *Magnetic Resonance in Medicine*, vol. 65, no. 4, pp. 973–985, 2011.

[22] D. Yoon, J. A. Fessler, A. C. Gilbert, and D. C. Noll, "Fast joint design method for parallel excitation radiofrequency pulse and gradient waveforms considering

off-resonance," *Magnetic Resonance in Medicine*, vol. 68, no. 1, pp. 278–285, 2012.

[23] C.-y. Yip, J. A. Fessler, and D. C. Noll, "Iterative rf pulse design for multidimensional, small-tip-angle selective excitation," *Magnetic resonance in medicine*, vol. 54, no. 4, pp. 908–917, 2005.

[24] J. A. Fessler and B. P. Sutton, "Nonuniform fast fourier transforms using minmax interpolation," *Signal Processing, IEEE Transactions on*, vol. 51, no. 2, pp. 560–574, 2003.

[25] D. C. Noll, C. Meyer, J. Pauly, D. Nishimura, and A. Macovski, "A homogeneity correction method for magnetic resonance imaging with time-varying gradients," *Medical Imaging, IEEE Transactions on*, vol. 10, no. 4, pp. 629–637, 1991.

[26] L.-C. Man, J. M. Pauly, and A. Macovski, "Multifrequency interpolation for fast off-resonance correction," *Magnetic resonance in medicine*, vol. 37, no. 5, pp. 785–792, 1997.

[27] P. Börnert and B. Aldefeld, "On spatially selective rf excitation and its analogy with spiral mr image acquisition," *Magnetic Resonance Materials in Physics, Biology and Medicine*, vol. 7, no. 3, pp. 166–178, 1998.

[28] A. Haase, J. Frahm, W. Hanicke, and D. Matthaei, "1h nmr chemical shift selective (chess) imaging," *Physics in Medicine and Biology*, vol. 30, p. 341, 1985.

[29] K. Ward, A. Aletras, and R. Balaban, "A new class of contrast agents for mri based on proton chemical exchange dependent saturation transfer (cest)," *Journal of magnetic resonance*, vol. 143, no. 1, pp. 79–87, 2000.

[30] C. Meyer, J. Pauly, A. Macovskiand, and D. Nishimura, "Simultaneous spatial and spectral selective excitation," *Magnetic Resonance in Medicine*, vol. 15, no. 2, pp. 287–304, 1990.

[31] G. Morrell and A. Macovski, "Three-dimensional spectral-spatial excitation," *Magnetic resonance in medicine*, vol. 37, no. 3, pp. 378–386, 1997.

[32] C. Yang, W. Deng, V. Alagappan, L. Wald, and V. Stenger, "Four-dimensional spectral-spatial rf pulses for simultaneous correction of B1+ inhomogeneity and susceptibility artifacts in t2*-weighted mri," *Magnetic Resonance in Medicine*, vol. 64, no. 1, pp. 1–8, 2010.

[33] F. Zhao, J.-F. Nielsen, and D. C. Noll, "Four-dimensional spectral-spatial fat saturation pulse design," *Magnetic Resonance in Medicine*, 2014.

[34] W. Grissom, C. Yip, Z. Zhang, V. Stenger, J. Fessler, and D. Noll, "Spatial domain method for the design of rf pulses in multicoil parallel excitation," *Magnetic Resonance in Medicine*, vol. 56, no. 3, pp. 620–629, 2006.

[35] K. Setsompop, L. Wald, V. Alagappan, B. Gagoski, and E. Adalsteinsson, "Magnitude least squares optimization for parallel radio frequency excitation design demonstrated at 7 tesla with eight channels," *Magnetic Resonance in Medicine*, vol. 59, no. 4, pp. 908–915, 2008.

[36] S. Saekho, F. E. Boada, D. C. Noll, and V. A. Stenger, "Small tip angle three-dimensional tailored radiofrequency slab-select pulse for reduced b1 inhomogeneity at 3 t," *Magnetic resonance in medicine*, vol. 53, no. 2, pp. 479–484, 2005.

[37] S. Saekho, C. Yip, D. Noll, F. Boada, and V. Stenger, "Fast-kz three-dimensional tailored radiofrequency pulse for reduced b1 inhomogeneity," *Magnetic Resonance in Medicine*, vol. 55, no. 4, pp. 719–724, 2006.

[38] C. M. Collins, Z. Wang, W. Mao, J. Fang, W. Liu, and M. B. Smith, "Array-optimized composite pulse for excellent whole-brain homogeneity in high-field mri," *Magnetic Resonance in Medicine*, vol. 57, no. 3, pp. 470–474, 2007.

[39] Z. Zhang, C. Yip, W. Grissom, D. Noll, F. Boada, and V. Stenger, "Reduction of transmitter B1 inhomogeneity with transmit sense slice-select pulses," *Magnetic Resonance in Medicine*, vol. 57, no. 5, pp. 842–847, 2007.

[40] K. Setsompop, V. Alagappan, B. Gagoski, T. Witzel, J. Polimeni, A. Potthast, F. Hebrank, U. Fontius, F. Schmitt, L. L. Wald *et al.*, "Slice-selective rf pulses for in vivo b 1+ inhomogeneity mitigation at 7 tesla using parallel rf excitation with a 16-element coil," *Magnetic Resonance in Medicine*, vol. 60, no. 6, pp. 1422–1432, 2008.

[41] W. Deng, C. Yang, V. Alagappan, L. L. Wald, F. E. Boada, and V. A. Stenger, "Simultaneous z-shim method for reducing susceptibility artifacts with multiple transmitters," *Magnetic Resonance in Medicine*, vol. 61, no. 2, pp. 255–259, 2009.

[42] J. T. Schneider, R. Kalayciyan, M. Haas, S. R. Herrmann, W. Ruhm, J. Hennig, and P. Ullmann, "Inner-volume imaging in vivo using three-dimensional parallel spatially selective excitation," *Magnetic Resonance in Medicine*, 2012.

[43] U. Katscher, P. Börnert, C. Leussler, and J. S. van den Brink, "Transmit sense," *Magnetic Resonance in Medicine*, vol. 49, no. 1, pp. 144–150, 2003.

[44] Y. Zhu, "Parallel excitation with an array of transmit coils," *Magnetic Resonance in Medicine*, vol. 51, no. 4, pp. 775–784, 2004.

[45] E. Insko and L. Bolinger, "Mapping of the radiofrequency field," *Journal of Magnetic Resonance, Series A*, vol. 103, no. 1, pp. 82–85, 1993.

[46] V. Yarnykh, "Actual flip-angle imaging in the pulsed steady state: A method for rapid three-dimensional mapping of the transmitted radiofrequency field," *Magnetic resonance in Medicine*, vol. 57, no. 1, pp. 192–200, 2007.

[47] K. Nehrke and P. Börnert, "Dreama novel approach for robust, ultrafast, multislice b1 mapping," *Magnetic Resonance in Medicine*, vol. 68, no. 5, pp. 1517–1526, 2012.

[48] Y. Zhu, L. Alon, C. M. Deniz, R. Brown, and D. K. Sodickson, "System and sar characterization in parallel rf transmission," *Magnetic Resonance in Medicine*, vol. 67, no. 5, pp. 1367–1378, 2012.

[49] J. Warntjes, O. D. Leinhard, J. West, and P. Lundberg, "Rapid magnetic resonance quantification on the brain: Optimization for clinical usage," *Magnetic Resonance in Medicine*, vol. 60, no. 2, pp. 320–329, 2008.

[50] S. Akoka, F. Franconi, F. Seguin, and A. Le Pape, "Radiofrequency map of an nmr coil by imaging," *Magnetic resonance imaging*, vol. 11, no. 3, pp. 437–441, 1993.

[51] N. G. Dowell and P. S. Tofts, "Fast, accurate, and precise mapping of the rf field in vivo using the 180 signal null," *Magnetic Resonance in Medicine*, vol. 58, no. 3, pp. 622–630, 2007.

[52] G. R. Morrell, "A phase-sensitive method of flip angle mapping," *Magnetic Resonance in Medicine*, vol. 60, no. 4, pp. 889–894, 2008.

[53] J. Park and M. Garwood, "B1 mapping using phase information created by frequency-modulated pulses," in *Proceedings of the 16th Annual Meeting of ISMRM*, 2008, p. 361.

[54] F. Bloch and A. Siegert, "Magnetic resonance for nonrotating fields," *Physical Review*, vol. 57, no. 6, p. 522, 1940.

[55] D. C. Noll, J. D. Cohen, C. H. Meyer, and W. Schneider, "Spiral k-space mr imaging of cortical activation," *Journal of Magnetic Resonance Imaging*, vol. 5, no. 1, pp. 49–56, 1995.

[56] K. Scheffler and J. Hennig, "Reduced circular field-of-view imaging," *Magnetic resonance in medicine*, vol. 40, no. 3, pp. 474–480, 1998.

[57] T. Knopp, S. Kunis, and D. Potts, "A note on the iterative mri reconstruction from nonuniform k-space data," *International journal of biomedical imaging*, vol. 2007, 2007.

[58] T.-Q. Li, A. M. Takahashi, T. Hindmarsh, and M. E. Moseley, "Adc mapping by means of a single-shot spiral mri technique with application in acute cerebral ischemia," *Magnetic resonance in medicine*, vol. 41, no. 1, pp. 143–147, 1999.

[59] B. Biswal, F. Zerrin Yetkin, V. M. Haughton, and J. S. Hyde, "Functional connectivity in the motor cortex of resting human brain using echo-planar mri," *Magnetic resonance in medicine*, vol. 34, no. 4, pp. 537–541, 1995.

[60] K. P. Pruessmann, M. Weiger, M. B. Scheidegger, P. Boesiger *et al.*, "Sense: sensitivity encoding for fast mri," *Magnetic resonance in medicine*, vol. 42, no. 5, pp. 952–962, 1999.

[61] M. Lustig, D. Donoho, and J. M. Pauly, "Sparse mri: The application of compressed sensing for rapid mr imaging," *Magnetic resonance in medicine*, vol. 58, no. 6, pp. 1182–1195, 2007.

[62] J. A. Fessler, "Image reconstruction: Algorithms and analysis," to be published.

[63] L. I. Rudin, S. Osher, and E. Fatemi, "Nonlinear total variation based noise removal algorithms," *Physica D: Nonlinear Phenomena*, vol. 60, no. 1, pp. 259–268, 1992.

[64] I. Daubechies, M. Defrise, and C. De Mol, "An iterative thresholding algorithm for linear inverse problems with a sparsity constraint," *Communications on pure and applied mathematics*, vol. 57, no. 11, pp. 1413–1457, 2004.

[65] J. C. Ye, S. Tak, Y. Han, and H. W. Park, "Projection reconstruction mr imaging using focuss," *Magnetic Resonance in Medicine*, vol. 57, no. 4, pp. 764–775, 2007.

[66] S.-J. Kim, K. Koh, M. Lustig, and S. Boyd, "An efficient method for compressed sensing," in *Image Processing, 2007. ICIP 2007. IEEE International Conference on*, vol. 3. IEEE, 2007, pp. III–117.

[67] S. Ramani and J. A. Fessler, "Parallel mr image reconstruction using augmented lagrangian methods," *Medical Imaging, IEEE Transactions on*, vol. 30, no. 3, pp. 694–706, 2011.

[68] F. Zhao, D. Noll, J. Nielsen, and J. Fessler, "Separate magnitude and phase regularization via compressed sensing," *Medical Imaging, IEEE Transactions on*, vol. 31, no. 9, pp. 1713–1723, 2012.

[69] J. D. Poorter, C. D. Wagter, Y. D. Deene, C. Thomsen, F. Ståhlberg, and E. Achten, "Noninvasive mri thermometry with the proton resonance frequency (prf) method: in vivo results in human muscle," *Magnetic resonance in medicine*, vol. 33, no. 1, pp. 74–81, 1995.

[70] J.-F. Nielsen and K. S. Nayak, "Referenceless phase velocity mapping using balanced ssfp," *Magnetic Resonance in Medicine*, vol. 61, no. 5, pp. 1096–1102, 2009.

[71] C. H. Meyer, B. S. Hu, D. G. Nishimura, and A. Macovski, "Fast spiral coronary artery imaging," *Magnetic Resonance in Medicine*, vol. 28, no. 2, pp. 202–213, 1992.

[72] D. Li, C. Paschal, E. Haacke, and L. Adler, "Coronary arteries: three-dimensional mr imaging with fat saturation and magnetization transfer contrast." *Radiology*, vol. 187, no. 2, pp. 401–406, 1993.

[73] S. D. Wolff, S. Chesnick, J. Frank, K. Lim, and R. Balaban, "Magnetization transfer contrast: Mr imaging of the knee." *Radiology*, vol. 179, no. 3, pp. 623–628, 1991.

[74] T. A. Bley, O. Wieben, C. J. François, J. H. Brittain, and S. B. Reeder, "Fat and water magnetic resonance imaging," *Journal of Magnetic Resonance Imaging*, vol. 31, no. 1, pp. 4–18, 2010.

[75] E. Delfaut, J. Beltran, G. Johnson, J. Rousseau, X. Marchandise, and A. Cotten, "Fat suppression in mr imaging: techniques and pitfalls," *Radiographics*, vol. 19, no. 2, pp. 373–382, 1999.

[76] R. Tien, "Fat-suppression mr imaging in neuroradiology: techniques and clinical application." *American Journal of Roentgenology*, vol. 158, no. 2, pp. 369–379, 1992.

[77] W. T. Dixon, "Simple proton spectroscopic imaging." *Radiology*, vol. 153, no. 1, pp. 189–194, 1984.

[78] G. Glover and E. Schneider, "Three-point dixon technique for true water/fat decomposition with B0 inhomogeneity correction," *Magnetic resonance in medicine*, vol. 18, no. 2, pp. 371–383, 1991.

[79] S. Reeder, A. Pineda, Z. Wen, A. Shimakawa, H. Yu, J. Brittain, G. Gold, C. Beaulieu, and N. Pelc, "Iterative decomposition of water and fat with echo asymmetry and least-squares estimation (ideal): Application with fast spin-echo imaging," *Magnetic resonance in medicine*, vol. 54, no. 3, pp. 636–644, 2005.

[80] S. S. Vasanawala, J. M. Pauly, and D. G. Nishimura, "Fluctuating equilibrium mri," *Magnetic resonance in medicine*, vol. 42, no. 5, pp. 876–883, 1999.

[81] B. Quist, B. A. Hargreaves, T. Cukur, G. R. Morrell, G. E. Gold, and N. K. Bangerter, "Simultaneous fat suppression and band reduction with large-angle multiple-acquisition balanced steady-state free precession," *Magnetic Resonance in Medicine*, vol. 67, no. 4, pp. 1004–1012, 2012.

[82] S. S. Vasanawala, J. M. Pauly, and D. G. Nishimura, "Linear combination steady-state free precession mri," *Magnetic resonance in medicine*, vol. 43, no. 1, pp. 82–90, 2000.

[83] Y. Zur, M. Wood, and L. Neuringer, "Spoiling of transverse magnetization in steady-state sequences," *Magnetic resonance in medicine*, vol. 21, no. 2, pp. 251–263, 1991.

[84] K. Scheffler and S. Lehnhardt, "Principles and applications of balanced ssfp techniques," *European radiology*, vol. 13, no. 11, pp. 2409–2418, 2003.

[85] H. Sun, J. A. Fessler, D. C. Noll, and J.-F. Nielsen, "Strategies for improved 3d small-tip fast recovery imaging," *Magnetic Resonance in Medicine*, 2013.

[86] R. C. Mehta, G. B. Pike, and D. R. Enzmann, "Magnetization transfer magnetic resonance imaging: a clinical review," *Topics in Magnetic Resonance Imaging*, vol. 8, no. 4, pp. 214–230, 1996.

[87] D. P. Flame, W. B. Pierce, S. E. Harms, and R. H. Griffey, "Magnetization transfer contrast in fat-suppressed steady-state three-dimensional mr images," *Magnetic resonance in medicine*, vol. 26, no. 1, pp. 122–131, 1992.

[88] R. I. Grossman, J. M. Gomori, K. N. Ramer, F. J. Lexa, and M. D. Schnall, "Magnetization transfer: theory and clinical applications in neuroradiology." *Radiographics*, vol. 14, no. 2, pp. 279–290, 1994.

[89] Ö. Özsarlak, J. W. Van Goethem, M. Maes, and P. M. Parizel, "Mr angiography of the intracranial vessels: technical aspects and clinical applications," *Neuroradiology*, vol. 46, no. 12, pp. 955–972, 2004.

[90] G. E. Santyr, F. Kelcz, and E. Schneider, "Pulsed magnetization transfer contrast for mr imaging with application to breast," *Journal of Magnetic Resonance Imaging*, vol. 6, no. 1, pp. 203–212, 1996.

[91] F. Zhao, J. Fessler, J.-F. Nielsen, and D. Noll, "Separate magnitude and phase regularization via compressed sensing," in *Proceedings of the 19th Scientific Meeting of International Society for Magnetic Resonance in Medicine, Montreal, Canada*, 2011, p. 2841.

[92] F. Zhao, J. A. Fessler, S. M. Wright, J. V. Rispoli, and D. C. Noll, "Optimized linear combinations of channels for complex multiple-coil B1 field estimation with Bloch-Siegert B1 mapping in MRI," in *Biomedical Imaging: From Nano to Macro, 2013 IEEE International Symposium on*. IEEE, 2013, pp. 942–945.

[93] F. Zhao, J. Fessler, J.-F. Nielsen, and D. Noll, "Regularized estimation of magnitude and phase of multiple-coil B1 field via Bloch-Siegert B1 mapping," in *Proceedings of the 20th Scientific Meeting of International Society for Magnetic Resonance in Medicine, Melbourne*, 2012, p. 2512.

[94] F. Zhao, J.-F. Nielsen, and D. Noll, "Four-dimensional spectral-spatial pulse for fat saturation with parallel excitation: Preliminary results on 3T scanners," in *Proceedings of the 20th Scientific Meeting of International Society for Magnetic Resonance in Medicine, Melbourne*, 2012, p. 636.

[95] F. Zhao, S. Swanson, J.-F. Nielsen, J. Fessler, and D. Noll, "Simultaneous fat saturation and magnetization transfer preparation with 2D small-tip fast recovery imaging," in *Proceedings of the 21th Scientific Meeting of International Society for Magnetic Resonance in Medicine, Salt Lake City*, 2013, p. 2507.

[96] F. Zhao, J.-F. Nielsen, and D. Noll, "Fat saturation for 2D small-tip fast recovery imaging using tailored 3D spectral-spatial pulses," in *Proceedings of the 21th Scientific Meeting of International Society for Magnetic Resonance in Medicine, Salt Lake City*, 2013, p. 252.

[97] F. Zhao, H. Sun, J.-F. Nielsen, J. Fessler, and D. Noll, "Balanced ssfp-like imaging with simultaneous water-fat separation and band reduction using small-tip fast recovery," in *Proceedings of the 21st Scientific Meeting of International Society for Magnetic Resonance in Medicine*, 2013, p. 2403.

[98] A. Funai, J. Fessler, D. Yeo, V. Olafsson, and D. Noll, "Regularized field map estimation in MRI," *Medical Imaging, IEEE Transactions on*, vol. 27, no. 10, pp. 1484–1494, 2008.

[99] J. A. Fessler and D. C. Noll, "Iterative image reconstruction in mri with separate magnitude and phase regularization," in *Biomedical Imaging: Nano to Macro, 2004. IEEE International Symposium on.* IEEE, 2004, pp. 209–212.

[100] M. Bydder and M. D. Robson, "Partial fourier partially parallel imaging," *Magnetic resonance in medicine*, vol. 53, no. 6, pp. 1393–1401, 2005.

[101] D. C. Noll, D. G. Nishimura, and A. Macovski, "Homodyne detection in magnetic resonance imaging," *Medical Imaging, IEEE Transactions on*, vol. 10, no. 2, pp. 154–163, 1991.

[102] M. V. W. Zibetti and A. R. De Pierro, "Separate magnitude and phase regularization in mri with incomplete data: Preliminary results," in *Biomedical Imaging: From Nano to Macro, 2010 IEEE International Symposium on.* IEEE, 2010, pp. 736–739.

[103] A. R. De Pierro, "A modified expectation maximization algorithm for penalized likelihood estimation in emission tomography," *Medical Imaging, IEEE Transactions on*, vol. 14, no. 1, pp. 132–137, 1995.

[104] V. Rieke, K. K. Vigen, G. Sommer, B. L. Daniel, J. M. Pauly, and K. Butts, "Referenceless prf shift thermometry," *Magnetic resonance in medicine*, vol. 51, no. 6, pp. 1223–1231, 2004.

[105] W. Grissom, K. B. Pauly, M. Lustig, V. Rieke, J. Pauly, and N. McDannold, "Regularized referenceless temperature estimation in prf-shift mr thermometry," in *Biomedical Imaging: From Nano to Macro, 2009. ISBI'09. IEEE International Symposium on.* IEEE, 2009, pp. 1235–1238.

[106] L. Sacolick, G. W. A., G. Kudielka, W. Loew, and M. W. Vogel, "Interference Bloch-Siegert B1 mapping for parallel transmit," in *Proceedings of the 19th Scientific Meeting of International Society for Magnetic Resonance in Medicine, Montreal, Canada*, 2011, p. 2926.

[107] K. Nehrke and P. Bornert, "Improved B1-mapping for multi rf transmit systems," in *Proceedings of the 16th Scientific Meeting of International Society for Magnetic Resonance in Medicine, Toronto, Canada*, 2008, p. 353.

[108] D. Brunner and K. Pruessmann, "B 1+ interferometry for the calibration of rf transmitter arrays," *Magnetic Resonance in Medicine*, vol. 61, no. 6, pp. 1480–1488, 2009.

[109] S. Malik, D. Larkman, and J. Hajnal, "Optimal linear combinations of array elements for B1 mapping," *Magnetic Resonance in Medicine*, vol. 62, no. 4, pp. 902–909, 2009.

[110] S. Kirkpatrick, C. Gelatt, and M. Vecchi, "Optimization by simulated annealing," *science*, vol. 220, no. 4598, p. 671, 1983.

[111] N. Hollingsworth, K. Moody, J. Nielsen, D. Noll, M. McDougall, and S. Wright, "Tuning ultra-low output impedance amplifiers for optimal power and decoupling in parallel transmit MRI," in *Biomedical Imaging: From Nano to Macro, 2013 IEEE International Symposium on.* IEEE, 2013.

[112] K. L. Moody, N. A. Hollingsworth, J.-F. Nielsen, D. Noll, M. P. McDougall, and S. M. Wright, "Eight-channel transmit/receive head array for use with ultra-low output impedance amplifiers," in *Biomedical Imaging: From Nano to Macro, 2013 IEEE International Symposium on.* IEEE, 2013.

[113] D. Brunner and K. Pruessmann, "A matrix approach for mapping array transmit fields in under a minute," *Quadrature*, vol. 60, no. 80, p. 100, 2008.

[114] J. Hua, C. Jones, J. Blakeley, S. Smith, P. van Zijl, and J. Zhou, "Quantitative description of the asymmetry in magnetization transfer effects around the water resonance in the human brain," *Magnetic Resonance in Medicine*, vol. 58, no. 4, pp. 786–793, 2007.

[115] J. Fessler and S. Booth, "Conjugate-gradient preconditioning methods for shift-variant PET image reconstruction," *Image Processing, IEEE Transactions on*, vol. 8, no. 5, pp. 688–699, 1999.

[116] K. Lange, *Numerical analysis for statisticians.* Springer, 2010.

[117] [Online]. Available: http://www.bic.mni.mcgill.ca/brainweb/

[118] C. Cocosco, V. Kollokian, K. Kwan, G. Pike *et al.*, "Brainweb: Online interface to a 3D MRI simulated brain database," 1997.

[119] R. Kwan, A. Evans, and G. Pike, "MRI simulation-based evaluation of image-processing and classification methods," *Medical Imaging, IEEE Transactions on*, vol. 18, no. 11, pp. 1085–1097, 1999.

[120] R. Kwan, A. Evans, and Pike, "An extensible MRI simulator for post-processing evaluation," in *Visualization in Biomedical Computing.* Springer, 1996, pp. 135–140.

[121] D. Collins, A. Zijdenbos, V. Kollokian, J. Sled, N. Kabani, C. Holmes, and A. Evans, "Design and construction of a realistic digital brain phantom," *Medical Imaging, IEEE Transactions on*, vol. 17, no. 3, pp. 463–468, 1998.

[122] A. O. Hero III, J. A. Fessler, and M. Usman, "Exploring estimator bias-variance tradeoffs using the uniform CR bound," *Signal Processing, IEEE Transactions on*, vol. 44, no. 8, pp. 2026–2041, 1996.

[123] L. Alon, C. M. Deniz, R. Brown, D. K. Sodickson, and Y. Zhu, "Method for in situ characterization of radiofrequency heating in parallel transmit MRI," *Magnetic Resonance in Medicine*, 2012.

[124] J. A. Heilman, J. D. Derakhshan, M. J. Riffe, N. Gudino, J. Tkach, C. A. Flask, J. L. Duerk, and M. A. Griswold, "Parallel excitation for b-field insensitive fat-saturation preparation," *Magnetic Resonance in Medicine*, vol. 68, no. 2, pp. 631–638, 2012.

[125] K. Setsompop, V. Alagappan, B. Gagoski, A. Potthast, F. Hebrank, U. Fontius, F. Schmitt, L. Wald, and E. Adalsteinsson, "Broadband slab selection with b 1+ mitigation at 7t via parallel spectral-spatial excitation," *Magnetic Resonance in Medicine*, vol. 61, no. 2, pp. 493–500, 2009.

[126] S. Malik, D. Larkman, D. O'Regan, and J. Hajnal, "Subject-specific water-selective imaging using parallel transmission," *Magnetic Resonance in Medicine*, vol. 63, no. 4, pp. 988–997, 2010.

[127] P. Kassakian, "Convex approximation and optimization with applications in magnitude filter design and radiation pattern synthesis," *University of California, Berkeley*, 2006.

[128] S. J. Malik, S. Keihaninejad, A. Hammers, and J. V. Hajnal, "Tailored excitation in 3D with spiral nonselective (spins) rf pulses," *Magnetic Resonance in Medicine*, vol. 67, no. 5, pp. 1303–1315, 2012.

[129] W. A. Grissom, M.-M. Khalighi, L. I. Sacolick, B. K. Rutt, and M. W. Vogel, "Small-tip-angle spokes pulse design using interleaved greedy and local optimization methods," *Magnetic Resonance in Medicine*, vol. 68, no. 5, pp. 1553–1562, 2012.

[130] C. Collins, W. Liu, B. Swift, and M. Smith, "Combination of optimized transmit arrays and some receive array reconstruction methods can yield homogeneous images at very high frequencies," *Magnetic Resonance in Medicine*, vol. 54, no. 6, pp. 1327–1332, 2005.

[131] F. Bardati, A. Borrani, A. Gerardino, and G. Lovisolo, "Sar optimization in a phased array radiofrequency hyperthermia system," *Biomedical Engineering, IEEE Transactions on*, vol. 42, no. 12, pp. 1201–1207, 1995.

[132] M. Cloos, N. Boulant, M. Luong, G. Ferrand, E. Giacomini, D. Le Bihan, and A. Amadon, "kt-points: Short three-dimensional tailored rf pulses for flip-angle homogenization over an extended volume," *Magnetic Resonance in Medicine*, vol. 67, no. 1, pp. 72–80, 2012.

[133] M. Allison and J. Fessler, "Accelerated computation of regularized field map estimates," in *Proceedings of the 20th Scientific Meeting of International Society for Magnetic Resonance in Medicine*, 2012, p. 413.

[134] P. M. Jakob, T. Wang, G. Schultz, H. Hebestreit, A. Hebestreit, M. Elfeber, D. Hahn, and A. Haase, "Magnetization transfer short inversion time inversion recovery enhanced1h MRI of the human lung," *Magnetic Resonance Materials in Physics, Biology and Medicine*, vol. 15, no. 1-3, pp. 10–17, 2002.

[135] G. E. Gold, S. B. Reeder, H. Yu, P. Kornaat, A. S. Shimakawa, J. W. Johnson, N. J. Pelc, C. F. Beaulieu, and J. H. Brittain, "Articular cartilage of the knee: Rapid three-dimensional mr imaging at 3.0 t with ideal balanced steady-state free precessioninitial experience1," *Radiology*, vol. 240, no. 2, pp. 546–551, 2006.

[136] D. G. Disler, T. R. McCauley, C. R. Wirth, and M. D. Fuchs, "Detection of knee hyaline cartilage defects using fat-suppressed three-dimensional spoiled gradient-echo mr imaging: comparison with standard mr imaging and correlation with arthroscopy." *AJR. American journal of roentgenology*, vol. 165, no. 2, pp. 377–382, 1995.

[137] P. Lang, F. Noorbakhsh, and H. Yoshioka, "Mr imaging of articular cartilage: current state and recent developments," *Radiologic Clinics of North America*, vol. 43, no. 4, pp. 629–639, 2005.

[138] C. K. Kuhl, H. Kooijman, J. Gieseke, and H. H. Schild, "Effect of b1 inhomogeneity on breast mr imaging at 3.0 t," *Radiology*, vol. 244, no. 3, pp. 929–930, 2007.

[139] S. C. Deoni, B. K. Rutt, and T. M. Peters, "Rapid combined t1 and t2 mapping using gradient recalled acquisition in the steady state," *Magnetic Resonance in Medicine*, vol. 49, no. 3, pp. 515–526, 2003.

[140] O. Bieri, M. Klarhofer, and K. Scheffler, "Chimera steady state free precession (chimera ssfp)," in *Proceedings of the 17th Scientific Meeting of International Society for Magnetic Resonance in Medicine*, 2009, p. 2767.

[141] D. P. Bertsekas, "Multiplier methods: a survey," *Automatica*, vol. 12, no. 2, pp. 133–145, 1976.

[142] D. S. WELLER, S. RAMANI, J.-F. NIELSEN, and J. A. FESSLER, "Monte carlo sure-based parameter selection for parallel magnetic resonance imaging reconstruction," *Magnetic Resonance in Medicine*, 2013.

[143] S. Yu, A. Shaharyar Khwaja, and J. Ma, "Compressed sensing of complex-valued data," *Signal Processing*, vol. 92, no. 2, pp. 357–362, 2012.

[144] P. van Zijl and N. N. Yadav, "Chemical exchange saturation transfer (cest): what is in a name and what isn't?" *Magnetic Resonance in Medicine*, vol. 65, no. 4, pp. 927–948, 2011.

[145] J. Fessler *et al.* Image reconstruction toolbox. [Online]. Available: http://web.eecs.umich.edu/~fessler/code/index.html